Exploring hydroperoxides in combustion: History, recent advances and perspectives

Zhandong R Wang, Olivier Herbinet, Nils Hansen, Frédérique Battin-Leclerc

EXPLORING HYDROPEROXIDES IN COMBUSTION: HISTORY, AND RECENT ADVANCES AND PERSPECTIVES

Zhandong Wang[1,2,3], Olivier Herbinet[4], Nils Hansen[5], Frédérique Battin-Leclerc[4*]

[1] National Synchrotron Radiation Laboratory, University of Science and Technology of China, Hefei, Anhui 230029, PR China;

[2] State Key Laboratory of Fire Science, University of Science and Technology of China, Hefei, Anhui 230026, PR China;

[3] King Abdullah University of Science and Technology (KAUST), Clean Combustion Research Center (CCRC), Thuwal 23955-6900, Saudi Arabia;

[4] Laboratoire de Réactions et Génie des Procédés, CNRS – Université de Lorraine, ENSIC, 1 rue Grandville 54001 Nancy, France;

[5] Combustion Research Facility, Sandia National Laboratories, Livermore, California 94551, United States

Published in Progress in Energy and Combustion Science, 73 (2019) 132-181

ABSTRACT

The aim of this paper is to review recent progress in detection and quantification of hydroperoxides, and to understand their reaction kinetics in combustion environments. Hydroperoxides, characterized by an -OOH group, are ubiquitous in the atmospheric oxidation of volatile organic compounds (~300 K), and in the liquid and gas phase oxidation of fuel components at elevated temperatures (~400-1000 K). They are responsible for two-stage fuel ignition in internal combustion engines and they play an important role in the formation and evolution of secondary organic aerosols in the atmosphere. The introduction outlines the importance of hydroperoxide chemistry in combustion reaction processes. In addition to this main topic, the role of hydroperoxide in atmospheric and liquid phase oxidation chemistry is also introduced, for a more general perspective. The second part of this paper briefly reviews the mechanistic insights of hydroperoxide chemistry in combustion systems, including experimental detection of these reactive species before 2010. Since that time significant progress has been made by advanced diagnostic techniques like tunable synchrotron vacuum ultraviolet photoionization mass spectrometry and infrared cavity ring-down spectroscopy. The third chapter of this work summarizes progress in gas phase oxidation experiments to measure hydrogen peroxide, alkyl hydroperoxides, olefinic hydroperoxides, ketohydroperoxides, and more complex hydroperoxides that include as many as five oxygen atoms. The fourth section details recent advances in understanding the combustion chemistry of hydroperoxides, involving the formation of carboxylic acids and diones, as well as the development of oxidation models that include a third O_2 addition reaction mechanism. Finally, challenges are discussed, and perspectives are offered regarding the future of accurately measuring molecule-specific hydroperoxide concentrations and understanding their respective reaction kinetics.

Keywords: Hydroperoxides, gas phase oxidation, autoignition, diagnostics, kinetics.

LIST OF ABBREVIATIONS

APCI atmospheric pressure chemical ionization
AOM acousto-optic modulator
BDE bond dissociation energy
CI Criegee intermediate
CFR cooperative fuel research
CRDS cavity ring-down spectroscopy
Cw-CRDS continuous-wave CRDS
CA crank angle
CSP computational singular perturbation
CCN cloud condensation nuclei
Cp specific heat capacities
DME dimethyl ether
DMM dimethoxymethane
DEE diethyl ether
DKHP diketohydroperoxide
DHPCE dihydroperoxy cyclic ether
$\Delta_f H_0(298K)$ standard enthalpy of formation
$S_0(298K)$ standard molar entropy
EI-MS electron ionization mass spectrometry
EI electron ionization
ELVOC extremely low-volatility organic compound
FT flow tube
FTIR Fourier-transform infrared
FID flame ionization detector
FAGE fluorescence assay by gas expansion
φ equivalence ratio
GC gas chromatography
HOM highly oxygenated molecule
HCCI homogeneous charge compression ignition
HOȮ hydroperoxy radical
HPMF hydroperoxymethyl formate
HPLC high pressure liquid chromatography
HRR heat release rate
HPCE hydroperoxy cyclic ether
IR infrared
IDT ignition delay time
JSR jet-stirred reactor
KHP ketohydroperoxide
KDHP ketodihydroperoxide
KHPCE ketohydroperoxy cyclic ether
LVOC low volatility organic compound
MDF mass discrimination factor
MF mole fraction

NTC negative temperature coefficient
ȮH hydroxyl radical
ȮOQOOH hydroperoxyalkyl peroxy radical
OTMS orbitrap mass spectrometry
$\dot{O}OP(OOH)_2$ dihydroperoxyalkyl peroxy radical
OHP olefinic hydroperoxide
PI photon ionization
PIE photoionization efficiency
PEPICO photoelectron photoion coincidence
$\dot{P}(OOH)_2$ dihydroperoxy alkyl radical
ȮOOH hydroperoxyalkyl radical
ROOH alkyl hydroperoxide
RH fuel
Ṙ alkyl radical
RȮ alkylperoxy radical
RCM rapid compression machine
SOA secondary organic aerosol
SPI-MS single-photoionization mass spectrometry
SVUV-PIMS synchrotron vacuum-ultraviolet photoionization mass spectrometry
S/N signal-to-noise
SIVOC semi-volatility and intermediate-volatility organic compound
T temperature
$\dot{T}(OOH)_3$ trihydroperoxyalkyl radical
τ residence time
UV ultraviolet
VOC volatile organic compound
VHP vinylhydroperoxide
VUV vacuum-ultraviolet
1,2-DME 1,2-dimethoxyethane

Content list

1. INTRODUCTION

Hydroperoxides are molecules containing an -OOH group. The O-O single bond in hydroperoxides is substantially weaker than other single bonds of organic compounds. C-C bond dissociation energies (BDE) in organic compounds are most often between 250 and 440 kJ/mol and the BDEs for C-H bonds are between 350 and 590 kJ/mol. For C-O and O-H bonds, BDEs are in the range of 330-480 kJ/mol and 350-480 kJ/mol, respectively [1]. In comparison, the BDE of the O-OH bond in hydrogen peroxide (H_2O_2, the most stable hydroperoxide), is 211 kJ/mol [1]. These small BDEs of hydroperoxides enable bond dissociation and the formation of two radical species, leading to enhanced reactivity. As shown in Fig. 1, this easy bond dissociation has made hydroperoxides --especially ketohydroperoxides-- the center of chemistry governing low-temperature oxidation and triggering autoignition in internal combustion engines (Section 1.2).

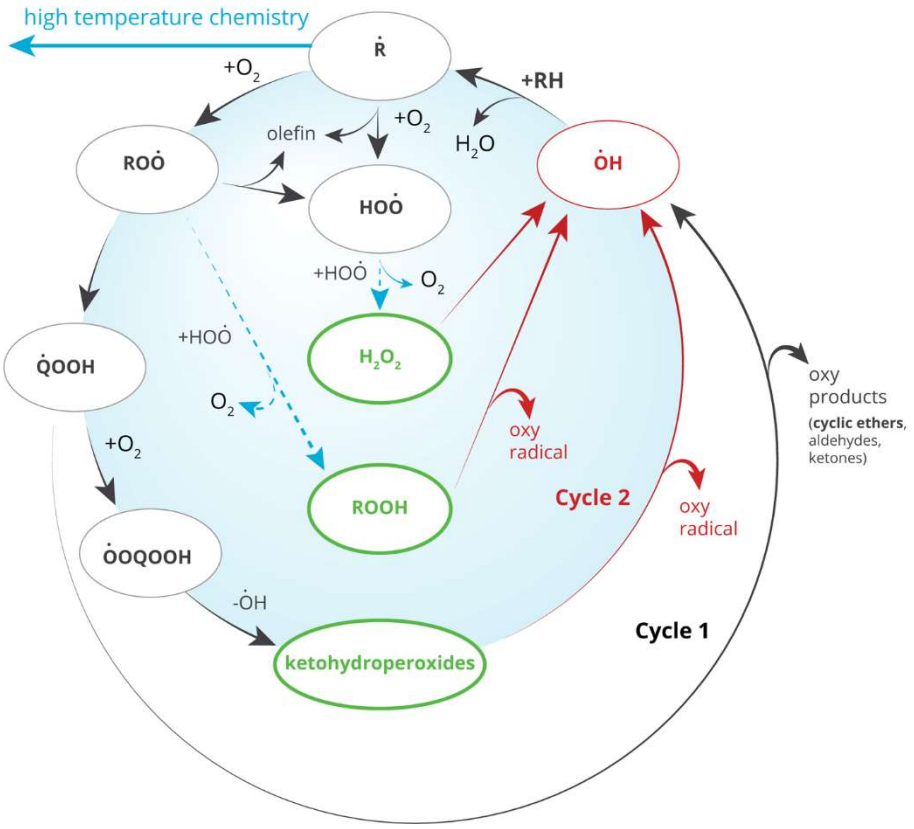

Figure 1: Schematic of main reactions in currently accepted models of alkane low-temperature oxidation.

The stability and oxidative properties of hydrogen peroxide make it a valuable product with a wide range of applications such as tooth whitening, bleaching, or disinfectants [2]. Hydrogen peroxide has also been proposed as a green monopropellant for rocket engines [3]. This versatility is not applicable to organic peroxides (i.e., carbon-containing hydroperoxides), and --with the exception of tert-butyl hydroperoxide-- few can be purchased. Hydrogen peroxide [4] and tert-butyl hydroperoxide [5] are commonly used as precursors for hydroxyl radicals in chemical kinetics studies using laser flash photolysis and shock tube experiments, respectively.

Several methods have been proposed to synthesize small organic hydroperoxides [6-11]; these are largely based on reactions of hydrogen peroxide with suitable precursors. For example, dimethyl sulfate/diethyl sulfate can be used to produce methyl hydroperoxide (CH_3OOH)/ethyl hydroperoxide (C_2H_5OOH); formaldehyde can yield hydroxymethyl hydroperoxide ($HOCH_2OOH$); acetaldehyde can be transformed to 1-hydroxyethyl hydroperoxide, and alkyl methanesulfonate can form alkyl hydroperoxides (*n*-propyl through *n*-decyl).

Detection, identification, quantification, and thorough investigation of the kinetics of organic hydroperoxides are very challenging, mainly due to the lack of commercial availability of these reactive intermediates, the difficulties in their synthesis and purification due to their potential to spontaneous and exothermic decomposition [11, 12], and the limitations of analytical tools (e.g., gas chromatography, GC). For these reasons, reports on the kinetics of hydroperoxides in the literature study are scarce.

Nevertheless, as shown here, abundant evidence can be found in the literature for the formation of organic peroxides during oxidation processes. Organic peroxides are mainly alkyl hydroperoxides that contain an -OOH function linked to an alkyl chain, alkyldihydroperoxides with two –OOH functions connected to an alkyl chain, ketohydroperoxides (KHPs) that include an -OOH function linked to an aldehyde or a ketone, and olefinic hydroperoxides, i.e. molecules including an –OOH function linked to an alkenyl chain.

This review primarily addresses hydroperoxides important in combustion chemistry; however, for a more general background of the role of hydroperoxides in oxidation reactions, the introduction provides information about the significance of hydroperoxides in two other contexts: atmospheric chemistry (Section 1.1) and liquid phase oxidation (Section 1.2). The term low-temperature oxidation is used in the field of combustion, while in atmospheric and liquid phase chemistry, auto-oxidation is normally adopted; both terms relate to the chemistry of the peroxy radicals and the formation of peroxide species [13]. Heavy-weight organic hydroperoxides are also important in biological systems as they can be formed from the reactions of radicals and singlet O-atoms with lipids, peptides, proteins or amino-acids and they have adverse effects on human health [14-16]. Hydroperoxides in biological systems will not be detailed in this review.

1.1 Hydroperoxides in atmospheric chemistry

Peroxides, including hydrogen peroxide (H_2O_2) and organic hydroperoxides, are important oxidants in the atmosphere with a mixing ratio (i.e., mole fraction) of 0.1-1 ppb [8, 17-20]. They participate in HO_x, NO_x, and O_3 chemistry [21, 22]; they contribute to acid precipitations and acid mists [23], and they are important components in secondary organic aerosols (SOAs) [24-28]. The formation and depletion kinetics of peroxides have been the targets of research for many years [29]. It is understood that the ambient environment (concentration level of NO_x, level of solar radiation, temperature, pressure, and humidity), affects the generation of hydroperoxides [30-32].

Some studies have shown that the production of H_2O_2 is positively correlated to temperature and solar radiation [33-38], while high concentrations of NO_x inhibit the formation of peroxides. In the

gas phase, the oxidation of volatile organic compounds (VOC) leads to H_2O_2 and other organic hydroperoxides. Table 1 lists some peroxide and peroxy acid intermediates commonly observed in the atmosphere [23]. The peroxide with the highest concentration in the atmosphere is H_2O_2, while methyl hydroperoxide and hydroxymethyl hydroperoxide are among the most important organic peroxides [23]. One major route for H_2O_2 production is the self-reaction of hydroperoxy radicals ($HO\dot{O} + HO\dot{O} \rightleftarrows H_2O_2 + O_2$) [39]. The reaction of methylperoxy radical and ethylperoxy radical with hydroperoxy radical ($RO\dot{O} + HO\dot{O} \rightleftarrows ROOH + O_2$) could produce methyl hydroperoxide and ethyl hydroperoxide [40].

Table 1: Hydroperoxide commonly observed in atmospheric oxidation of volatile organic compounds [23].

Name	Abbreviation	Structure
hydrogen peroxide	H_2O_2	HOOH
methyl hydroperoxide	MHP	CH_3OOH
hydroxymethyl hydroperoxide	HMHP	$CH_2(OH)OOH$
ethyl hydroperoxide	EHP	CH_3CH_2OOH
1-hydroxyethyl hydroperoxide	1-HEHP	$CH_3CH(OH)OOH$
2-hydroxyethyl hydroperoxide	2-HEHP	$HOCH_2CH_2OOH$
1-hydroxypropyl hydroperoxide	1-HPHP	$CH_3CH_2CH(OH)OOH$
2-hydroxypropyl hydroperoxide	2-HPHP	$CH_3CH(OH)CH_2OOH$
dihydroperoxy methane	DHPM	$HOOCH_2OOH$
peroxyformic acid	PFA	$CH(O)OOH$
peroxyacetic acid	PAA	$CH_3C(O)OOH$

In addition to these pathways, some studies suggest that the ozonolysis of alkenes may directly lead to hydrogen and hydroxymethyl peroxide and methyl hydroperoxide [41-47], without the participation of hydroperoxy and alkylperoxy radicals. As shown in Fig. 2(a), the O_3 addition to ethylene leads to a primary ozonide, which subsequently dissociates into a diradical intermediate. The dissociation of this diradical leads either to a carbonyl oxide (i.e., the Criegee intermediate (CI)), or the isomerization of the diradical produces a KHP, recently detected in ozonolysis experiments [48].

The formation of the peroxides is promoted in humid environments by the reaction of the CI with water vapor [47, 49] in Fig. 2(a). In this process, hydroxymethyl hydroperoxide can be produced [23, 50]. Similarly, the bimolecular reaction of the CI with formic acid could lead to hydroperoxymethyl formate (HPMF, $HOOCH_2OCHO$) [51-56]. The experimental measurements reveal a very fast rate for the reaction of the CI with carboxylic acids [57, 58]

For larger alkenes (Fig. 2(b)), the formed CIs could undergo a 1,4-hydrogen shift to form an α-hydroperoxide alkene (i.e., a vinylhydroperoxide (VHP) intermediate [59]). Some small VHPs were measured via carboxylic acid-catalyzed tautomerization of CIs [60]. The decomposition of VHP releases an ȮH radical and leads to a vinoxy radical; the latter undergoes further intramolecular isomerization and multiple O_2 addition steps, causing highly oxygenated molecules (HOM) in the ozonolysis of biogenic emissions, such as mono-terpenes and their model compounds [25, 61-63].

HOM intermediates have extremely low volatility; they normally contain multiple functional groups such as carbonyl, hydroxyl, and hydroperoxy, and are an important source for SOA [25]. Although the estimated mass contribution of the compounds containing hydroperoxy groups in α-pinene SOA varies greatly in different studies [26], the peroxides have been shown to be the major constituents of SOA [27, 64-69]. The decomposition of the hydroperoxy group recycles the ȮH radicals via photo-oxidation and/or bimolecular reactions with other radicals, and enhances the auto-oxidation process [70, 71]; it also affects the atmospheric SOA formation and evolution processes.

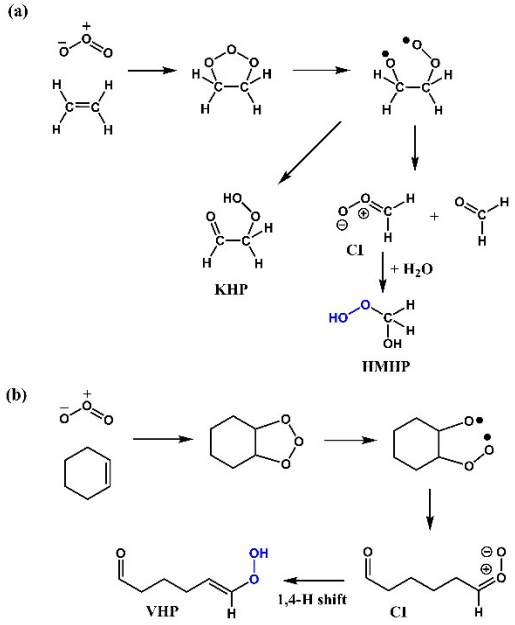

Figure 2: Examples of formation of hydroperoxide via ozonolysis of (a) ethylene and (b) cyclohexene. Only the radical pathway from the initial adduct is presented.

1.2 Hydroperoxides in the chemistry of fuel oxidation and combustion

This section introduces hydroperoxide chemistry in gas phase oxidation. Historically, studies of liquid and gas phase oxidation (especially those directed toward understanding the chemistry of hydroperoxides), were performed in parallel. Observations in the liquid phase oxidation of hydrocarbons helped to reveal their chemistry in the gas phase; this section begins with a summary of liquid phase oxidation from the important literature.

Alkyl hydroperoxides are known to be the primary products and promoters of liquid phase oxidation of organic reactants [72-76]. When radical intermediates are generated, they react directly with the initial organic reactant by H-abstraction. The addition of oxygen to the radical site that follows forms a peroxy radical, which subsequently reacts by H-abstraction of another organic molecule to produce a hydroperoxide. The decomposition of this hydroperoxide via the weak O-O bond forms two new radicals and promotes the reaction propagation [77]. The hydroperoxides formed in the jet fuels could then attack elastomers that result in leaks, or inoperation in aircraft fuel systems [78].

Fuel liquid phase oxidation can also yield a wide range of products, in addition to hydroperoxides--isomeric alkenes, alcohols, ketones, aldehydes, esters, carboxylic acids, cyclic ethers or lactones [72, 75, 79]. The formation of these products affects the stability of fuels, lubricants and/or additives under storage or operating conditions, and can ultimately lead to the formation of gums and deposits that degrade engine operating conditions by blocking mechanical devices [80]. Furthermore, the oxidation stability of methyl esters is of the highest concern since it is one of the major technical issues associated with the use of biodiesel [81].

The chemistry of hydrocarbon liquid phase oxidation was determined by measuring several key intermediates: In 1979, a team that included Stephan Korcek at Ford Motor Company, reported yields of isomeric monohydroperoxides as high as 10% during *n*-hexadecane oxidation in a stirred flow reactor at 453 K [73]. The hydroperoxides were quantified by GC after a complex procedure of reduction, purification, and separation [73]. Isomeric hydroperoxides were reduced in isomeric alcohols by sodium borohydride. After reduction, the authors observed that the diols indicated the presence of dihydroperoxides or KHPs [73]. In another study of pentaerythrityl tetraheptanoate auto-oxidation [82], Korcek's team mentioned that the auto-oxidation mechanism of hydrocarbons occurs through the formation of KHPs; today this mechanism is considered in kinetic modeling. These authors specifically examined the importance of γ-KHPs when the carbonyl and hydroperoxy functions were separated by a $-CH_2-$ group; such KHPs can be the precursors for carboxylic acids and methyl ketones, experimentally discovered to be significant products [73, 82]. In 1994, using a similar procedure, the same team [83] again studied the *n*-hexadecane oxidation reaction network from 393 to 463 K; the presence of hydroperoxyhexadecanones (KHPs, $O=C_{16}H_{31}OOH$) or dihydroperoxyhexadecanes [$C_{16}H_{32}(OOH)_2$] was revealed through the formation of hexadecanediols during the reduction by triphenylphosphine.

Hydroperoxides are also important during gas phase fuel chemistry in internal combustion engines because they trigger the first stage (cool flame) and the second stage autoignition of gasoline and diesel fuel components [84-86]. This relationship can be seen in Fig. 3, which shows the history of simulated species during constant pressure *n*-heptane autoignition. First stage autoignition, indicated by the first small temperature (T) rise, occurs when KHPs begin to be consumed. The second stage autoignition--corresponding to the second large temperature rise--appears together with sharp H_2O_2 consumption. Controlling these thermal phenomena is key to mastering engine knock in spark-ignited engines [87] and improving the design of diesel [86] and homogeneous charge compression ignition (HCCI) [85] engines.

Gas phase chemistry of fuel component oxidation at low temperatures (below 900 K) has been studied for many years because it is the origin of autoignition and the cool flame phenomena [89]. Readers are referred to Griffiths and Scott [90], Walker and Morley [91], and more recent papers by Battin-Leclerc [92], Zádor et al. [93] and Westbrook et al. [94]. Hydroperoxides are at the center of this chemistry. The main steps, currently accepted to explain this chemistry for alkane oxidation, appear in Fig. 1.

The chemistry is initiated by slow reactions of the fuel molecule with oxygen. Except in this very early stage, the chemistry is well described as propagation cycles initiated by an H-abstraction of

a hydroxyl radical (ȮH) from the fuel molecule, RH in Fig. 1. An alkyl radical (Ṙ) is formed during this process and the oxygen addition to Ṙ leads to the ROȮ radical. Further isomerization of the ROȮ radical involves the internal transfer of an H-atom to produce a hydroperoxyalkyl (ṪOOH) radical. This first cycle (cycle 1) is closed via the formation of an oxygenated product (a cyclic ether, an aldehyde or a ketone) and the regeneration of an ȮH radical from the ṪOOH radical.

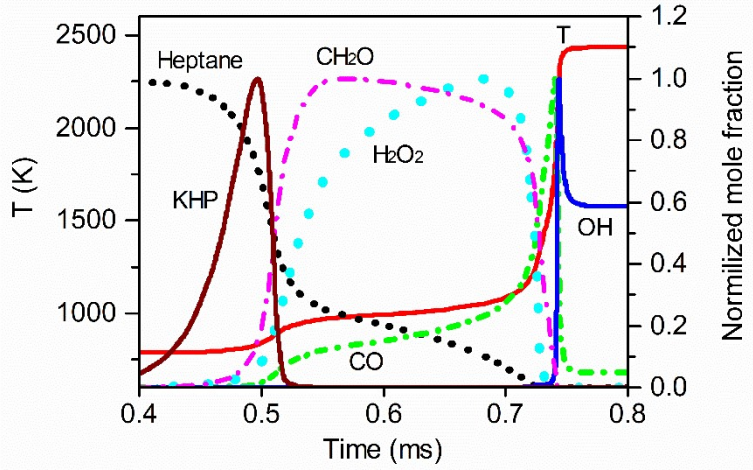

Figure 3: Simulated *n*-heptane autoignition in a closed homogenous batch reactor using model in Ref. [88]. Equivalence ratio is 1.0, pressure is 5.07 MPa. Mixture composition is 1.15% *n*-heptane/ 12.7% O_2 / 86.15% N_2. Mole fraction of each species is normalized by its maximum value. Maximum mole fraction is *n*-heptane 1.15×10^{-2}, CH_2O 5.9×10^{-3}, H_2O_2 3.8×10^{-3}, CO 5.4×10^{-2}, ȮH 2.1×10^{-3}, and KHP 4.6×10^{-4} – plotted following an idea from Ref. [86].

The most abundant oxygenated products resulting from cycle 1 are cyclic ethers [95], which are routinely identified and quantified by GC [96]. Cyclic ethers could be derivatives of oxiranes, oxetanes, tetrahydrofurans, and tetrahydropyrans that include an oxygenated heterocycle with three, four, five and six atoms, respectively.

A reaction competing with the oxygen addition to the Ṙ radical is a concerted reaction of Ṙ with O2; the conjugated alkene and an HOȮ radical are formed. In the ROȮ radical, the reaction competing with its internal isomerization is the concerted HOȮ elimination, also leading to the conjugated alkene. HOȮ can yield hydrogen peroxide (H_2O_2) by H-abstraction from the initial reactant RH, or by disproportionation with another HOȮ radical. H_2O_2 dissociation is typically viewed as a chain branching reaction that regenerates two reactive ȮH radicals from two less reactive HOȮ radicals.

Other concurrent channels occurring from the ROȮ radical are disproportionation with HOȮ radical and H-abstractions from the RH (not shown in Fig. 1), yielding alkyl hydroperoxide (ROOH) isomers. Similarly, abstractions of an H-atom from the reactant by ROȮ radicals are the main reactions that produce hydroperoxides during the liquid phase oxidation [75]. ROOH dissociation is another branching reaction that regenerates ȮH radicals, along with the formation of a reactive alkoxy radical. When the temperature is sufficiently high (> ~ 700 K) to overcome the barrier for O-OH bond dissociation, these branching reactions from H_2O_2 and ROOH consume the stable molecules produced at lower temperatures, and increase the global reactivity. However,

the most efficient branching reaction (the origin of high reactivity of alkane at temperatures as low as 550 K), is a reaction that participates in a second propagating cycle (cycle 2). This branching reaction occurs after a second oxygen addition to ȮOOH radical, producing a hydroperoxyalkyl peroxy (ȮOQOOH) radical. The internal isomerization of this radical by abstracting the C-H adjacent to the –OOH group, followed by a rapid OH-elimination, yields a KHP molecule and an ȮH radical. As discussed at the beginning of this section, this reaction pathway is similar to the channel toward KHPs in liquid phase oxidation [82, 83]. The further decomposition of KHPs results in another ȮH radical and a ketoalkoxyl radical.

With increased temperature, cycle 2 becomes less important and ȮH radicals are reduced. In contrast, cycle 1 and the formation of HOȮ radicals begins to prevail. First, oxygen addition reactions are reversed and inhibited at higher temperatures. Second, at higher temperatures the activation energy barriers for ȮOOH radical dissociation to cyclic ethers and other β-scission products (cycle 1), and the concerted elimination of ROȮ radical to HOȮ radical, are overcome. This is the origin of a specific behavior of alkane oxidation observed since 1929 [97]: the counter intuitive *negative temperature coefficient* (NTC).

All recent models of alkane low-temperature oxidation are based on the kinetic scheme shown in Fig. 1. This reaction scheme has been used since the 90's, particularly by teams at Lawrence Livermore National Laboratory [98], Milano [99], Nancy [100], Galway [88] and KAUST [101], in order to develop detailed kinetic mechanisms. These models were progressively refined to improve prediction of ignition delay times (IDTs) in shock tubes and rapid compression machines, as well as a wide range of pollutants in flow reactors (jet-stirred reactors and tubular reactors) [102]. Significant progress in these models was made by using theoretical calculations (ab initio methods) to predict thermochemical data and rate parameters [103]. Beginning in 2010, several studies updated the rate rules of reactions in the cycles of Fig. 1 from such calculations (Refs. [104-108]). This improved the accuracy of the models, such as those developed in Nancy [107, 108] for C_3-C_4 alkanes and in Galway and KAUST [88, 109-114] for C_{5+} alkanes. The Galway models were derived from those generated in the 90s by Curran et al. [98] at Lawrence Livermore National Laboratory. Two recent Galway models are specifically mentioned here: Bugler et al. for *n*-pentane [111] and Zhang et al. for *n*-heptane [88].

These detailed mechanisms were built using reaction classes and kinetic rate rules, which are well defined for C_{3+} alkanes [110, 115-117], and can also be established for alkenes [118, 119], ethers [120], or other large oxygenated species, such as alcohols [121] or aldehydes [122]. For small oxygenated and unsaturated compounds that can be produced from alkane oxidation, the definition of reaction classes is more complicated and some specific reactions frequently need to be considered. These reactions are gathered in a dedicated reaction basis, or core mechanism, and inserted as part of any alkane oxidation mechanism. In recent alkane mechanisms from Galway [88, 111], this core mechanism is the AramcoMech 2.0 [118], which notably includes reactions for C_2-C_4 alkenes and aldehydes.

To clarify the level of agreement that can be expected when using these recent models to predict routine low-temperature oxidation products, Fig. 4 compares the simulated mole fraction profiles of several important species with the experimental measurements.

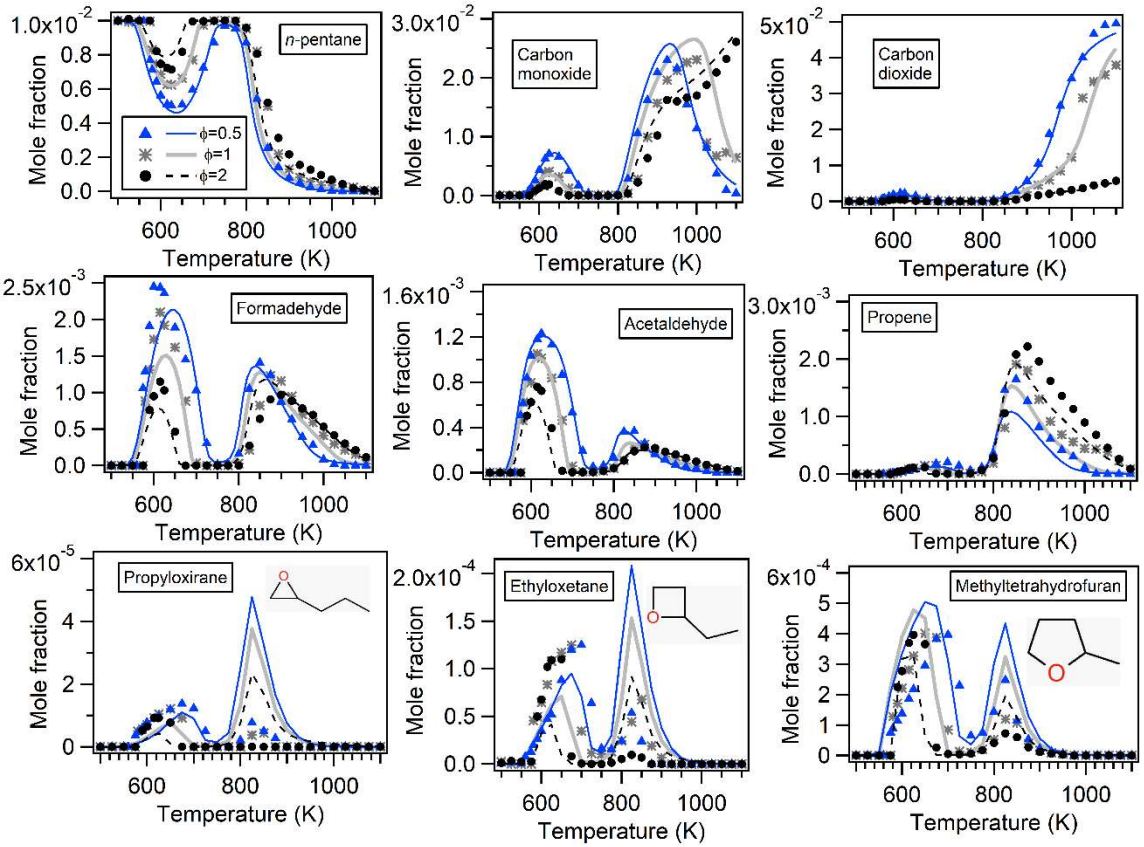

Figure 4: Comparison between model predictions [111] and experimental results in JSR oxidation of *n*-pentane at three equivalence ratios, initial fuel mole fraction = 0.01, pressure 106.7 kPa, and residence time of 2 s. Reactant and products quantified by GC – drawn from Supplementary Material in Bugler et al. [111].

The experiment was conducted in a jet-stirred reactor (JSR) at atmospheric pressure and a residence time of 2s. Bugler et al. [111] initially developed the model to predict the ignition delay times of pentane isomers [109]. This figure shows that, in the range of equivalence ratios studied from 0.5 to 2, the predictions were satisfactory for fuel and C_1-C_3 products (around 20% maximum deviation), but they deteriorated above 800 K for heavier products such as cyclic ethers. Nevertheless, the type and selectivity of the different ethers were well reproduced.

This paper focuses on recent progress toward the detection and quantification of hydroperoxides, and understanding their chemistry in combustion environments. The second part of this review summarizes the literature on hydroperoxide measurements and reaction mechanism developments up to 2010. The third section reviews progress and achievements in the detection and quantification of hydroperoxides during gas phase oxidation since 2010. In 2009, the pilot paper [123] in a series about hydroperoxide measurements in combustion experiments was published, marking the starting point of the third part of this review paper. The fourth section details advances in understanding hydroperoxide chemistry, which is flourishing with the recent detection of carboxylic acids, diones, and more complex hydroperoxides with up to five oxygen atoms added to the fuel molecule. The fifth and final section examines perspectives and offers a conclusion.

2 UNDERSTANDING HYDROPEROXIDE COMBUSTION CHEMISTRY: PROGRESS TO 2010

This section describes how the dominant role of KHPs in low-temperature oxidation (occurring before autoignition) of fuel components has been increasingly understood, and how the existence of hydroperoxides was first experimentally confirmed.

2.1 Mechanistic insights into the role of hydroperoxides in hydrocarbon oxidation

While the principles of branched chain reactions were well established by Semenov before 1960 [124, 125], the chemical structure of the branching agents involved in hydrocarbon oxidation was discovered considerably later. The roles of alkyl hydroperoxides and hydrogen peroxide in the occurrence of cool flame and ignition phenomena have been understood since 1961, from the work of Cartlidge and Tipper [126]. Their influence was later confirmed by Burgess and Laughlin [127], who added 2-heptylhydroperoxide during *n*-heptane oxidation in a static vessel and observed a significant reduction of the induction period before the cool flame.

The reactions involved in cycle 1 of Fig. 1 became well understood at the end of the 60's, after the papers of Knox in 1967 [128] and Fish in 1968 [129, 130]. In Pollard's review in 1977 [95], cycle 1 of Fig. 1, and the second oxygen addition, were well established, along with accountability for the formation of a wide range of cyclic ethers (oxiranes, oxetanes, tetrahydrofurans, tetrahydropyrans). However, the formation of KHPs in gas phase oxidation processes was not mentioned; instead, the branching agents derived from the second oxygen addition were considered to be alkyldihydroperoxides.

Following the work of Korcek and coworkers on liquid phase oxidation [82], a review by Benson in 1981 [131] mentioned the formation of alkyl hydroperoxides with a carbonyl function (i.e., KHPs) for C_6 or larger reactants. Such species were later mentioned in 1985 by Cox and Cole [132], who described their updated SHELL model [133] to simulate the autoignition of hydrocarbon air mixtures. In 1988, the manually written mechanism of *n*-butane oxidation by the groups of Westbrook and Cernansky [134] included a branching reaction leading to two ȮH radicals. The reaction began with an ȮOQOOH radical but did not include the KHPs. A more complete reaction mechanism (which included KHPs as the branching agents), has been developed since 1992. The representive works are alkane low-temperature oxidation by Chevalier et al. [135], Ranzi et al. [99], and Warth et al. [100]. These first attempts significantly clarified the determinant role of KHP in the modeling of low-temperature oxidation. A paper written in 1998 by Curran et al. [98], about the modeling of *n*-heptane oxidation, included KHPs in reaction class 23: "Isomerization of ȮOQOOH and formation of ketohydroperoxide and ȮH". Afterward, the reactions involved in cycle 2 of Fig. 1 became the standard for all hydrocarbon low-temperature oxidation models.

2.2 Hydroperoxide detection in hydrocarbon gas phase oxidation

As summarized above, several papers mentioned the analysis of hydroperoxides during gas phase oxidation in the 60's. Most importantly, the work by Cartlidge and Tipper [136] in 1960 described the measurement of 5-10% of butyl hydroperoxides during the *n*-butane oxidation between 588 and 618 K. The reaction was studied in a flow system and the products were analyzed by paper

chromatographic analysis [137]. In the same work [136], using cyclohexane as fuel, these authors found appreciable yields of the monohydroperoxide; the amounts of hydrogen peroxide were much smaller. Using *n*-heptane as a fuel, dihydroperoxyheptane and hydrogen peroxide were the main peroxides. Another study in 1967 by Burgess and Laughlin used an iodometric method to follow organic hydroperoxides during *n*-heptane cool-flame in a static vessel [127]. Following this pioneering work, Sahetchian's team at CNRS-Orsay obtained the next important results on hydroperoxide measurements. From 1988 to 1990, Sahetchian et al. [138, 139] measured hydroperoxides extracted from a motored cooperative fuel research (CFR) engine fueled with *n*-heptane. The CFR engine was first designed in 1928 as a test engine with adjustable compression ratio (from 4:1 to 10:1) and adjustable ignition timing [140]. This laboratory engine could be used as a reactor with high pressure and variable volume to study the low-temperature reactivity (before ignition) of the fuels by properly adjusting the intake temperature, pressure, compression ratio, inlet air temperature, fuel/air equivalence ratio, engine speed, etc. [141-145]. Low-temperature oxidation products were sampled from the exhaust line and analyzed by GC, Fourier-transform infrared (FTIR) spectroscopy [142-145], and recently by mass spectrometry [146].

In these experiments by Sahetchian et al. [138, 139], a microprobe was connected to a cold finger maintained at 77 K. After rinsing with methanol, the trapped compounds were analyzed using two chromatographic methods and the analytes were kept in the liquid phase: thin layer chromatography and high pressure liquid chromatography (HPLC). In addition to hydrogen peroxide, peracetic acid (CH_3COOOH), and alkyl hydroperoxides, the authors detected a compound bearing an -OOH group and a second polar function at compression ratio, just before autoignition, when using *n*-heptane. However, when using *n*-butane as the fuel, and under the same conditions [139], the absence of this hydroperoxide complex and the absence of the autoignition event, was observed.

In 1991, during a further study of *n*-heptane oxidation in a motored CFR engine and in a flow reactor, Sahetchian et al. [147] identified the hydroperoxide complex as a heptylketohydroperoxide. Their mass spectrometric analysis of the obtained methanol solution revealed a peak at m/z = 145, indicating a molecular weight of 146 and a compound with a formula $C_7H_{14}O_3$. Furthermore, the KHP structure was confirmed by infrared (IR) and ultraviolet (UV) spectroscopy. The IR spectrum showed a strong peak at 1414 cm^{-1}, characteristic of the carbonyl function of heptanone; and the UV absorption at 210 nm was consistent with the hydroperoxide function [147].

The same team revealed the presence of KHPs during the motored CFR engine oxidation of *n*-pentane and *n*-octane [148]. The KHPs appeared at compression ratios just before autoignition, and the heavier fuel molecule showed earlier in the cycle, where they were formed. In contrast, KHPs and autoignition were not observed during propane and *n*-butane oxidation.

In 2003, Sahetchian and coworkers [149] presented data obtained by electron ionization mass spectrometry (EI-MS) of the KHP isomers formed during *n*-hexane oxidation. In this work, the KHP was measured after trapping, rinsing with acetonitrile, and GC-MS analysis of the obtained acetonitrile solution. Figure 5 shows the mass spectrum obtained for

2-hexanone-4-hydroperoxide. The authors also reported a noticeable amount of hexadiones, a type of product not commonly considered at that time.

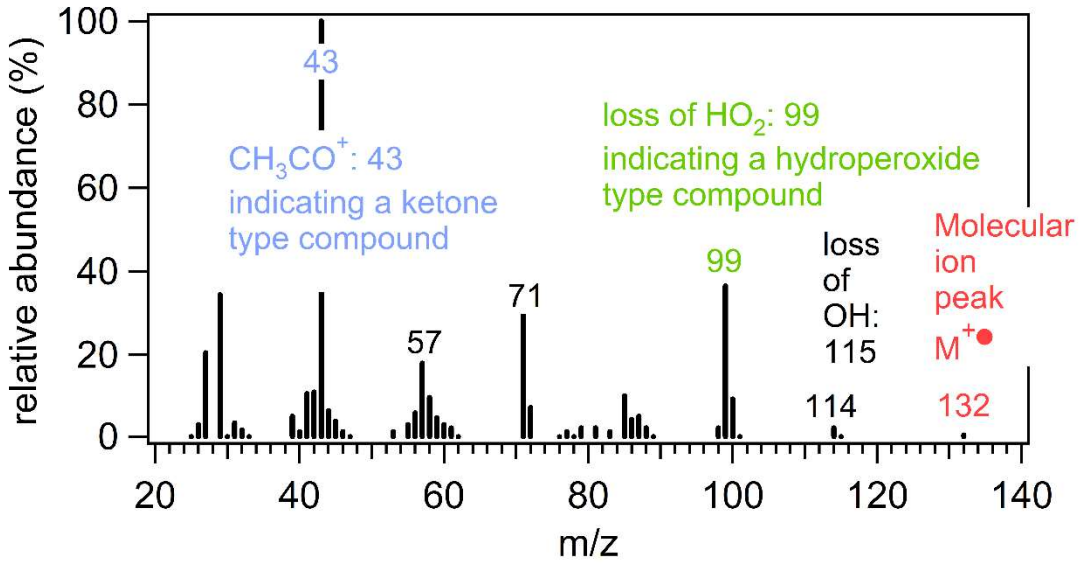

Figure 5: Interpretation of EI-MS spectrum of 2-hexanone-4-hydroperoxide formed during *n*-hexane oxidation at 548 K (500 ppm fuel in a N_2/O_2 mixture) in a flow reactor [149].

Further study of the gas phase oxidation of *n*-dodecane in a flow reactor [150] by the team of Sahetchian, reported the formation of polycarbonyl hydroperoxides, including four or more oxygen atoms, in addition to the formation of KHPs. The formation of dodecadiones was also mentioned.

After the previously described work of Sahetchian et al. [138, 139, 147-150], few other experiments were conducted to measure KHPs in the gas phase oxidation. While the gas phase oxidation mechanism based on cycle 2 of Fig. 1 has been widely accepted in detailed kinetic models of hydrocarbons, until 2010, the key assumption in these models --the formation of KHPs-- was supported only by the work of one team.

In 2005, a paper published in "Science" [151] brought awareness of the possibilities for species detection and identification by time-of-flight mass spectrometry with photoionization by synchrotron radiation. Based on this technique, Battin-Leclerc et al. [123] coupled a JSR with synchrotron radiation photoionization mass spectrometry at the National Synchrotron Radiation Laboratory (NSRL), University of Science and Technology of China in Hefei. During the low temperature oxidation of *n*-butane, the C_4-KHPs and the C_1-C_4 alkyl hydroperoxides were directly detected. Compared to the previous work of Sahetchian et al., the advantage of this advanced method lay in direct measurement of the hydroperoxides. This work offered new possibilities for more accurate quantification of individual hydroperoxides [152, 153].

In a subsequent paper [154], the authors reported a photoionization efficiency (PIE) curve (Fig. 6) for m/z = 104, which corresponds to possible KHPs produced in *n*-butane oxidation. The measured ionization energy of ~9.3 eV in Fig. 6 is close to the value derived from theoretical calculations [123], which were performed with the CBS-QB3 method [155], using Gaussian03

[156]. It was later determined that caution is necessary when interpreting the ionization thresholds of these flexible molecules for identification purposes, and additional information, such as fragmentation patterns, should also be taken into account [157].

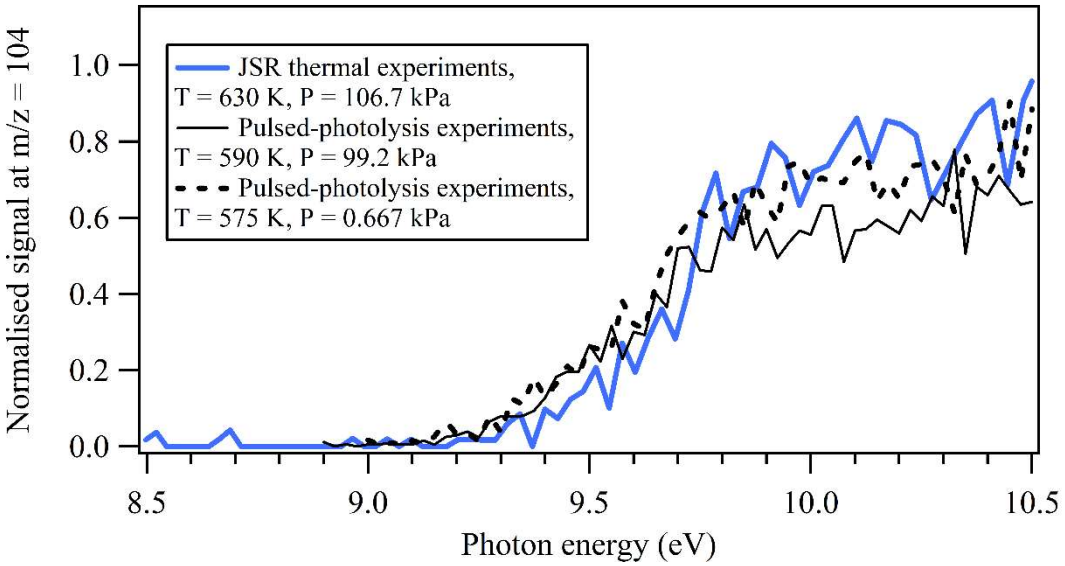

Figure 6: Photoionization efficiency curve of m/z 104 obtained during *n*-butane oxidation in JSR thermal [154] and flow reactor pulsed-photolysis [158] experiments.

In 2015, using the same mass spectrometry technique, Eskola et al. [158] confirmed this measurement at the Advanced Light Source, a synchrotron user facility at the Lawrence Berkeley National Laboratory, during *n*-butane oxidation and using pulsed-photolysis (PIE curve in Fig. 6). It can be seen that the two separate experiments produced similar results, suggesting that the major C_4 KHP isomers may be the same in thermal and photolysis experiments, and/or that the PIE curves are invariant of the isomeric structure.

The detection of the KHP in 2010, followed by confirmation in 2015, opened the door to a wide range of hydroperoxide measurements, as shown in the following section.

3 PROGRESS IN HYDROPEROXIDE DETECTION AND QUANTIFICATION SINCE 2010

This section is organized as follows: Section 3.1 describes the main experimental techniques used to measure the hydroperoxides. Section 3.2 summarizes the corresponding results in analyzing hydroperoxides, specifically addressing hydrogen peroxide, alkyl hydroperoxides, olefinic hydroperoxides, KHPs, and more complex hydroperoxides.

3.1 Advances in diagnostics for hydroperoxide analysis

The detection, identification and quantification of hydroperoxides in oxidation environments is not an easy task, given their reactivity, molecular size and stability. To this end, researchers have established a set of idealized reactors for controlled laboratory-scale experiments which are briefly described next. The two main types of analytical methods used to analyze these reactive species, formed in idealized systems, have been time-of-flight mass spectrometry and laser-based

absorption spectroscopy. While laser-based absorption spectroscopy can be applied to small hydroperoxides, the detection of KHPs has only become available with advanced mass spectrometry techniques [123].

3.1.1 Ideal reactors for controlled laboratory-scale oxidation experiments

To simulate real world environments, as found either in internal combustion engines or in the atmosphere, researchers routinely take advantage of several laboratory-scale reactor --plug flow and perfectly stirred reactors. Jet-stirred reactors (JSR) and flow tubes (FT) have been the two main reactor types used to study hydroperoxide chemistry in complex gas phase reactions -- especially in fuel oxidations [92]-- since 2010. These reactors are generally used under isothermal and isobaric conditions with a gas mixture continuously flowing inside. They are popular because they can be simulated by zero-dimensional models. The dilution by inert gas in these reactors is kept large enough to avoid significant temperature gradients inside the reactor due to the oxidation exothermicity [159].

A FT consists of a cylindrical tube located in an oven in which a flow of gaseous fuel is injected into a laminar or turbulent flow of a diluent/oxygen mixture [160]. While pressures as high as 10 MPa have been used, the typical pressure in FT experiments is 100 kPa, with typical residence times ranging from 10 ms to 20 s [161, 162]. With a suitable design, FTs can be modeled as plug flow reactors [163], but it is advisable to consider the experimental temperature profile when running simulations. FTs that can easily be made from alumina have already been used at temperatures as high as 1800 K [164].

Due to their complex geometry, JSRs are usually made from fused silica, which limits their maximum accessible temperature to ~ 1200 K [159]. A JSR consists of a heated sphere in which rapid mixing is achieved by four turbulent jets located near the center of an injection cross. The injection cross is in the middle of the sphere, attached to a preheating zone with negligible volume compared to the sphere [159]. Typical pressures in JSR experiments range from 100 kPa [154] to 1 MPa [165], but oxidation experiments were also performed at higher pressures (up to 4 MPa [166]). Typical residence times range from 0.1 to 10s [167], according to reactor geometry. Using the design proposed by Ref. [168], a JSR can be modeled as a perfectly stirred reactor. During the JSR oxidation of C_{3+} hydrocarbons, the temperature-dependent mole fraction profiles of reactants usually indicate three reactivity zones: one below 650 K, one between 650 and 800 K, and one above 800 K [153]. This is clearly visible in Fig. 4 for *n*-pentane oxidation. The first reactivity zone corresponds to the low-temperature chemistry, which is governed by cycle 2 of Fig. 1. The second zone is the NTC zone, in which cycle 1 and HOȮ radical formation are dominant.

Reactivity above 800 K is due to high-temperature chemistry triggered by the decomposition of H_2O_2. These three reactivity zones result in the temperature dependence of most products exhibiting two peaks (see CO, aldehydes, propene and cyclic ethers in Fig. 4): a first peak occurs when the low-temperature reactivity is maximum; a second peak is produced when the rate of fuel consumption at high temperatures is maximum.

Analyses of the complex products formed during low-temperature oxidation studies in JSRs and FTs are usually performed by GC and FTIR spectroscopy, such as the work by CNRS-Nancy [159], CNRS-Orléans [159], Princeton University [169], and KAUST [170]. However, these two diagnostic techniques are not generally suitable for direct analysis of the hydroperoxide products, instead, JSRs and FTs are coupled with two other types of analytical methods --time-of-flight mass spectrometry techniques and infrared cavity ring-down spectroscopy.

3.1.2 Advanced mass spectrometry techniques

Mass spectrometry is a universal diagnostic tool based on determining a molecule's mass-to charge (m/z) ratio after an ionization process; it has been applied to detect hydroperoxide species in several laboratories [152, 157, 171-173]. It is a highly multiplexed technique that allows for sensitive detection of all species simultaneously without prior knowledge of their chemical identities and as such, it is very useful for determining mixture compositions [152, 174-176]. Although mass spectrometry primarily determines the mass of a particular molecule, structural information can be obtained through observations of molecule-specific fragmentation patterns and appearance energies.

Described first are some experimental aspects that should be considered when employing mass spectrometry for detection, identification, and --in some cases-- quantification of hydroperoxide species in reactive environments. The steps to convert mass spectra into quantitative species concentrations are discussed in the section that follows.

3.1.2.1 Experimental aspects of mass spectroscopy for hydroperoxide analysis

The goal being to provide accurate quantitative measurements of hydroperoxide intermediate concentrations in reactive environments, and given the species' reactivities, it is challenging to quantitatively transfer these reactive intermediates into the ionization region of the mass spectrometer. One possibility is to sample the gaseous components through molecular beam expansion [177-179], out of the reactive environments and into the higher vacuum of a mass spectrometer (Fig. 7). This approach is typically implemented by sampling, via a small pin hole and a pressure drop between the reactor and the inlet of the mass spectrometer.

In such a molecular beam --guided towards the ionization region of the mass spectrometer-- all sampled molecules fly with basically the same velocity, precluding further collisions and reactions among its components, and the highly reactive species, like hydroperoxides, are preserved. Using this approach, the chemical composition at the sampling location is nearly identical to that of the molecular beam in the ionization region of the mass spectrometer, enabling quantitative measurements with this technique. The accuracy of these measurements depends on many different parameters. In flame sampling experiments, which use a similar experimental configuration, it was shown that although substantial cooling of the vibrational temperature was observed, the molecular beam did not fall clearly in either of the limiting cases (effusive or supersonic [181]). Thus, this technique enables accurate measurements, ensuring that the chemical composition at the sampling location is identical to the composition of the molecular beam in the ionization region of the mass spectrometer.

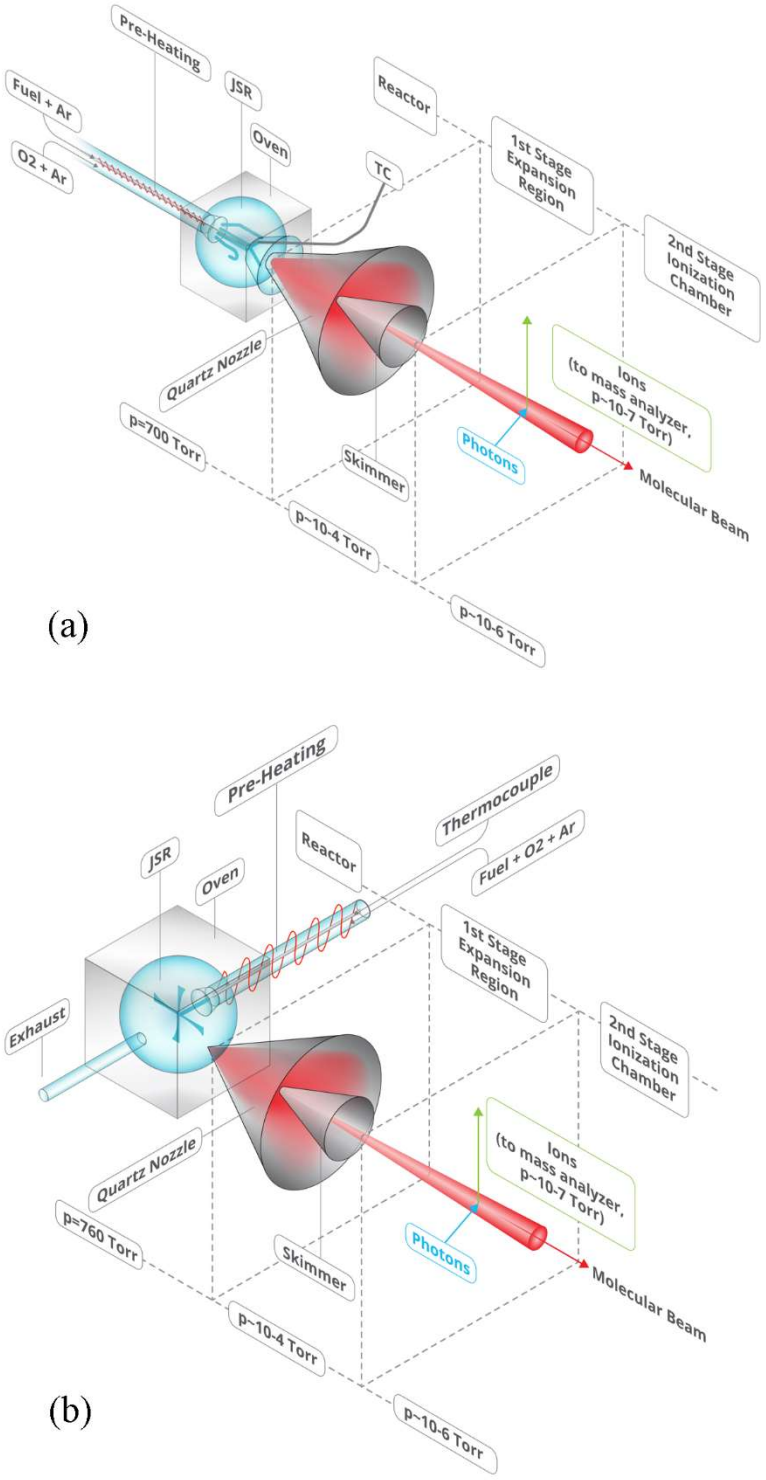

Figure 7: Schematic description of coupling between a JSR and SVUV-PIMS (a) in Sandia [180] and (b) in Hefei [123]. Pressure at different stages of the PIMS is given (1 Torr ≈ 133.3 Pa). TC in Fig. 7a is thermocouple.

Figure 7 shows the two setups established at Sandia [180] and Hefei [123]. Although both models use molecular-beam mass spectrometry with tunable synchrotron vacuum-ultraviolet photoionization (SVUV-PIMS) as a diagnostic, the reactor design and the sampling position are different. The design of the Hefei JSR follows the work of CNRS-Nancy [153] while Sandia JSR

relates to the work of CNRS-Orléans [166]. The major difference between the two reactors lies in the preheating section. In the Hefei JSR, the reactant/O_2/dilution gas mixture is premixed in the preheating annular tube, whose volume is a few percent of the JSR. In the Sandia JSR, the reactant/dilution gases are preheated in an inner annular tube and the O_2/dilution gases are preheated in an outer annular tube. The reactant/O_2/dilution gas mixture is mixed at a positon usually 30 mm away from the inlet of the reactor. Another major difference between the two models is the sampling cone and the sampling position. In the Hefei JSR, the quartz cone is fused within the JSR and inserted inside the sphere of the reactor. The connection point is at the side wall of the reactor. For the Sandia model, the cone is inserted into the outlet of the reactor, but the two pieces are not fused together. Finally, the position of the thermocouple that measures the reactor temperature is also different. In the Hefei JSR, the thermocouple is located inside the intra annular space of the preheating zone, its extremity is on the level of the injection cross. The thermocouple in the Sandia JSR is fixed at the tip of the sampling cone. The cooling effect of the sampling causes the measured temperature to be slightly lower than the reaction temperature inside the JSR.

At Princeton University, two studies showed hydrogen peroxide measurements using a tubular reactor coupled with a molecular beam EI-MS diagnostic [182, 183]. The ionization energy used (i.e., 30 eV) was too high to detect organic hydroperoxides.

In another approach [119, 171, 184] at CNRS-Nancy, gas mixtures from a JSR were sampled and transferred through a capillary tube into the ionization region of the mass spectrometer. While reactions between the sampled gaseous components were not stopped, reliable quantitative information could still be obtained when the residence time in the transfer line was maintained at much less than the mean residence time in the reactors. This approach has been combined with laser-based ionization techniques. The JSR used at CNRS-Nancy with MS, GC and CRDS (cavity ring-down spectroscopy, Section 3.1.3) has the same geometry as that used in Hefei with SVUV-PIMS. For comparison purposes, both reactors were often used under the same operating conditions.

For the ionization of gaseous species, several different ionization techniques are employed in mass spectrometry. Most commonly, the gaseous species are ionized via removal of the most-weakly bound valence electron after interactions with energetic electrons (electron ionization, EI) or photons (photon ionization, PI). In the PI technique, tools have become available that are either based on laser or synchrotron-generated radiation. The advantages and disadvantages of the EI and PI techniques in combustion chemistry research have been described in detail in Ref. [176] and are briefly summarised hereafter. Ionization of the sampled species can be alternatively achieved via gas phase ion molecule reactions at atmospheric pressures (atmospheric pressure chemical ionization, APCI). APCI is a soft ionization technique in which the species are typically ionized through a proton transfer onto the targeted molecule. The model used at KAUST, where the JSR and the APCI source are combined with an orbitrap mass spectrometer (OTMS), is shown in Fig. 8.

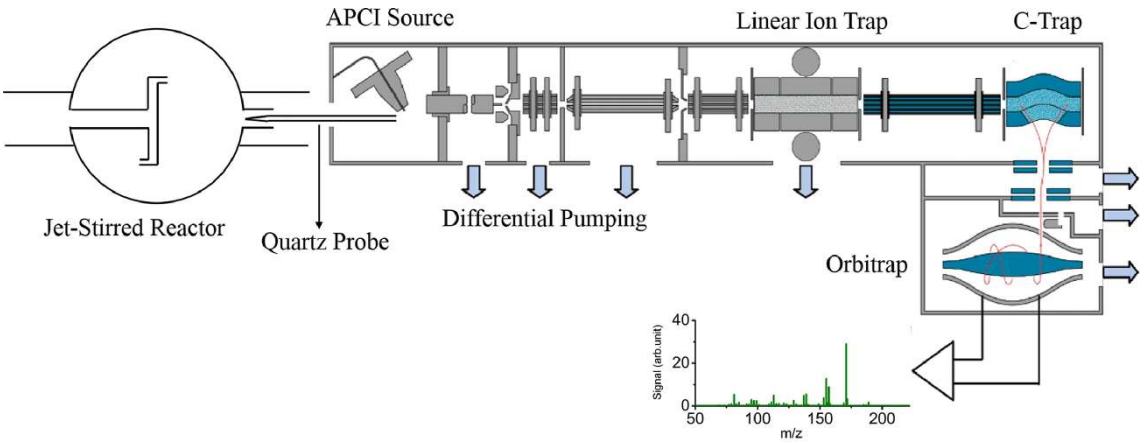

Figure 8: Schematic representation of an APCI mass spectrometer used for JSR sampling and analysis – reproduced from Ref. [146] with permission of Elsevier.

For the detection of hydroperoxide species, the PI and APCI techniques have proven to be very successful [172]. Compared to the EI technique (which suffers partly from the large width of the electron's energy distribution), APCI and PI have the advantage of avoiding fragmentation under special experimental conditions. For the photoionization of hydroperoxide species, energies in the range from 8 to 10 eV are typically necessary. Photons in this energy range can be generated using non-linear mixing schemes in a laser laboratory (at CNRS-Nancy [171]), or at vacuum-ultraviolet (VUV) beamlines at synchrotrons found at the Advanced Light Source in Berkeley (USA) [185], the National Synchrotron Radiation Laboratory in Hefei (China) [186-188], the Swiss Light

Source at the Paul-Scherrer Institute (Switzerland) [189], and at SOLEIL (France) [190]. The wide-range tunability and the high photon flux of synchrotron-generated VUV photons are unmatched by laser-based PI techniques, providing an advantage for sensitive species detection and their identification, based on so-called PIE curves. The possibility to ionize near a molecule's ionization threshold can especially minimize complications when interpreting the mass spectra. However, it should also be pointed out that fragmentation can be used (as discussed by Moshammer et al. [157]), for species identification.

In the four mass spectrometers which were extensively used to analyse hydroperoxides (CNRS Nancy, USTC, Sandia, and KAUST), the separation of the created ions was based on either their respective flight time to the detector (time-of-flight mass spectrometry), or on an orbitrap. These mass spectrometers offer a wide range of resolving power and are suitable for separating oxygenated from hydrocarbon species. Mass resolutions of $m/\Delta m$ of ~2000 (CNRS-Nancy), ~2500 (USTC), ~4000 (Sandia), 105 (KAUST) are typically achieved. To avoid confusion about the different mass resolution of the various instruments, the m/z ratio of the targeted species is given only as the nominal mass throughout this manuscript.

In addition to detection of the hydroperoxide species based on m/z ratio, mass spectrometry also allows for the identification of the molecular structure of the detected species. First, to analyze the fragmentation pattern (arguably difficult to identify in mass spectra obtained from complex reaction mixtures), the combination of mass spectrometric detection with synchrotron generated, tunable VUV radiation for ionization and high-level ab-initio calculations have proven to be very

successful. The ability to experimentally determine ionization and fragment appearance energies via the PIE curves is unmatched by any other ionization technique. Because of the substantial vibrational cooling in the molecular beam, the internal energy of the targeted species is small and thresholds for reactor-sampled and room temperature PIE curves have been found to be identical in shape, within the experimental signal to noise ratios. Hot-bands are not typically observed and the internal energy of the targeted species does not affect the species' assignments [154, 157]. For example, Moshammer et al. [157] clearly identified the hydroperoxymethylformate (HPMF, $HOOCH_2OCHO$) as the KHP produced in the low-temperature oxidation of dimethyl ether (DME) in a jet-stirred reactor by matching the observed ionization and fragment appearance energies to calculated values (Fig. 9).

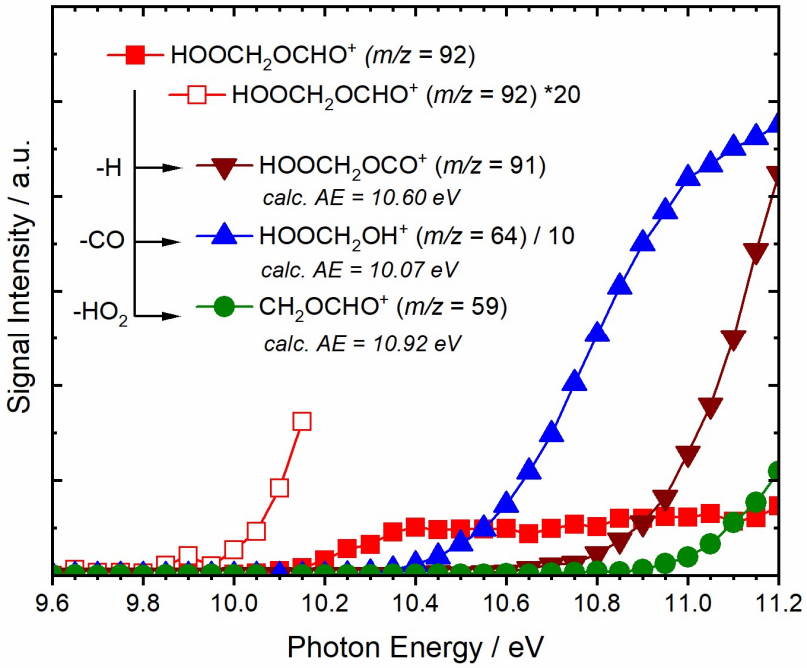

Figure 9: Photoionization efficiency curves of m/z = 92 ($C_2H_4O_4$), identifiable as the hydroperoxyl methylformate (HPMF) via its ionization energy and the appearance energies of the ion fragmentation channels leading to $C_2H_3O_4$ (m/z = 91), CH_4O_3 (m/z = 64), and $C_2H_3O_2$ (m/z = 59) measured by SVUV-PIMS during dimethyl ether JSR oxidation – Adapted from results of Ref. [157].

As noted in Ref. [157], it is necessary to emphasize the conformeric structures when assigning PIE curves to structural isomers, adding complexity to the data analysis and interpretation. While the work of Moshammer et al. [157] clearly benefited from the fact that only one possible isomeric form of the KHP exists, it also showed its limitations in assigning isomeric structures for other systems. This technical approach is fine for small hydroperoxide species, including H_2O_2 and CH_3OOH, and these small molecules can easily be assigned for molecular structures. However, even with this state-of-the-art diagnostic, the assignment for larger molecules should also be based on chemical intuition, not on PIE curves alone. In the future, new analytical mass spectrometry tools might become available to overcome these limitations. These techniques are likely to include photoelectron photoion coincidence (PEPICO) or Tandem MS, as already successfully implemented for combustion research [189-194].

3.1.2.2 Conversion of mass spectra into quantitative species concentrations

Strategies to convert mass spectra into quantitative species concentration profiles have been developed for PI techniques [174, 180, 195-197]. For EI mass spectrometry, Guo et al. [173] used a direct calibration method to quantify H_2O_2 during the FT oxidation of DME. In the case of APCI mass spectrometry, it has not been applied to quantify hydroperoxide species; therefore, only strategies to obtain quantitative information based on the PI techniques are described here. The quantification strategies are based on the fact that the targeted species mole fraction is correlated to the observed signal intensity by the following relationship:

$$x_i(T) = S_i(T,E)/[\sigma_i(E) \times \Phi(E) \times SW \times MDF_i \times c \times FKT(T)] \quad \text{Eq. (1)}$$

In Eq. (1), $x_i(T)$ is the mole fraction of species i at a given temperature T, $S_i(T,E)$ is the energy dependent total ion signal related to the targeted species, $\sigma_i(E)$ is the ionization cross-section at a given photon energy, $\Phi(E)$ is the photon flux, SW is the number of mass spectral accumulations (sweeps), MDF_i is the mass discrimination factor, c is a calibration constant, and $FKT(T)$ is a temperature-dependent sampling function.

Sometimes it is sufficient --and more convenient-- to report the ratio of the target species mole fraction to a known reference species. Eq. (1) can then be rewritten as:

$$x_i(T)/x_{ref}(T) = S_i(T,E)/S_{ref}(T,E) \times \sigma_{ref}(E)/\sigma_i(E) \times MDF_{ref} \times MDF_i \quad \text{Eq. (2)}$$

With this approach, uncertainties associated with the accurate measurement of the photon flux and the determination of $c \times FKT(T)$ are eliminated. More importantly, such an approach allows quantification of the laser-based single-photon ionization mass spectra when access to the Ar signal (normally used as the calibration standard) is not accessible because the photon energy of 10.6 eV is below the argon ionization energy. For example, Rodriguez et al. (*n*-pentane [171], *n*-heptane/*n*-decane [184]) and Meng et al. (1-hexene [119]) used propene as a reference species, with its concentration determined from accompanying GC measurements.

When all the parameters are known, Eq. (1) can be used to directly calculate the mole fraction $x_i(T)$. For this, $\Phi(E)$ is measured, using a calibrated photodiode. Mass discrimination factors (which correct for a m/z-dependent detection efficiency), are typically measured using calibrated gas mixtures, covering the range from m/z = 2 (H_2) to m/z = 136 (Xe). $\sigma_i(E)$ is either taken from the literature, newly measured, and estimated based on similar structures, or it is calculated using a theoretical framework. The sampling function FKT and calibration constant c are determined from the experimental data, taking into account the known inlet flow conditions and the mass balance.

There are a couple of challenges associated with the quantification of the peroxide species: a) These compounds tend to be unstable under ambient conditions and, with the exception of H_2O_2 and HO_2 [198], experimentally determined photoionization cross-sections for peroxide species are not available. b) The fragmentation patterns of the peroxide ions are vastly unknown,

complicating quantification procedures, since the total photoionization cross-sections must be correlated to the total ion count that corresponds to the sum of the parent and fragment ions.

Theoretical frameworks have been developed to overcome the challenges in determining photoionization cross-sections of unstable species. Based on work from Bobeldijk et al. [199], photoionization cross-sections can be estimated using group additivity theory; however, because of what follows, the additivity rule appears to result in cross-sections that are usually too large, i.e. the experimentally determined peroxide mole fractions are too small. Nevertheless, this approach has been used (for example in Ref. [171]), for the quantification of hydroperoxides in *n*-pentane oxidation. This resulted in determination within a factor 2.5 of the mole fractions of methyl hydroperoxide (cross-section ~4 Mb at 10.6 eV) and ethyl hydroperoxide (cross-section ~5 Mb) compared to the modeling results [111]. Significantly more major underdetermination of the experimental mole fraction --a factor ~ 125-- was found for KHPs with cross-section ~15 Mb.

In an alternative approach, routines to quantum-chemically calculate photoionization cross sections have been developed [200-208]. Moshammer et al. [180] used routines from Lucchese and coworkers for the quantification of methyl hydroperoxide and hydroperoxymethylformate (HPMF) in a dimethyl ether (DME) low-temperature oxidation study. Following a large set of test cases [180], it was concluded that this theoretical approach resulted in cross-sections that were good within a factor of two. In the DME oxidation study [180], calculated cross-sections for CH_3OOH and HPMF were ~6 Mb at energies up to 2 eV above the ionization energy (Fig. 10(a) and (c)). It is noted that discrepancies in the results from the group additivity rules (Bobeldijk et al. [199]) can exist. Following the procedures of Bobeldijk et al. [199], the group additivity rules resulted in cross-sections at 11.8 eV of 9 Mb for CH_3OOH and 40 Mb for the HPMF. The result of the theoretically derived ionization cross-section is comparable to that of the group additivity of CH_3OOH; the group additivity leads to an unusually large cross-section for the more complex HPMF molecule which seems to be outside the expected uncertainty of the theoretically derived value. For H_2O_2 a large energy-dependence of the photoionization cross-section was observed, largely due to the involvement of a low-lying excited electronic state of H_2O_2 (see Supplementary Material of Ref. [180]).

Until now, these quantum-chemical routines have not been coupled with Franck-Condon overlap calculations (a future research topic), considering the large-amplitude motions in these peroxide species. Therefore, Moshammer et al. [180] normalized the experimentally determined PIE curves to the theoretically predicted value as shown here in Figs. 10(a) and (c).

Using this approach, methyl hydroperoxide was quantified, and, as shown in Fig. 10(b), the experimentally determined mole fraction agreed reasonably well with the modeled value, using an up-to-date chemically detailed kinetic model. The same procedures were applied by Tao et al. [197] to quantify the methyl hydroperoxide and its corresponding methyl hydroperoxyl radical during the low-temperature oxidation of acetaldehyde.

The situation for quantifying KHPs is more complicated because fragmentation patterns of the peroxide ions must be considered; this is because both the additivity rules and quantum-chemically calculated cross-sections typically result in total photoionization cross-sections.

Therefore, the identification of fragment ions in the complex mass spectra is important. This can be achieved using chemical intuition or experimentally observed appearance energies and comparison with theoretical calculations. For example, for the quantification of the HPMF in the DME low temperature oxidation, it was essential to identify the -H, -CO, -HOO fragmentation channels which then contributed to the total ion count of HPMF (Figs. 9 and 10(c)). The total ion count for the targeted species is then the sum of the ions observed at the m/z of the parent ion and at the respective masses of the fragments. Using the same normalization strategy for methyl hydroperoxide (i.e. normalizing the experimental PIE curve onto the calculated photoionization cross section), allowed for a quantification of HPMF, resulting in mole fractions that were in reasonable agreement with up-to-date kinetic model calculations (Fig. 10(d)).

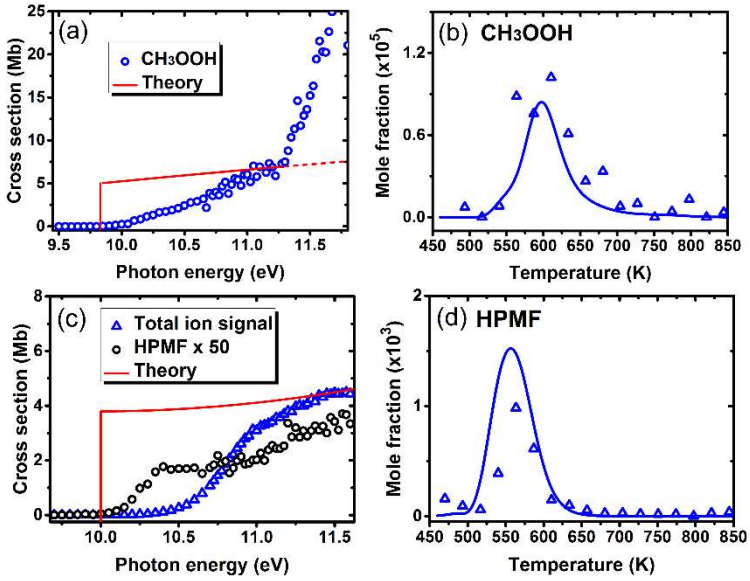

Figure 10: Photoionization cross-section and mole fraction profile of methyl hydroperoxide (CH_3OOH) and hydroperoxyl methylformate (HPMF, $HOOCH_2OCHO$) measured by SVUV-PIMS during DME JSR oxidation: (a) and (c) calculated photoionization cross-section and scaled experimental PIE curve; (b) and (d) mole fractions as function of temperature. Total ion signal in (c) is the sum of the signal at the m/z of the parent ion and respective fragments (details in part 3.2.4). Symbols are experiments; lines are computations using the model of Ref. [120] (predicted values divided by 5 in (d)) – adapted from the results of Ref. [180].

3.1.3 Infrared cavity ring-down spectroscopy

Cavity ring-down spectroscopy (CRDS) is a highly sensitive direct absorption technique based on the rate of absorption of the light confined in an optical cavity, which consists of two highly reflective mirrors (CRDS mirrors usually have a selectivity around 0.99997) fixed at each end of a cell. The high sensitivity is obtained by trapping an absorbed laser beam inside the cell and by the corresponding high value of the length of the optical path: e.g., an 80 cm cell can have an actual optical path of around 100 km.

Due to its high sensitivity and relatively low cost, this technique is widely used in many research areas, mainly in physical, analytical and atmospheric chemistries, but also in biology, medicine, environmental and combustion chemistry [209]. CRDS has become the technique of choice for

detection of species important in the atmosphere [210-213] --even those present in trace amounts.

This section describes how CRDS was used to identify and quantify reaction products and how this technique was applied to study hydrogen peroxide formation during low-temperature oxidation of fuels. The low-temperature oxidation studies that have used CRDS to date are also listed.

3.1.3.1 Spectroscopic method applied to low-temperature oxidation studies

Cavity ring-down spectroscopy has been used in the field of combustion chemistry since the mid 90's to probe various species --even reactive species like hydroxyl radicals in flames [214-216]. It was also used to measure the absolute volume fraction of soot particles in flames [217]. Several types of CRDS are used, they differ mainly by the light source used. Standard pulsed CRDS (using a pulsed laser) are easiest to use; however, the continuous wave CRDS (cw-CRDS), using a constant laser with lower bandwidth, allows single longitudinal mode excitation and is frequently utilized. The cw-CRDS has higher sensitivity, repetition rate and spectral resolution than standard pulsed CRDS [218].

The sensitivity of CRDS depends mainly on the length of the optical path in the cell. In optimal conditions, and due to the trapping of the absorbed laser beam inside the cavity, a CRDS technique can have a sensitivity 107 times better than a single path absorption technique [219]. Application of cw-CRDS to the study of the low-temperature oxidation of hydrocarbons and biofuels is quite recent. This type of experiment has two components, a cw-CRDS cell, functioning with an infrared diode laser, and a JSR. To our knowledge, two experimental set-up based on CRDS have been currently developed to study fuel oxidation. The first was developed at CNRS-Nancy in collaboration with the University of Lille [220]. Some years later, another model was built at CNRS-Orléans [221]. These two experimental set-up are very similar. The main difference is the sampling method: a sonic probe is used in Nancy and a sampling cone is implemented in Orléans. As described hereafter, hydrogen peroxide was successfully detected using both experimental set up. Another difference is the wavelength range used for the measurements: typically 6638-6643 cm^{-1} at CNRS-Nancy, and 6623-6626 cm^{-1} at CNRS-Orléans. Figure 11 shows the setup at CNRS Nancy. The cw-CRDS cell is a glass tube with the two mirrors located at each end of a cylindrical cell.

Although it uses a continuous-wave (cw) diode laser, the so-called cw-CRDS method at Nancy is not really a continuous-wave technique; the laser light provided by a diode laser (in the 6624-6647 cm^{-1} range) passed through an acousto-optic modulator (AOM). The AOM was triggered by an avalanche photodiode that detects light emitted by the cavity. The first order diffracted beam was sent to the cell and rapidly extinguished when the photo-detector found a strong signal from the cavity (when the resonance occurred). During this time, the decrease of the signal due to species absorption was recorded as a function of time. The ring-down time was extracted from the signal decay by performing a Levenberg-Marquardt exponential fit.

A fused silica tube sonic probe with a ~100 µm pin hole at its tip (Fig. 11) performed the sampling inside the gas phase of the reactor. The probe created the required pressure drop between the reactor (operated at slightly above atmospheric pressure), and the cell which was under partial vacuum (between 1.33 and 6.67 kPa). The gas expansion in the probe froze the reaction [159].

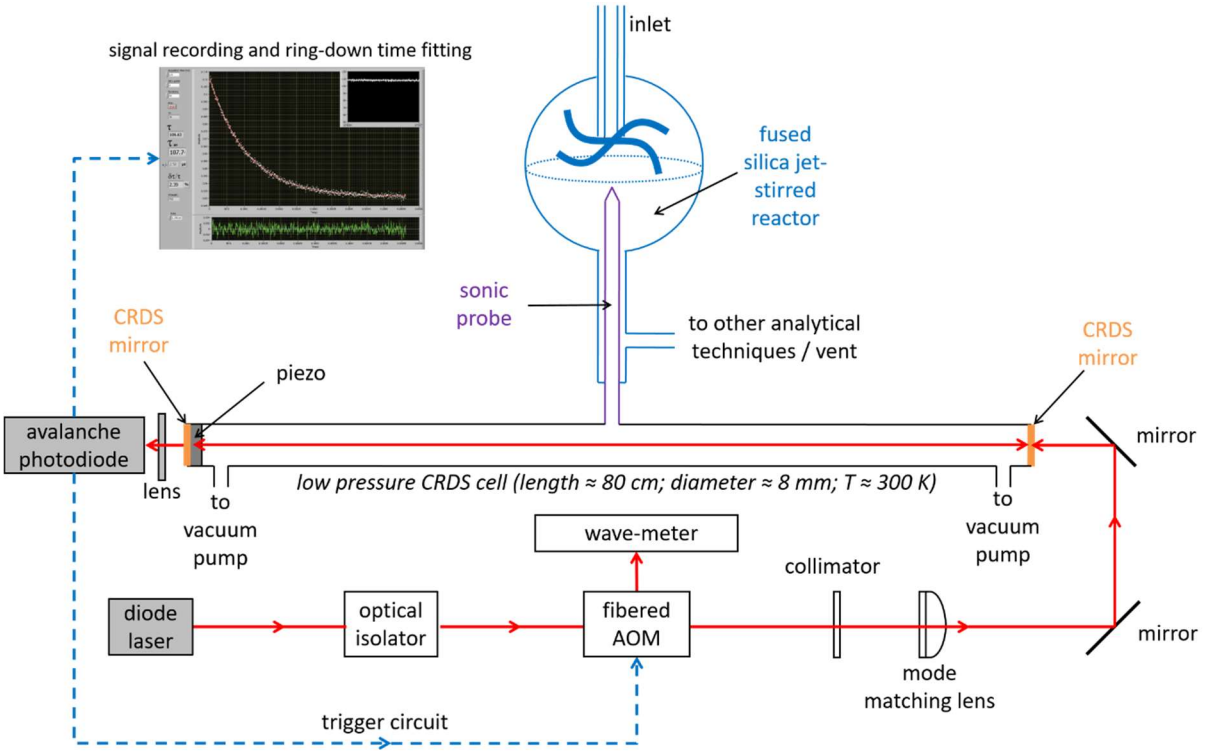

Figure 11: cw-CRDS setup used at CNRS-Nancy.

3.1.3.2 Identification and quantification of reaction products

Figure 12 displays the spectrum recorded in the 6638-6642 cm^{-1} range during the oxidation study of dimethylether [120]. Additional spectra recorded for water, hydrogen peroxide/water solution, and a spectrum of formaldehyde [222] from the literature, are also presented. This figure illustrates the difficulty in identifying isolated peaks in combustion mixtures where many absorbing products are present. Symbols in the panels of Fig.12 correspond to peaks used for the detection of the given species.

When the peaks have been selected for the quantification, frequency-specific absorption coefficients $\alpha(\upsilon)$ can be calculated from the ring-down time using Eq. (3):

$$\alpha(\upsilon) = \frac{R_L}{c}\left(\frac{1}{\tau(\upsilon)} - \frac{1}{\tau_0(\upsilon)}\right) \qquad \text{Eq. (3)}$$

where R_L is the ratio of the cavity length (i.e. the distance between the two cavity mirrors) to the length of the absorption cell, c is the speed of light, $\tau(\upsilon)$ and $\tau_0(\upsilon)$ are the ring-down times measured with the cell containing species A and with an empty cell, respectively. In the Nancy setup, the $R_L \approx 1$.

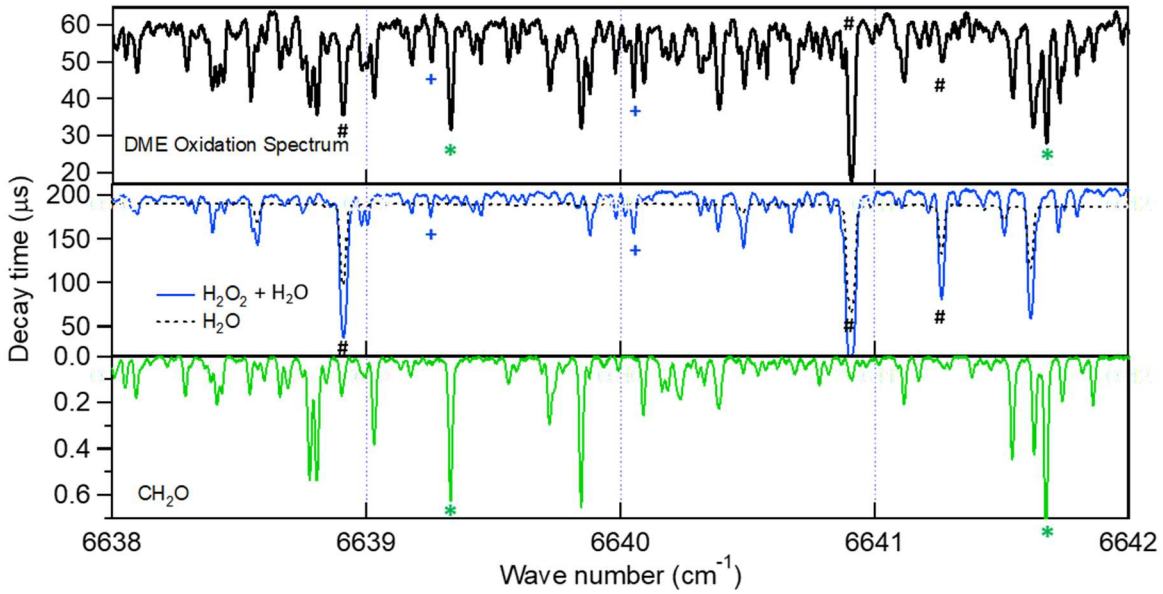

Figure 12: Spectrum recorded during JSR oxidation of dimethylether (top) at 625 K [120]. Identification of peaks using spectra recorded for water (black #), hydrogen peroxide (blue crosses) (middle), and formaldehyde (green stars) [222] (bottom). Symbols denote peaks used for species quantification.

The concentration of the species A is deduced from $\alpha(\upsilon)$ and from the value of the absorption cross-section of species A at the considered wavelength using Eq. (4):

$$\alpha(\upsilon) = [A] \times \sigma(\upsilon) \qquad \text{Eq. (4)},$$

where [A] is the concentration of species A and $\alpha(\upsilon)$ is the absorption cross-section of species A. One major advantage of this technique is that the absorption cross-section is an absolute value. It depends only on the wavelength υ and can be measured independently from the setups. For example, the cross-section used for the quantification of hydrogen peroxide in all the experiments performed at CNRS-Nancy (Section 3.2.1) was taken from the measurements of Parker et al. [223]. In this work, hydrogen peroxide absorption cross-sections were obtained by the combination of spectroscopic and kinetic measurements of ȮH and HOȮ radicals, produced by the photolysis of H_2O_2 at 248 nm. Time-resolved measurements of ȮH and HOȮ radicals by laser-induced fluorescence were used to determine the initial hydrogen peroxide concentrations, the absorption cross-sections were then derived from the absorption coefficients. Note that peak broadening was observed when the pressure in the cell increased. Because the temperature is given (room temperature), the temperature dependence of the cross-section is not important.

The theoretical detection limit α_{min} depends on the mirror reflectivity R, the length of the cell L, and the minimum relative variation of the ring down time that can be detected, $\left(\frac{\Delta\tau}{\tau}\right)_{min}$:

$$\alpha_{min} = \frac{1-R}{L} \times \left(\frac{\Delta\tau}{\tau}\right)_{min} \qquad \text{Eq. (5)},$$

For conditions usually used in combustion studies [220] (e.g., a reflectivity of 99.99%, a cavity length of 70 cm, and a $\left(\frac{\Delta\tau}{\tau}\right)_{min}$ of 1%), the α_{min} is close to $1.4.10^{-8}$ cm^{-1}. This corresponds to a concentration of about 50 ppm when detecting formaldehyde using the peak at 6639.33 cm^{-1}. However, this detection limit can significantly decrease under less than ideal conditions. For example, when the spectra are crowded with very close peaks, and when the baseline around the quantified peak is not well defined.

3.1.3.3 Low-temperature oxidation studies performed using cw-CRDS

Table 2 summarizes published studies on fuel oxidation using a JSR and cw-CRDS. Several species (CH_4, H_2O, H_2O_2, CH_2O, C_2H_4, and HOȮ radical) can be measured by CRDS, with careful selection of the wavelengths. The first study using CRDS for low-temperature oxidation focused on the detection of intermediates during the oxidation of methane [220]. The detected species were formaldehyde, methane, and water. Hydrogen peroxide was not detected in this study, because its concentrations were below the estimated detection limit of 130 ppm. Hydrogen peroxide was detected by CRDS in the following studies with fuels like *n*-butane [221, 224, 225], dimethylether [120, 226], and heavier organic reactants [119, 122, 171, 184] of *n*-pentane, *n*-heptane, 1-hexene, and *n*-hexanal. However, the attempt to detect hydrogen peroxide was not successful in *n*-decane oxidation [184]; according to the analysis, this was caused by condensation in the CRDS cell due to the low volatility of *n*-decane and its many reaction products.

Table 2: Low-temperature oxidation fuel studies using cw-CRDS. τ: residence time, fuel (%): initial fuel mole fraction, φ: equivalence ratio.

Fuel	detected species	T (K)	P (kPa)	τ (s)	fuel (%)	φ	reference
methane	CH_4, H_2O, CH_2O	500-1300	106.7	1	6.3	2	[220]
dimethylether	H_2O, CH_2O, H_2O_2	500-1100	106.7	2	2	0.25, 1, 2	[120]
	H_2O, CH_2O, H_2O_2, HOȮ	540-850	101.3	1.5	2	0.5, 1, 2	[226]
n-butane	C_2H_4, H_2O, CH_2O, H_2O_2	550-925	106.7	6	2.3	1	[224,225]
	C_2H_4, H_2O, CH_2O, H_2O_2, HOȮ	600-900	101.3	6	2.3	1	[221]
n-pentane	C_2H_4, H_2O, CH_2O, H_2O_2	500-1100	106.7	2	1	0.5, 1, 2	[171]
n-heptane	C_2H_4, H_2O, CH_2O, H_2O_2	500-1100	106.7	2	0.5	1	[184]
1-hexene	C_2H_4, H_2O, CH_2O, H_2O_2	500-1100	106.7	2	1	0.5, 1, 2	[119]
n-hexanal	H_2O, CH_2O, H_2O_2	475-1100	106.7	2	0.5	0.25, 1, 2	[122]
n-decane	C_2H_4, H_2O, CH_2O	500-1100	106.7	2	0.25	1	[184]

The uncertainties of mole fraction depend mainly on the uncertainties of the cross-sections used for quantification. For species like hydrogen peroxide, the relative uncertainties of the cross sections are ~20% [119]. Another source of uncertainty is the definition of the baseline; it is not always possible to consider the maximum ring-down time as the base line. For systems presenting a complex absorption spectrum (e.g., *n*-butane oxidation), peaks are very close, and the ring-down time does not go back to the baseline. This challenge can result in a relative uncertainty of 5% in the absorption coefficient in some unfavorable cases. To minimize uncertainty, the ring-down times at both sides of the peak were usually chosen and an average value used. Overall, relative uncertainties in the mole fractions of the closed shell species in Table 2 quantified by cw-CRDS are usually ~30%.

Note that some molecules (large alkanes) present a continuous absorption over the entire range of wavelengths investigated. This absorption causes a shift of the baseline, depending on the

concentration of the molecule. This shift is especially notable when the molecule is the initial reactant; the shift does not affect the uncertainties, but it reduces the sensitivity.

3.2 Main experimental results of hydroperoxide analysis

3.2.1 Hydrogen peroxide

As is shown in Fig. 1, the preferred way to produce hydrogen peroxide is by disproportionation of two HOȮ radicals, and the dominant way to consume hydrogen peroxide is by decomposition into two ȮH radicals. As a branching reaction, H_2O_2 dissociation is of particular importance for triggering the start of second stage engine autoignition [227]. Hydrogen peroxide concentrations were also measured in studies of burner stabilized cool flames; these were first performed by Carlier et al. [228] using electronic paramagnetic resonance spectroscopy in an *n*-butane cool flame. Because a recent review focuses on cool flame studies [229], this subject will not be detailed here.

Due to its high reactivity, detection of hydrogen peroxide is not obvious; its mole fractions were rarely reported in the literature, even if its formation in gas phase oxidation is proven very early [136]. Analytical methods with direct sampling strategies (sonic probe, molecular beam) are required to obtain reliable data for this species. The following sections describe significant results related to quantification of hydrogen peroxide under reactor conditions.

This discussion is divided into two parts: (1) data recorded in hydrocarbon oxidation studies, and (2) data obtained during oxidation studies of biofuel components. There is an increasing interest in molecules found in biofuels as they can substitute --at least partially-- conventional fuels from crude oil [230-233]. Among the fuels obtained from biomass, ethers are promising candidates. The oxidation of dimethylether (DME, CH_3OCH_3), the simplest ether has been studied extensively, as reviewed in Ref. [120]. Hydrogen peroxide was detected in several independent studies of DME oxidation using molecular-beam mass spectrometry (both EI and PI) [157, 173, 234] and cw-CRDS [120, 226]. Table 3 summarizes the experimental measurement of hydrogen peroxide during gas phase oxidation of fuels.

Hydrocarbons: Hydrogen peroxide was first detected in a low-temperature JSR oxidation study of *n*-butane by SVUV-PIMS [154, 235]. At that time, no data was available for the cross-section of hydrogen peroxide, and an estimated value of 8.58 Mb at 11 eV was used for quantification. This estimation was based on the correlation proposed by Koizumi [239]. Predictions from a model developed by the authors [235] over-estimated the experimental data by a factor of ~ 50. Recently, Dodson et al. [198] measured the cross-section of hydrogen peroxide from the ionization threshold up to 12 eV; they obtained a cross-section of 1.213 Mb at 11.008 eV, which was about seven times lower than the previous estimated value. Thus, using the measured cross-section, model prediction is approaching the experimental value. Additional *n*-butane oxidation experiments were performed later at CNRS-Nancy using cw-CRDS over a wider temperature range (covering both low and high temperature chemistry [224, 225]).

Table 3: Hydrogen peroxide measured during fuel thermal oxidation in JSR and FT. Only studies reporting hydrogen peroxide mole fractions, or signals as a function of temperature, are listed.

fuel	T (K)	P (kPa)	τ (s)	fuel (%)	φ	diagnostic	reference
			Hydrocarbons				
	550-925	106.7	6	2.3	1	*cw*-CRDS	[224,225]
n-butane	600-900	101.3	6	2.3	1	*cw*-CRDS	[221]
	550-800	160.7	6	4	1	SVUV-PIMS	[235]
n-pentane	500-1100	106.7	2	1	0.5, 1, 2	*cw*-CRDS	[171]
	500-700	106.7	2	1	1	SVUV-PIMS	[171]
n-heptane	500-1100	106.7	2	0.5	1	*cw*-CRDS	[184]
			Biofuels				
	500-1100	106.7	2	2	0.25, 1, 2	*cw*-CRDS	[120]
DME	540-850	101.3	1.5	2	0.5, 1, 2	*cw*-CRDS	[226]
	460-950	93.4	4	2.5	0.5	SVUV-PIMS	[180]
	490-740	101.3	1.7	2	0.6	EI-MBMS	[173][a]
	400-1150	101.3	0.44-0.19 2.0-0.87	0.5, 0.88	0.2, 1.06	EI-MBMS	[234][a]
DMM	488-869	100	3	2	0.5	SVUV-PIMS	[236]
acetaldehyde	528-946	98.2	2.7	2.34	0.5	SVUV-PIMS	[197]
n-butanal	542-972	93.3	1.38	2	0.8	SVUV-PIMS	[237]
n-hexanal	475-1100	106.7	2	0.5	0.25, 1, 2	*cw*-CRDS	[122]

Note: DME: dimethyl ether, DMM: dimethoxymethane

The ionization energy of hydrogen peroxide is 10.58 eV [238].

[a] measured in FT, others measured in JSR.

Higher dilution than in previous SVUV-PIMS experiment was adopted because *n*-butane presented a continuous absorption in the investigated wavelength range and caused a shift of the ring-down time baseline. Along with hydrogen peroxide, water, formaldehyde and ethylene were detected. Figure 13 shows that the experimental mole fraction profile of hydrogen peroxide exhibits two peaks. As described previously, these two peaks correspond to the two reaction zones induced by NTC behavior.

As shown in Fig. 13, the kinetic model [225] also predicted these two peaks. The agreement between experimental measurement and model prediction was good in the low-temperature zone, but the model over-estimated the mole fractions by a factor of ~ 4 in the high-temperature regime.

In the model, the kinetic parameters for the decomposition of hydrogen peroxide by Baulch et al. [240] were updated to the new values by Troe [241]. As shown in Figs. 1 and 2 in Ref. [225], using the new rate parameters did not improve H_2O_2 prediction above 800 K, but led to better agreement of the overall reactivity. The authors also proposed a consumption reaction of hydrogen peroxide on the wall. After including this reaction, the model prediction agreed better

with the experiment (dotted line in Fig. 13). Additional experiments performed in a JSR with silicium coating (SiliconertTM 2000, provided by SilcoTek) did not show any significant difference (Fig. 9 in Ref. [225]) compared to the original JSR. But, this did not absolutely confirm that wall effects could not occur.

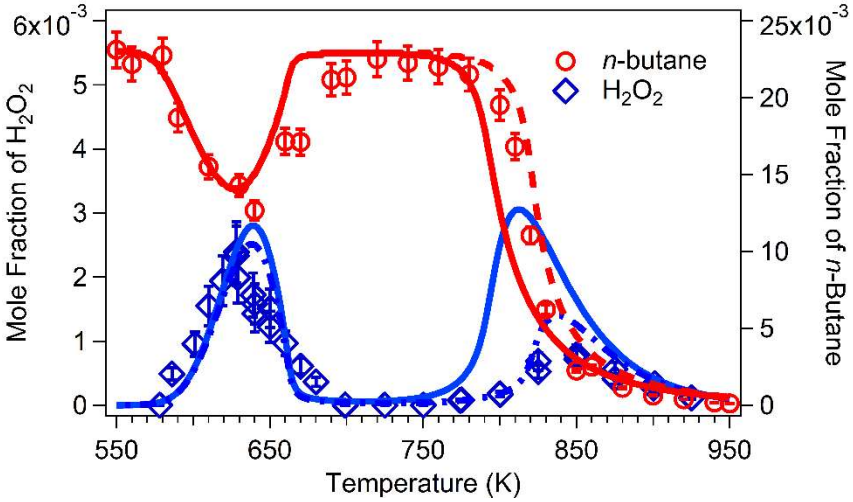

Figure 13: Mole fractions of hydrogen peroxide (measured by cw-CRDS) and *n*-butane (measured by GC) during JSR oxidation of *n*-butane. Full line: original model; dotted line: model with a wall reaction that consumes hydrogen peroxide – adapted from the results of Ref. [225].

Djehiche and coworkers [221] later repeated the *n*-butane oxidation experiment by Bahrini et al. [224] using the cw-CRDS setup built at CNRS-Orléans. The comparison of both datasets showed that the H_2O_2 mole fractions obtained at Orléans were two times larger than those measured in Nancy. Another difference was the temperature that corresponds to the peak mole fraction of hydrogen peroxide in the low-temperature region. It was observed at ~ 630 K in the CRNS-Nancy experiment, but at ~ 670 K in the CNRS-Orléans experiment. There is no obvious explanation for these discrepancies, especially for the shift of the temperature corresponding to the peak mole fraction. Interestingly, the shift was observed for hydrogen peroxide, but not for formaldehyde. New *n*-butane experiments with other diagnostic techniques (e.g. SVUV-PIMS), could provide additional data and help confirm these results.

Hydrogen peroxide was also detected in the oxidation of larger alkanes. Rodriguez et al. [171, 184] quantified this species during the oxidation of *n*-pentane and *n*-heptane using cw-CRDS. In a later JSR oxidation study of *n*-heptane, Wang et al. also observed the formation of hydrogen peroxide [146]. Figure 14 presents the data for hydrogen peroxide at several equivalence ratios during *n*-pentane and *n*-heptane oxidation. The models from Galway satisfactorily predicted the mole fractions of hydrogen peroxide in the low-temperature reaction zone [88, 111]. However, the model significantly overpredicted the mole fraction of hydrogen peroxide in the high-temperature reaction zone. This phenomenon is also observed for *n*-butane oxidation in Fig. 13.

Furthermore, the oxidation of both alkanes was studied in the low-temperature region (500-700 K) using SVUV-PIMS at the National Synchrotron Radiation Laboratory in Hefei [171, 184]. The main difference was that the carrier gas at Nancy was helium, and argon was used in Hefei. Figure

14 also displays the mole fraction profiles of H_2O_2 obtained by SVUV-PIMS in *n*-pentane and *n*-heptane oxidation. Note that in both cases, the authors extrapolated the cross-sections of H_2O_2 from the data by Dodson et al. [198] to calculate the mole fractions of hydrogen peroxide measured at 13.05 eV. Despite this approximation, excellent agreement of the two datasets by cw-CRDS and SVUV-PIMS was observed. Moreover, no temperature shift was observed between the two mole fraction profiles, which were obtained by different JSRs and sampling methods in the two experiments [171, 184].

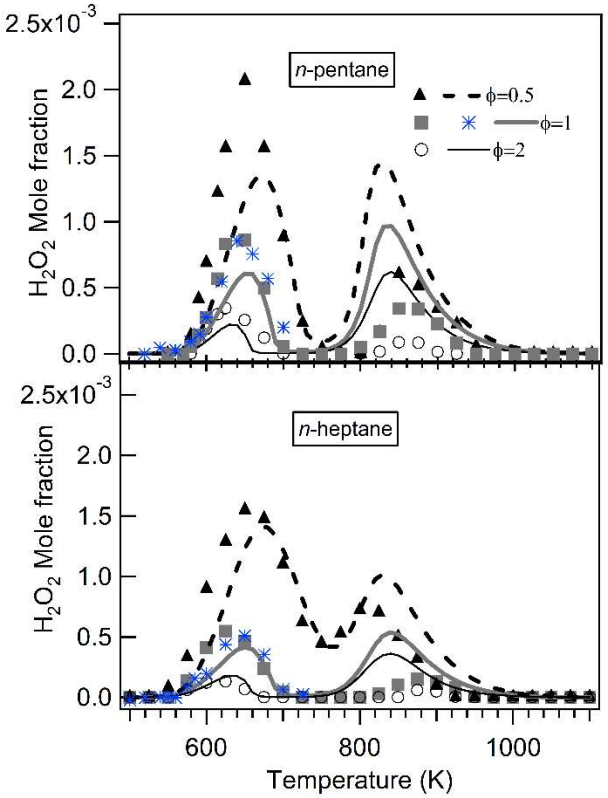

Figure 14: Experimental (symbols) and simulated (lines) mole fraction profiles of H_2O_2 during JSR oxidation of *n*-pentane ($x°_{fuel}$ = 0.01) and *n*-heptane ($x°_{fuel}$ = 0.005). Grey and black symbols are cw-CRDS measurements; blue crosses are SVUV-PIMS data - adapted from the results of Refs. [171, 184].

Meng et al. [119] revisited the low-temperature oxidation of 1-alkenes, which has considerable chemical specificity due to the presence of the double bond. They performed 1-hexene oxidation experiments in a JSR and measured hydrogen peroxide mole fractions by cw-CRDS. Because of the NTC behavior and similar to alkanes (discussion in Section 3.1.1), two peaks in mole fraction profile of hydrogen peroxide were observed in different temperature regions. The model prediction of hydrogen peroxides from Meng et al. [119] was not good in both the low- and high-temperature reaction zone, except for the low-temperature prediction under stoichiometric condition.

Biofuels: Hydrogen peroxide was first quantified in biofuel system in the oxidation of linear ethers. Guo et al. [173] reported the first direct measurement of hydrogen peroxide during the oxidation of DME. The quantification of H_2O_2 was carried out using a direct calibration of H_2O_2; the

experiment was performed in a flow reactor in the low-temperature region of 490-750 K. A molecular beam was used for direct sampling and EI-MS for detection. Results showed DME to be a somewhat reactive molecule, which begins to react at ~ 550 K. A significant production of hydrogen peroxide was also reported, and an early peak mole fraction at 600 K (Fig. 4 in Ref. [173]). Model predictions in the literature for hydrogen peroxide were satisfactory, but fuel conversion was significantly over-estimated at around 600 K (Fig. 3b in Ref. [173]). Later, Kurimoto et al. [234] extended the operating conditions of these experiments and refined the kinetic model.

Rodriguez et al. [120] also detected hydrogen peroxide during the JSR oxidation of DME over a wider temperature range (500-1100 K), using cw-CRDS. As indicated by the selectivity diagram in Fig. 15(a), hydrogen peroxide was among the main reaction products of DME oxidation at 625 K. This temperature corresponds to the peak mole fraction of H_2O_2 in the low-temperature reaction zone (Fig. 15(b)). These observations are consistent with those of Guo et al. [173]. Figure 15(b) shows that predictions using a model updated by the authors under-estimated the mole fractions of hydrogen peroxide across the studied temperature range, and especially under stoichiometric and fuel-lean conditions. The underestimation of H_2O_2 mole fraction by the model in the high-temperature region was in contrast to the observation of C_4-C_7 alkanes [171, 184, 225], 1-hexene [119], and another DME study by Moshammer et al. [180], in which the models over predicted the H_2O_2 mole fraction.

Le Tan et al. [226] also studied the JSR oxidation of DME, conducting experiments over a temperature range of 540-840 K and using cw-CRDS to detect HOȮ radical and hydrogen peroxide. The cw-CRDS also measured H_2O and CH_2O. Models in the literature were used to predict the temperature-dependent mole fractions of these four intermediates. DME reactivity predicted by the models could not be evaluated because the DME mole fraction was not measured; however, the measured temperature dependence and mole fraction of the H_2O_2 was satisfactorily predicted by model in the literature [242].

The formation of hydrogen peroxide was also reported by Moshammer et al. [180] during the JSR oxidation of DME (470-990 K) using SVUV-PIMS. The photoionization cross-section used was from Dodson et al. [198]. Similar to the work of Rodriguez et al. [120], the experimental temperature dependence of hydrogen peroxide mole fraction displayed two maxima: one at around 600 K and another at around 800 K. Literature models [120, 242, 243] predicted this dependence well, but the computed values of the H_2O_2 mole fraction were larger than the experimental measurements by a factor from about two to at least five, across the studied temperature range. Interestingly, Moshammer et al. showed that three different up-to-date models predicted largely different H_2O_2 concentrations in the high-temperature range, clearly revealing the need for further improvement of detailed chemical mechanisms.

The temperature dependence of the mole fraction of hydrogen peroxide has also been observed by Sun et al. [236] during the JSR oxidation of dimethoxymethane (DMM, $CH_3OCH_2OCH_3$), using SVUV-PIMS. The JSR was operated at temperatures from 488 to 869 K and pressure close to one atmosphere, with a mixture at φ = 0.5 and with 2% of fuel. The hydrogen peroxide mole fraction was evaluated using the cross-section published by Dodson et al. [198]. For this reaction system,

the models proposed by the authors, by Vermeire et al. [244], and by Marrodán et al. [245] acceptably predicted the hydrogen peroxide mole fraction.

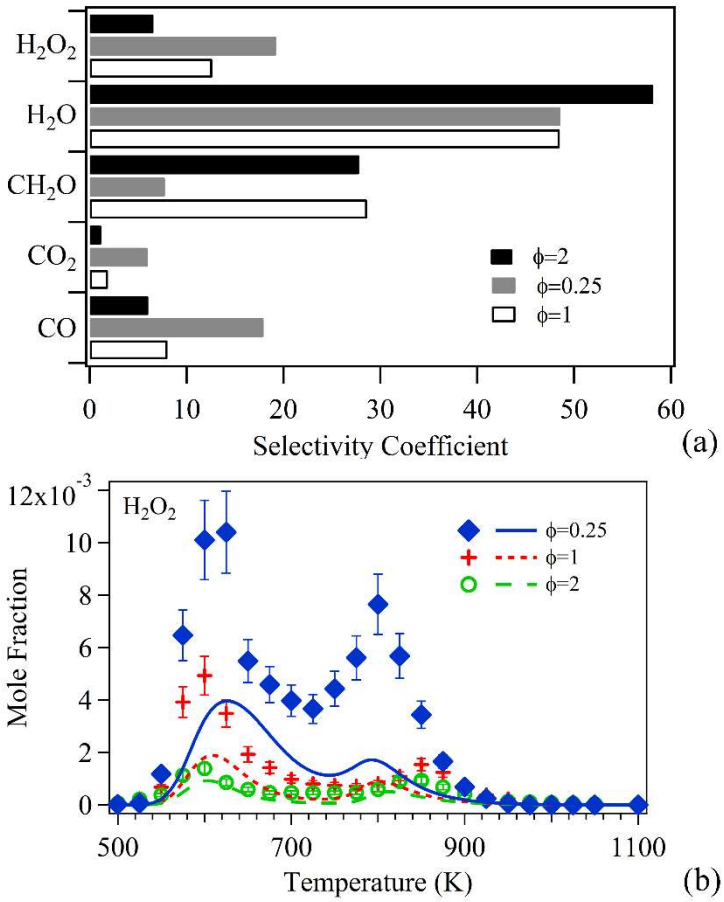

Figure 15: (a) Experimental selectivity of main reaction products at 625 K, and (b) mole fraction of hydrogen peroxide detected in the oxidation of DME (experiments are symbols with error bars, lines are simulations) – adapted from the results of Ref. [120].

In addition to the ether biofuels, aldehydes are another class of oxygenated compounds that have reported the formation of H_2O_2. Tao et al. [197] studied the oxidation of acetaldehyde in a JSR using SVUV-PIMS after molecular-beam sampling. Although acetaldehydes are not currently considered to be biofuels, they are important intermediates formed in alkanes oxidation [92] and in the oxidation of oxygenated molecules like alcohols [121]. Figure 16 shows the temperature dependence of the H_2O_2 mole fractions in acetaldehyde oxidation. In this data evaluation, the authors also adopted H_2O_2 cross-sections measured by Dodson et al. [198]. The authors developed a model for acetaldehyde oxidation based on the AramcoMech 2.0 mechanism [118]. This model reproduces well the high reactivity of acetaldehyde, but overpredicts the maximum H_2O_2 mole fraction by a factor of ~ 6.

In the JSR oxidation study of *n*-butanal, the mole fraction profile of H_2O_2 was also measured by SVUV-PIMS [237]. The result indicated a maximum mole fraction of 1.3×10^{-3} at 670 K using the cross-sections measured by Dodson et al. [198]. However, a comparison with the model prediction was not shown.

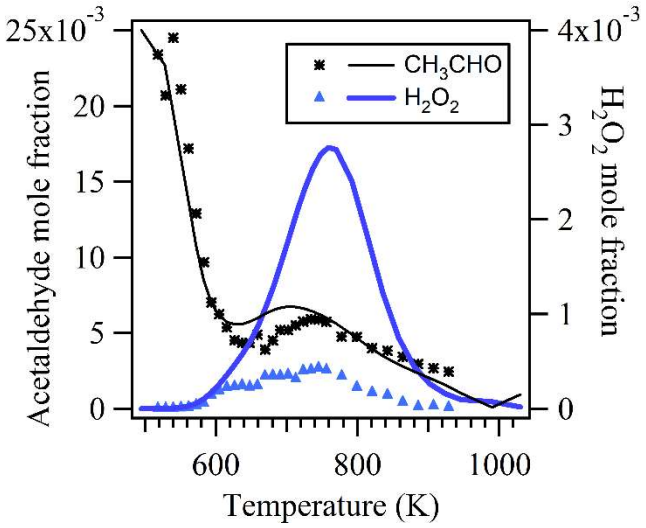

Figure 16: Experimental (symbols) and simulated (lines) mole fraction profiles of H_2O_2 and acetaldehyde during the JSR oxidation of acetaldehyde ($x°_{fuel}$ = 0.025, φ = 0.5) at a pressure of 93.3 kPa and a residence time of 2.7s - Plotted from the data in Supplementary Material of Ref. [197].

Rodriguez et al. [122] investigated the oxidation of *n*-hexanal in a JSR by GC and cw-CRDS. Using cw-CRDS, a large amount of hydrogen peroxide was measured during the oxidation of this very reactive fuel. Its maximum mole fraction, 8.6×10^{-4} at 650 K and φ = 0.5, is in the same order of magnitude as those of typical low-temperature reaction products, such as formaldehyde or acetaldehyde. Generally, the model developed by the authors satisfactorily predicted the maxima of H_2O_2 mole fractions, except under fuel-rich conditions.

In summary, the cw-CRDS technique has proven to be a powerful tool to measure mole fractions of hydrogen peroxide during the oxidation of fuels. It is expected that larger hydroperoxides (e.g. methyl hydroperoxide (CH_3OOH)), could be detected in other spectral regions. Application of this technique for *n*-heptane and *n*-hexanal oxidation was successful; However, some limitation for even larger molecules such as *n*-decane was observed, due to the condensation in the CRDS cell. It is possible that molecular beam sampling, coupled to a CRDS cell, could solve this problem.

The SVUV-PIMS technique also provided reliable data for H_2O_2, especially after the experimental measurement of the absolute photonionization cross-sections of H_2O_2 [198]. Two studies showed H_2O_2 data, measured by cw-CRDS and SVUV-PIMS, to be in good agreement [171, 184]. Thus, both methods are suitable for measuring H_2O_2, and the accuracy of the results depends largely on the photoabsorption and photoionization cross-sections, respectively. Given the fact that the photoionization experiments described here were largely performed at synchrotron facilities, it seems that the cw-CRDS technique is easier to implement.

In most cases, the up-to-date mechanisms were challenged to accurately predict the mole fraction of H_2O_2, especially in the high-temperature reaction zone. This is somewhat unexpected since the combustion mechanism of the H_2/O_2 system is well known [246]. However, given the fact that the HOȮ radical is the main source for H_2O_2, the chemistry of HOȮ or the fuel-specific reactions to HOȮ should be investigated further, since uncertainties in the kinetic parameters for the

decomposition of hydrogen peroxide are not expected to explain the observed deviations. From the experimental viewpoint, the influence of the wall effect could not be excluded either, as mentioned in Refs. [225, 234]. Decomposition of hydrogen peroxide at the walls of the reactor or of the CRDS probe may affect the measurement of H_2O_2 [225].

In parallel to the measurement of H_2O_2, experimental efforts were conducted to establish measurement routines to quantitatively detect HOȮ radicals. While considerable work has been published regarding radical analysis in flames [186, 215], few attempts were made to measure radicals during fuel low-temperature oxidation without a combined photolysis initiation. ȮH and HOȮ radicals were detected in *n*-butane JSR oxidation using fluorescence assay by gas expansion technique (FAGE), but the quantification included substantial uncertainties [247]. HOȮ radicals were later measured during *n*-butane JSR oxidation using cw-CRDS [221] under the same conditions as Ref. [247]. The shapes of the temperature dependence of HOȮ radicals measured by FAGE and cw-CRDS were comparable, except for the high-temperature reaction zone: the FAGE HOȮ mole fractions peaked at ~ 900 K, whereas the cw-CRDS HOȮ mole fractions peaked at ~ 830 K. The maximum mole fraction of HOȮ radicals at 650 K differed by a factor of three in the two studies. Very good agreement was observed over the range of 780-830 K. HOȮ radicals were also quantified during DME oxidation in a JSR and a FT by cw-CRDS [226] and by mid-infrared Faraday rotation spectroscopy [234, 248], respectively.

3.2.2 Alkyl hydroperoxides

In this section, recent studies on alkyl hydroperoxides will be summarized. Because their formation pathways are distinct, two kinds of alkyl hydroperoxides were distinguished: alkyl hydroperoxides with less carbon atoms than in the fuel reactant, and alkyl hydroperoxides with the same carbon skeleton as the fuel molecule (e.g., ROOH in Fig. 1). Dominant consumption of the two types of organic hydroperoxides occur from the dissociation of the O-OH bond, which leads to an alkoxy radical and an ȮH radical. Table 4 summarizes gas phase oxidation studies in which attempts to quantify alkyl hydroperoxides have been made. To the best of our knowledge, these attempts were only performed in JSR oxidation studies.

As shown in Fig. 1, an alkyl hydroperoxide is produced mainly from the reaction of an HOȮ radical with an alkyl peroxy radical. In an alkyl hydroperoxide with less carbon atoms than the reactant, the peroxy radical is produced from the O_2 addition to the alkyl radicals. These alkyl radicals could be produced by β-C-C scission reactions of the fuel radicals (Ṙ) or ketoalkoxyl radicals [146].

In 2010, during the JSR oxidation of *n*-butane, Battin-Leclerc et al. [123] measured the temperature dependence of signals at m/z 48 and 62 and identified them as methyl and ethyl hydroperoxides by SVUV-PIMS. In a paper that followed [235], the mole fractions for these compounds were estimated; the cross-sections for CH_3OOH and C_2H_5OOH (i.e., 8.9 Mb and 8.6 Mb respectively at 10 eV), were based on the correlation proposed by Koizumi [239]. In these studies, the mole fraction of butenes measured by GC was used as reference. Large discrepancies, with a factor of 200 for methyl hydroperoxide and a factor of 20 for ethyl hydroperoxide, were observed when comparing the experimental mole fraction profiles to the predictions by a model in the literature [253]. The very large discrepancies can be attributed to uncertainties in the estimated

cross-sections, for example the estimated cross-section value for CH_3OOH is a factor of 50 higher than the calculation of Moshammer et al. [180]. However, the uncertainties of the kinetic model cannot be ruled out since the model was developed using old kinetic data and rate rules [253].

Table 4: Alkyl hydroperoxides measured during fuel thermal oxidation in JSR. Only studies reporting alkyl hydroperoxide mole fractions, or signals as a function of temperature, are listed.

hydroperoxides	fuel	T (K)	P (kPa)	τ (s)	fuel (%)	φ	diagnostics	reference
Alkyl hydroperoxides with a lower carbon number than the reactant								
C_1 HP	DME	460-950	93.4	4	2.5	0.5	SVUV-PIMS	[180]
C_1 HP	Acetaldehyde	400-900	101		2	0.5, 1, 4	SVUV-PIMS	[250]
C_1 HP	Acetaldehyde	528-946	98.2	2.7	2.34	0.5	SVUV-PIMS	[197]
C_1 HP	DMM	488-869	100	3	2	0.5	SVUV-PIMS	[236]
C_1 – C_2 HP	propanal	450-800	101.3	2	2	0.35, 4	SVUV-PIMS	[251]
C_1 – C_2 HP	*n*-butane	550-800	106.7	6	4	1	SVUV-PIMS	[154,235]
C_1 – C_3 HP	*n*-butanal	542-972	93.3	1.38	2	0.8	SVUV-PIMS	[237]
C_1 – C_2 HP	*n*-pentane	500-800	106.7	2	1	0.5, 1, 2	SVUV-PIMS [a] SPI-MS	[171]
C_1 – C_3 HP	1-hexene	500-1000	106.7	2	1	0.5, 1, 2	SPI-MS	[119]
C_1 – C_3 HP	*n*-heptane	500-850	106.7	2	0.5	0.25, 1, 2, 4	SPI-MS	[184]
C_1 – C_3 HP	*n*-decane	500-850	106.7	2	0.25	1	SPI-MS	[184]
Alkyl hydroperoxides of the same size as the reactant								
C_3 HP	propane	530-730	106.7	6	12	1	SVUV-PIMS	[108]
C_4 HP	*n*-butane	550-800	106.7	6	4	1	SVUV-PIMS	[154]
C_5 HP	*n*-pentane	500-800	106.7	2	1	1	SVUV-PIMS SPI-MS	[171]
Olefinic hydroperoxides								
C_3 – C_5 OHP	*n*-pentane	500-900	106.7	2	1	0.5, 1, 2	SVUV-PIMS	[171]
C_3, C_6 OHP	1-hexene	500-1000	106.7	2	1	0.5, 1, 2	SVUV-PIMS SPI-MS	[119,252]
C_3 – C_7 OHP	*n*-heptane	500-850	106.7	2	0.5	0.5, 1, 2, 4	SVUV-PIMS SPI-MS	[184]
C_7 OHP [b]	*n*-heptane	500-600	104	2	1	1	SVUV-PIMS	[146]
C_7 OHP [b]	2MHX	530-740	104	0.5	2	1	SVUV-PIMS	[253]
C_3 – C_6 OHP	*n*-decane	500-850	106.7	2	0.25	1	SVUV-PIMS SPI-MS	[184]
C_9 – C_{10} OHP [b]	*n*-decane	500-850	106.7	2	0.25	1	SVUV-PIMS SPI-MS	[184]

Note: Hydroperoxide and olefinic hydroperoxide are abbreviated as HP and OHP, respectively.

DME: dimethyl ether, DMM: dimethoxymethane, 2MHX: 2-methylhexane.

The ionization energy of methyl hydroperoxide, ethyl hydroperoxide, propyl hydroperoxides, butyl hydroperoxides, pentyl hydroperoxides is ~ 9.9, ~ 9.7, ~ 9.5, ~ 9.4, ~ 9.2-9.5 eV, respectively [108, 123]. The ionization energy of allyl hydroperoxide, butenyl hydroperoxides, pentenyl hydroperoxides, hexenyl hydroperoxides, and heptenyl hydroperoxides is ~ 9.6, ~ 9.3, ~ 9-9.3, ~ 8.8-9.3, ~ 8.8-9.2 eV, respectively [171, 184, 251].

[a] only C1 HP was measured.

[b] only signals were reported, not mole fractions.

In subsequent papers for the JSR oxidation of hydrocarbons (e.g., propane [108], isomers of hexane [254], 1-hexene [251], *n*-heptane [255]) using SVUV-PIMS in Hefei, the authors did not mention the formation of C_1-C_2 alkyl hydroperoxides; this was because signal intensities were low and did not attract attention at that time.

In later work, the Nancy team studied the JSR oxidation of alkanes using SPI-MS. In the *n*-pentane oxidation studied by Rodriguez et al. [171], the mass spectrum in Fig. 17 clearly showed mass peaks at m/z = 48 and 62. Other m/z will be discussed further in the text. This observation led to revisiting older data obtained in Hefei and reanalyzing the PIE curve for both m/z = 48 and 62. In

comparisons to theoretical calculations, the ionization onset confirmed that these two peaks can be attributed to methyl and ethyl hydroperoxides, respectively.

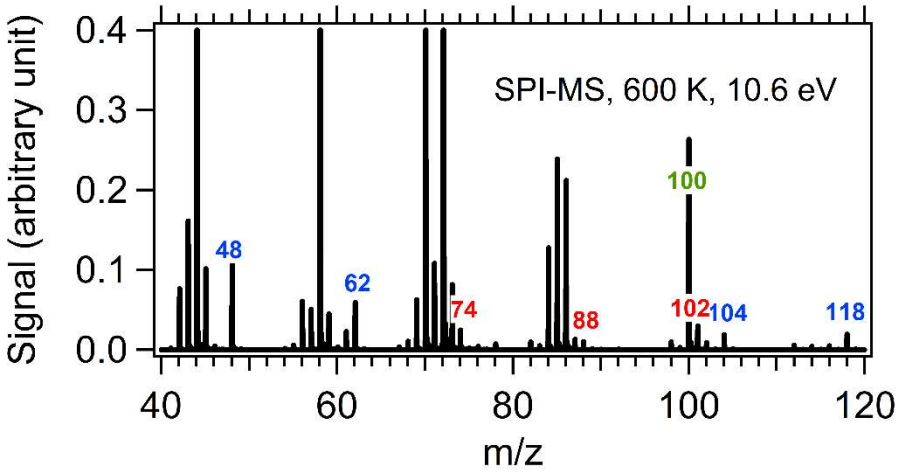

Figure 17: Mass spectrum obtained by SPI-MS during *n*-pentane JSR oxidation at 600 K – adapted from the results of Ref. [171].

Rodriguez et al. [184] also re-examined the JSR oxidation of *n*-heptane by SPI-MS. The PIE curve obtained by Herbinet et al. [255] confirmed the species identification. In addition to methyl and ethyl hydroperoxides, isomers of propyl hydroperoxide were also detected for this C_7 alkane. These species were also observed during a recent study by Wang et al. [146] on *n*-heptane JSR oxidation using SVUV-PIMS and APCI-OTMS. Rodriguez et al. [171, 184] furthermore estimated the mole fractions of these C_1-C_3 hydroperoxides with cross-sections calculated using the group additivity method proposed by Bobeldijk et al. [199]. Due to significant fragmentation during ionization of KHPs, this group additivity method is not entirely reliable for estimating the cross sections for KHPs (see Section 3.2.4); however, it gives satisfactory estimations for some alkyl hydroperoxides, as shown hereafter. The estimated cross-sections for the C_1-C_3 hydroperoxides at 10.6 eV are 4.4 Mb, 5.1 Mb, and 5.8 Mb, respectively. The contribution of each group was estimated from the analysis of standard species. This estimation did not consider the O-OH group because no standard was available. In the mole fraction evaluation, the mole fraction of propene measured by GC was used as a reference. Figure 18 presents the experimental mole fractions of these three hydroperoxides using SPI-MS. Predictions by the recent Galway *n*-heptane model [88] are also shown. The mole fractions of these three hydroperoxides peak experimentally at ~ 600 K and are in the order of methyl hydroperoxide > ethyl hydroperoxide > propyl hydroperoxide; the mole fraction of propyl hydroperoxide is much lower, i.e., below 5 ppm.

For methyl and ethyl hydroperoxides, the model reproduced the shape of the experimental profiles well, as well as the influence of the equivalence ratio from 0.25 to four. The predicted mole fractions were nevertheless a factor of three to five times larger than the experimental measurements; this discrepancy is not significant considering that the estimated cross-sections had significant uncertainties. However, bad prediction of the temperature dependence for propyl hydroperoxides indicates larger kinetic uncertainties for the reactions of C_3 alkyl radicals than those for C_1-C_2 alkyl radicals. It was particularly noted that the model drastically overpredicted

the formation of C_3H_7OOH intermediates at very low temperatures, i.e. according to the model, the C_3 alkyl hydroperoxide formed at lower temperatures than the C_1 and C_2 alkyl hydroperoxides.

It was also noted that the measured equivalence ratio effect on propyl hydroperoxides was slightly different from that of methyl and ethyl hydroperoxides. The reason for this inconsistency is still unclear.

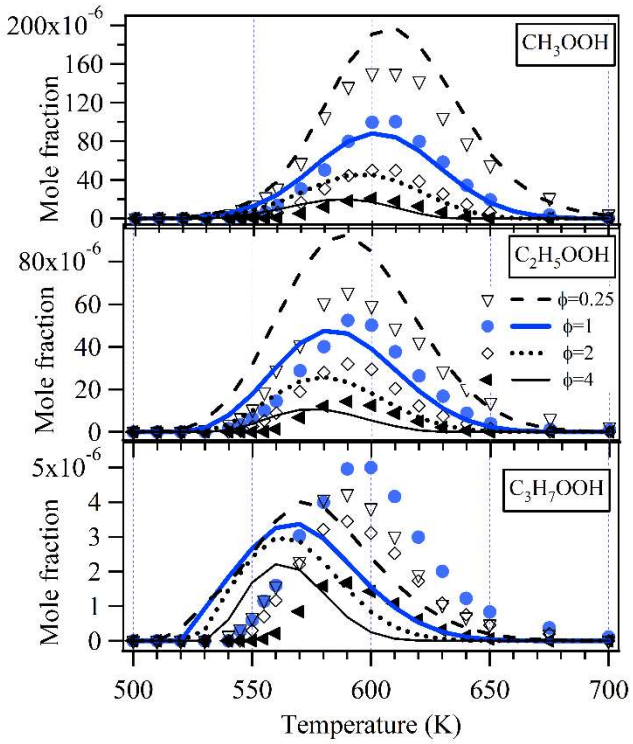

Figure 18: Temperature dependence of mole fraction of C_1 to C_3 alkyl hydroperoxides measured by SPI-MS during *n*-heptane JSR oxidation with four equivalence ratios. Symbols are experiments, lines are simulations. Simulated values divided by a factor of three, five and two, for CH_3OOH, C_2H_5OOH, and C_3H_7OOH (sum of the isomers), respectively – adapted from the results of Ref. [184].

The C_1-C_3 hydroperoxides were also measured in 1-hexene JSR oxidation using SPI-MS [119]; their quantification used the calibration method proposed in Refs. [171, 184]. Predictions using a model developed by the authors agreed with the experimental results within a factor of two for methyl and ethyl hydroperoxides, and a factor of four for propyl hydroperoxides.

Methyl hydroperoxide was also quantified in the JSR oxidation of five oxygenated molecules: dimethylether (DME) [180], dimethoxymethane (DMM) [236], acetaldehyde [197, 249], propanal [250] and *n*-butanal [237]. For the first four oxygenated fuels listed, the CH_3OOH mole fraction profiles peaked at close to 600 K (see Fig. 10 for DME); for *n*-butanal, it peaked closer to 650 K. In all these studies, the cross-section of CH_3OOH employed was the same as was theoretically calculated by Moshammer et al. [180] (Section 3.1.2.2). The calculated cross-section was 7 Mb at 11 eV. This value was very close to the estimation (5 Mb at 11 eV) by Rodriguez et al. [184], who used the group additivity method proposed by Bobeldijk et al. [199]. It is important to note that

with this theoretically calculated cross-section, the experimental mole fractions of CH_3OOH were well predicted by models of DME [120], DMM [236, 244], acetaldehyde [256], and propanal [250]. Knowing that the $CH_3O\dot{O}$ radical chemistry has been studied much less the H_2/O_2 system, it is surprising to see that in some cases the up-to-date models more closely predicted the methyl hydroperoxide mole fractions than that of hydrogen peroxide. In addition to methyl hydroperoxide, ethyl hydroperoxide was also quantified in propanal oxidation [250] and detected in *n*-butanal oxidation [237].

C_{n-1} alkyl radicals have been shown to be important intermediates during the oxidation of C_n aldehydes [256]. In a study of propanal oxidation [250], ethyl hydroperoxide was quantified using the cross-section in Ref. [171], which was based on the group additivity method proposed by Bobeldijk et al. [199]. The cross-section value was 7.6 Mb at 11 eV. The mole fraction profile obtained was well predicted using the model proposed by the authors. The analysis shows that the decomposition of methyl and ethyl hydroperoxides were the dominant source of hydroxyl radicals at 675 K for all equivalence ratios (i.e., ϕ = 0.35, 1.0, and 4.0). Propyl hydroperoxide was quantified during the oxidation of *n*-butanal [237]. With a cross-section estimated to be 5 Mb at 11 eV, the obtained mole fraction profile was well predicted using the model of Pelucchi et al. [257]. It was noted that in the quantification of C_1-C_3 hydroperoxides, these studies used values between 5-8 Mb at 11 eV for the three compounds.

Different from the C_1, C_2, and C_3 hydroperoxides mentioned above, the alkyl hydroperoxides with the same carbon skeleton as the reactant were derived directly from the alkyl peroxy radicals. These radicals were produced from the O_2 addition to the fuel radicals ($\dot{R}$). Because the isomerizations of alkyl peroxy radicals competed directly with the pathways that form this type of alkyl hydroperoxides, their production became less favorable when the isomerization routes were easier. In fact, a long carbon chain of the reactant favors these isomerizations. This may explain the discovery that alkyl hydroperoxides with the same carbon skeleton as the reactant were observed only in C_3-C_5 fuels. However, it should be noted that in a recent study of *n*-heptane oxidation, Wang et al. [146] observed a peak at m/z 132, corresponding to the C_7 alkyl hydroperoxides.

For the pentyl hydroperoxides measured by Rodriguez et al. [171] during *n*-pentane JSR oxidation (see m/z = 104 in Fig. 17), mole fractions were derived from the cross-section (i.e., 15.1 Mb at 11 eV) evaluated using the group additivity method proposed by Bobeldijk et al. [199]. Good agreement was observed between predictions from the recent Galway pentane model [111] and the experimental mole fractions. In summary, it appears that for the C_1-C_3 hydroperoxides and pentyl hydroperoxides, the mole fractions obtained from cross-section by calculation and group additivity method are consistent with predictions from the up-to-date kinetic models.

3.2.3 Olefinic hydroperoxides

Olefinic hydroperoxides can be produced by combination of an alkenyl radical with an $HO\dot{O}$ radical, and the bimolecular reaction of $HO\dot{O}$ with $RO\dot{O}$, which is produced from the O_2 addition to the alkenyl radical [251]. Alkenyl radicals are mainly produced by H-abstractions from alkenes. Due to the presence of the double bond, resonance-stabilized radicals may be formed; these --as

well as HOȮ radicals-- are the predominant radicals observed before engine autoignition of olefins. For alkane fuels, olefinic hydroperoxides can also be produced from hydroperoxyalkyl radicals (ȮOOH in Fig. 1) by β-scission reactions, or abstraction reactions by O_2. In the case of olefinic hydroperoxides with the same carbon skeleton as the alkane reactant, another pathway should be considered: the elimination of HOȮ radical from hydroperoxyalkylperoxy radicals (ȮOQOOH in Fig. 1) and/or dihydroperoxyalkyl radicals. Dihydroperoxyalkyl radicals can be obtained from ȮOQOOH radicals by internal isomerizations [100]. Further explanation about these unconventional pathways are given in Section 3.2.5.

Table 4 summarizes gas phase oxidation studies, in which olefinic hydroperoxides have been quantified, or their signals with temperature have been measured. Battin-Leclerc et al. [251] reported an olefinic hydroperoxide in their JSR oxidation study of 1-hexene. The SVUV-PIMS in Hefei detected a signal at m/z = 116. Experimentally measured ionization energy is consistent with the values from theoretical calculations (~ 9.25 eV) for hexenyl hydroperoxides. This m/z at 116 was also detected by Meng et al. [119] in their JSR oxidation study of 1-hexene using SPI-MS. The m/z = 74 that corresponds to C3H5OOH was also measured.

Rodriguez et al. [171, 184] also detected olefinic hydroperoxides by SPI-MS in their JSR oxidation studies of alkanes. The identification of these peroxides was achieved via PIE curves obtained by SVUV-PIMS. For example, the signal at m/z = 74, 88, and 102 in Fig. 17 for *n*-pentane oxidation, corresponds to isomers of allyl hydroperoxide, butenyl hydroperoxides, and pentenyl hydroperoxides, respectively. During the JSR oxidation of three alkanes (*n*-pentane, *n*-heptane, and *n*-decane), olefinic hydroperoxides with C_3 up to C_x carbon chain were detected, with x being the number of carbon atoms of the reactant. However, the heptenyl and octenyl hydroperoxides were not measured during *n*-decane oxidation. In a recent work on *n*-heptane oxidation, Wang et al. [146] also detected the olefinic hydroperoxides from C_3 to C_7.

The m/z ratio corresponding to olefinic hydroperoxides with the same carbon skeleton as the reactant was detected by SVUV-PIMS during the JSR oxidation of a wide range of linear, branched and cyclic C_7-C_{12} alkanes, and biofuel components [146, 172, 252, 258]. Examples of recorded mass spectra are given in Fig. 19. This figure shows that hydroperoxides which include a C=C bond while keeping the same structure as the reactant, are not only formed in alkanes oxidation (panels (A) to (J)), but are also produced when oxygenated fuels with long carbon chains are used as reactants (panels (K) to (O)).

In a time-resolved SVUV-PIMS study of the tetrahydrofuran oxidation initiated by photolysis in a FT at 1.3 kPa, Antonov et al. [259] reported a signal at m/z = 102, which they attributed to 2,3-dihydrofuranyl hydroperoxide. This intermediate was identified from a comparison between experimental and theoretically calculated ionization energies (~8.57 eV).

The temperature dependence of the signal of an olefinic hydroperoxide was plotted during the JSR oxidation study of 2-methylhexane (see Fig. 3b of Ref. [252]). However, due to the lack of photoionization cross-sections, this intermediate was not quantified.

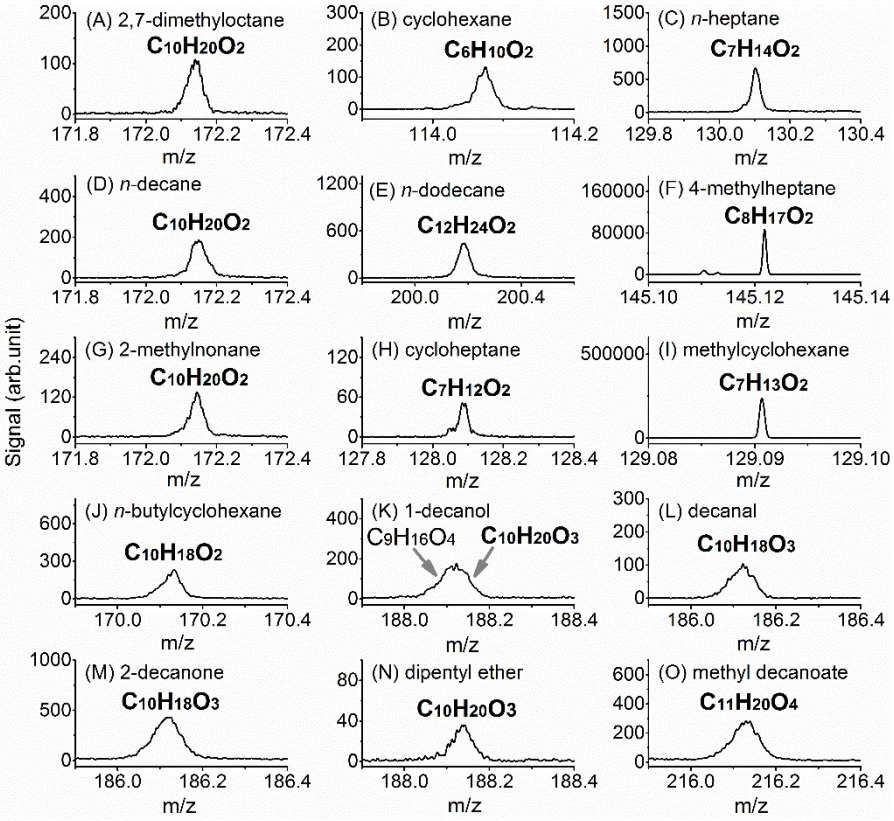

Figure 19: Mass spectrum of olefinic hydroperoxides with identical carbon skeleton of organic reactants. Data recorded by SVUV-PIMS, except for panels (F) and (I), obtained by APCIOTMS. (T = (A) 520, (B) 540, (C) 540, (D) 530, (E) 500, (F) 520, (G) 530, (H) 580, (I) 535, (J) 540, (K) 580, (L) 520, (M) 550, (N) 510, (O) 530 K). Reproduced from Ref. [172] with permission of PNAS.

In Refs. [119, 171, 184] for *n*-pentane, *n*-heptane, *n*-decane, and 1-hexene oxidation, the temperature profiles of all the detected olefinic hydroperoxides were systematically plotted. Tentative quantifications of these peroxides were performed based on cross-sections evaluated using the group additivity method proposed by Bobeldijk et al. [199]. Models of *n*-pentane [111], *n*-heptane [88], *n*-decane [184] and 1-hexene [119] in the literature were adopted to predict the mole fraction of these olefinic hydroperoxides. In contrast to the prediction of alkyl hydroperoxides by these models, significantly larger deviations between experiments and simulations were observed for the olefinic hydroperoxides. Among the olefinic hydroperoxides, the deviations were generally the smallest for C_3 species; the largest deviations were observed when the corresponding combination reaction of an alkenyl radical with an HOȮ radical was not included in the model.

In summary, with recent progress in mass spectrometry methods, a wide range of alkyl hydroperoxides and olefinic hydroperoxides has been detected during gas phase oxidation of numerous C_2-C_{12} alkanes, alkenes and oxygenated molecules. Due to the difficulty in acquiring photoionization cross-sections of these species, quantification studies are scarce and often prone to significant uncertainty. However, in the case of CH_3OOH, the cross-sections could be theoretically calculated, and a reliable quantification was achieved. The up-to-date models also satisfactorily predicted the mole fraction of CH_3OOH, indicating satisfactory understanding of the oxidation kinetics of this small peroxide. In larger alkyl hydroperoxides, as well as olefinic

hydroperoxides, large discrepancies between experimental and modeling results were generally observed. Both the accuracy of the photoionization cross-sections and the reaction kinetics of these species must be improved, e.g., synthesizing the peroxides and measuring their photoionization cross-sections, improving the method of photoionization cross-sections calculation, and exploring the key reaction pathways and calculating the rate coefficients.

3.2.4 Ketohydroperoxides

KHPs have been included in the kinetic models ever since the pioneering work of Sahetchian et al. [147], and the seminal paper of Curran et al. [98]. Only recently, however, Battin-Leclerc et al. [123] discovered strong experimental evidence for the presence of KHPs. The authors coupled a JSR with molecular-beam sampling and mass-spectrometric detection using single-photon ionization via synchrotron radiation. In a series of papers [123, 154, 235], the groups of Battin-Leclerc and Qi reported the detection, identification and tentative quantification of the KHP in low-temperature oxidation of *n*-butane. Since the detection of the KHPs was reported for *n*-butane, experimental evidence for KHPs in the low-temperature oxidation of many other hydrocarbons and oxygenated fuels has been published (e.g., Ref. [172, 251, 252, 260]). Chemical ionization and laser-based photoionization techniques have also made it possible to detect KHP in non synchrotron-based experiments, e.g. Ref. [146, 171]. Table 5 lists studies that have measured the temperature dependence of mole fractions, or signals of KHP.

Whereas Table 5 indicates that KHPs were detected when DME, propanal, *n*-butanal, 1,2-dimethoxyethane ($CH_3OC_2H_4OCH_3$) and C_{4+} alkanes were used as fuel, KHPs were not observed when propane oxidation was studied using SVUV-PIMS [108], even though propyl hydroperoxide was observed (Table 4). Note that the JSR oxidation of *n*-butanal [237] detected a KHP, $C_3H_6O_3$, corresponding to the KHP expected from propyl radical oxidation. This KHP is an important intermediate during the oxidation of *n*-butanal.

For a long time, the high reactivity of these multi-functional intermediates hampered their detection; as described in Section 3.1.2, molecular-beam sampling and soft ionization mass spectrometric techniques made their direct measurement possible. The main approach to the identification of KHPs is the exact m/z ratio in the high-resolution mass-spectrometric detection (e.g., TOF), which provides information about their chemical composition. Furthermore, observed ionization energy and fragmentation patterns have proved to be very helpful and should be considered when identifying KHPs. While this approach worked for DME [180] and *neo*-pentane [260], in which only one KHP isomer is conceivable, more work is needed for the identification and separation of different isomeric structures when molecular structure of the fuel becomes more complex.

In their *neo*-pentane work [260], Eskola et al. measured time-dependent signal profiles of KHP at different pressures, temperatures, and oxygen concentrations in a flow reactor, with chlorine initiated production of the respective radicals. For this molecule, only one γ-KHP isomer can be formed. Their results at 206 kPa and 575 K showed that increasing O_2 concentration also increased the relative intensity of the KHP signal (Figure 20). The authors used a recent *neo*-pentane model [110] to simulate their observations. The time-dependent profile shape of

KHP, and its temperature- and O_2 concentration-dependent production were well predicted by the model.

Table 5: Ketohydroperoxides measured during fuel thermal oxidation in JSR. Only studies reporting ketohydroperoxides mole fractions, or signals as a function of temperature, are listed.

KHPs	fuel	T (K)	P (kPa)	τ (s)	fuel (%)	φ	diagnostics	IE (eV)	reference
$C_2H_4O_4$	DME	460-950	93.4	4	2.5	0.5	SVUV-PIMS	~ 10	[180]
$C_3H_4O_4$ [b]	propanal	450-800	101.3	2	2	0.35, 4	SVUV-PIMS	~ 10.3	[250]
$C_4H_8O_3$	*n*-butane	550-800	106.7	6	4	1	SVUV-PIMS	~ 9.3	[123,235]
$C_3H_6O_3$ [b]	*n*-butanal	542-972	93.3	1.38	2	0.8	SVUV-PIMS	~ 9.2	[237]
$C_4H_8O_5$ [b]	12DME	488-954	93.3	1	1	1	SVUV-PIMS	~ 9.4-9.8	[261]
$C_5H_{10}O_3$	*n*-pentane	500-800	106.7	2	1	0.5, 1, 2	SVUV-PIMS SPI-MS	~ 9-9.3	[171]
$C_6H_{12}O_3$ [b]	hexanes	500-750	106.7	2	2 [a]	1	SVUV-PIMS	~ 9-9.5	[254]
$C_7H_{14}O_3$	*n*-heptane	500-850	106.7	2	0.5	0.25, 1, 2, 4	SVUV-PIMS SPI-MS	~ 8.9-9.7	[184,255]
$C_7H_{14}O_3$ [b]	*n*-heptane	500-600	104	2	1	1	SVUV-PIMS	--	[146]
$C_7H_{14}O_3$ [b]	2MHX	530-740	104	0.5	2	1	SVUV-PIMS	~ 8.8-9.5	[252]
$C_8H_{16}O_3$ [b]	25DMHX	470-550	93.3	2	1	1	SVUV-PIMS	~ 8.8-9.6	[258]

Note:

Ketohydroperoxides is abbreviated as KHP.

DME: dimethyl ether, 1,2-DME: 1,2-dimethoxyethane, 2MHX: 2-methylhexane, 25DMHX: 2,5-dimethylhexane.

[a] the fuel mole fraction is 4% for dimethylbutanes.

[b] only signals were reported, not mole fractions.

In recent work by Koritze et al. [262], the KHP in cyclohexene oxidation was measured using the same type of experimentation. Interestingly, the PIE curve obtained for the KHPs was very similar to those measured for KHPs in *n*-butane oxidation [154, 158], this may be due to the probable consequence of ionization by emitting a valence electron from the same structural feature --in this case the -OOH function-- and leading to similar electronic structure.

Identification of several isomeric KHPs was not reported during the preparation of this review; however, the isomeric contributions of KHPs is of critical importance to understanding low temperature oxidation chemistry, because isomeric ratios of KHPs are ultimately linked to initial H-abstraction reactions [251, 254]. When considering complex molecules, more than one initial hydrogen abstraction reaction can occur, forming different ROȮ and ȮOOH radicals.

The correct level of theoretical calculations of ionization energies and fragmentation patterns is an important aspect in the identification of KHPs. It should be noted that identification based on PIE curves alone can be unreliable because of the conformer-dependent calculations. Also, these flexible molecules may have small Franck-Condon overlaps near the ionization threshold, which cause a weak signal that is difficult to interpret. Furthermore, given the large molecular structures, calculations for the ionization energies become more complex and the associated error bars larger.

A unique identification based on the observed and calculated ionization threshold becomes complicated. Given the fact that KHP detection appears to be possible only with a soft ionization mass spectrometric technique, the conversion of the mass spectra into temperature-dependent mole fraction profiles is only possible if the absolute photoionization cross-section is known. In the *n*-butane oxidation experiments of Herbinet et al. [235], KHP was quantified based on an estimated photoionization cross-section and using the butene mole fraction measured by GC as the reference.

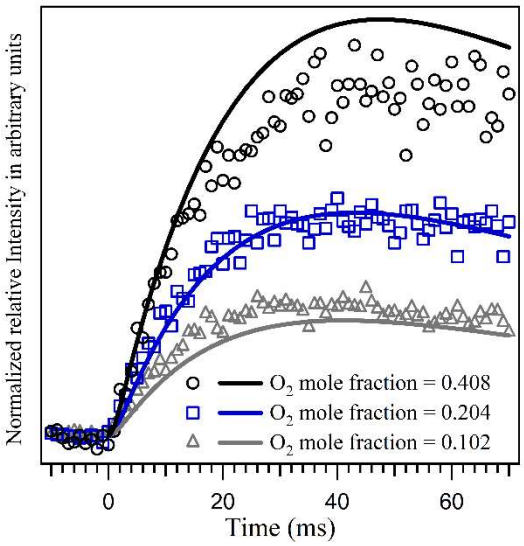

Figure 20: Normalized time-dependent profiles of KHP in *neo*-pentane oxidation in a flow reactor under different O_2 initial mole fractions. Symbols are experimental signals at 575 K and 206 kPa [260]. Lines are simulations by the *neo*-pentane model of Bugler et al. [110] – adapted from results provided by Eskola et al. [260].

Since both molecules have close ionization energy (~ 9.4 eV), the KHP's cross-section was assumed to be identical to the cross section of tetrahydrofuran, which is in the range of 6.6-8.5 Mb from 10 to 11 eV [263]. It was noted that considerable uncertainty accompanies this assumption. As shown in Fig. 21, a discrepancy within a factor of five was observed between the model predicted and the experimentally measured KHP mole fraction. This discrepancy appears to be reasonable considering the estimation of the cross-sections and the fact that no fragmentation patterns were considered in the analysis of KHPs.

In further work on *n*-pentane [171] and *n*-heptane [184] oxidation, photoionization cross-sections, based on the same additivity rules [199] as described in Sections 3.2.2 and 3.2.3, were used to quantify KHPs. The resulting mole fraction was at least one order of magnitudes smaller than the simulated values. These discrepancies can be traced to the break-down of additivity rules for hydroperoxide species. The derived cross-sections were unreasonably large, resulting in very low concentrations. Also, additivity rules determine the total cross-sections, thus fragmentation patterns are inherently not considered in the analysis, leading to additional uncertainties in the procedures used to convert mass spectral signals into mole fraction profiles.

To overcome these problems, Moshammer et al. [180] used calculated photoionization cross sections that were found to be good within a factor of two (Fig. 10) for the small sized molecules they studied. They also found that most of the mass spectral signal of the HPMF (the KHP in the DME oxidation), appears on a fragment peak at m/z = 64 (CH4O3), confirming the importance of including fragmentation patterns, even when using the near-threshold ionization with synchrotron techniques.

Fragments are quite common in mass spectrometry and they can be useful for identification purposes; however, when analyzing a complex reacting mixture, fragmentations can preclude the

exact quantitative interpretation of the mass spectra. Sometimes fragmentation cannot be avoided, even at narrow photon energy distribution and single-photon ionization close to the ionization energy. In the work of Moshammer et al. [180], the identification of CH_4O_3 as a fragment was based on a) the fragment signal with the same temperature trace as the signal of the parent ion, and b) theoretical calculations of the fragment appearance energies, which could be compared to the measured onsets in the synchrotron-based mass-selected PIE scans. This assignment is consistent with the loss of CO after ionization of formic acid esters (note that HPMF can be considered a formic acid ester) [264]. Using this approach, reasonable concentration profiles were determined that compared favorably with the simulations; this is important to note, because the DME oxidation chemistry could be interpreted as being well understood.

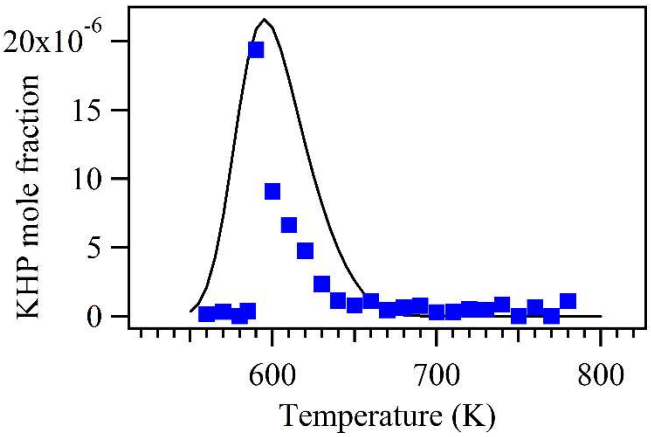

Figure 21: Temperature dependence of KHP mole fraction measured by SVUV-PIMS during nbutane JSR oxidation. Symbols are experimental measurements of KHP. Lines are model prediction of KHP; value is divided by a factor of five – adapted from the results of Ref. [235].

The JSR oxidation study of hexane isomers performed in Hefei [254] has shown that the structure of the fuel molecule affects the formation of KHPs. Figure 22 shows that the maxima of the KHP signal is observed at 553 K for *n*-hexane, 580 K for 2-methylpentane, and 600 K for 3-methylpentane. This phenomenon is related mainly to the reactivity of the fuel molecules; it also indicates that KHP is an indicator of the intramolecular isomerization propensity, e.g., branching of the molecule hinders isomerization of the peroxy radicals.

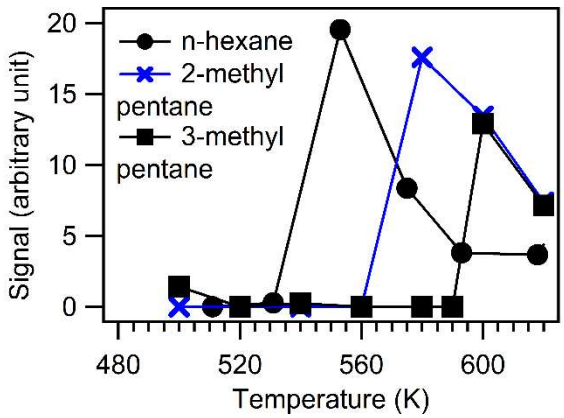

Figure 22: Experimental temperature dependence of the KHP signal (m/z = 132) measured at 10.5 eV during the JSR oxidation of hexane isomers – adapted from results of Ref. [254].

A recent study on the ozone-assisted oxidation of ethylene also revealed the formation of KHP. The experiment was carried out in a JSR from 300 K to 1000 K. The KHP (i.e. $HOOCH_2CHO$) was successfully identified using a combination of the PIE curve recorded by SVUV-PIMS and ab-initio calculations of the corresponding ionization energy. In the quantification, an estimated photoionization cross-section of 5 Mb at 10.5 eV resulted in 5 ppm of KHP at 300 K [48].

In summary, the detection, identification, and quantification of KHPs have become possible in recent years. Advanced mass-spectrometric techniques have become routine; but, using current techniques, the isomeric identification of the KHPs in complex systems is still challenging.

Methods to extract concentration profiles have been successfully improved and tested over the last years; however, these techniques, which heavily rely on theoretical calculations for fragmentation patterns and ionization cross-sections, are still associated with significant uncertainties, limited to small size molecules, and requiring refinement for future procedures.

3.2.5 More complex hydroperoxides

The organic peroxides mentioned above --especially those with the same carbon skeleton as the fuel molecule-- could be produced from the ROȮ and ȮOQOOH radicals in cycles 1 and 2 of Fig. 1. The observation of olefinic hydroperoxides with the same carbon skeleton as the fuel molecule indicates that the ȮOQOOH radicals could undergo HOȮ concerted elimination and/or further intramolecular H-atom isomerization to produce dihydroperoxyalkyl radical. One example from the 2,5-dimethylhexane low-temperature oxidation is shown in Fig. 23.

For the ȮOQOOH radical in Fig. 23(a) (apart from the standard isomerization to the KHP by abstracting the H-atom adjacent to the –OOH group via a six-member ring transition state, and by immediate elimination of an OH), it could undergo an alternative isomerization to dihydroperoxyalkyl radical ($\dot{P}(OOH)_2$) by abstracting the tertiary C-H (via a seven-member ring transition state) [104]. Intramolecular H-atom abstraction of the C-H alpha to the -OOH group by an –OȮ is the standard isomerization usually considered in models in the literature [98, 101]; intramolecular H-atom abstraction from a C-H --not alpha to the –OOH group-- by an –OȮ is an alternative isomerization. The lower bond dissociation energy of the tertiary C-H makes this pathway feasible [104]. This is also indicated by the estimated rate constants in Fig. 23. Once the $\dot{P}(OOH)_2$ radical is produced, it undergoes concerted β-C-O scission to form an olefinic hydroperoxide, or it undergoes cyclization to form a hydroperoxy cyclic ether (HPCE), an isomer of the ketohydroperoxide [109]. The formation of HPCE was already indicated by Battin-Leclerc et al. [154] in *n*-butane low-temperature oxidation modeling in 2011. Here we define the position of –OOH group relative to the radical site in $\dot{P}(OOH)_2$ radical as β, γ, δ, etc. The radical site is at α position. For the β-$\dot{P}(OOH)_2$ radical in Fig. 23(a), its dissociation rate is fast, making the further O_2 addition to the radical site unfavorable, especially under relatively low pressure (e.g. below 10 atm) [105]; however, for the γ-$\dot{P}(OOH)_2$ radical in Fig. 23(b), the rate constant for its cyclization is slow [106]. Thus, further O_2 addition to this radical could compete with its unimolecular reactions, as indicated in Fig. 23(b).

The existence of this channel was also indicated by Jensen et al. [73] during liquid phase auto oxidation of *n*-hexadecane. The author measured species such as trihydroperoxides and hydroperoxy cyclic peroxides with the same skeleton as the initial fuel, allowing them to also consider a mechanism involving three O_2 additions. Several years later, in a gas phase oxidation study of *n*-dodecane at 518 K, the group of Sahetchian [150] measured the di-, and even tri-ketohydroperoxide.

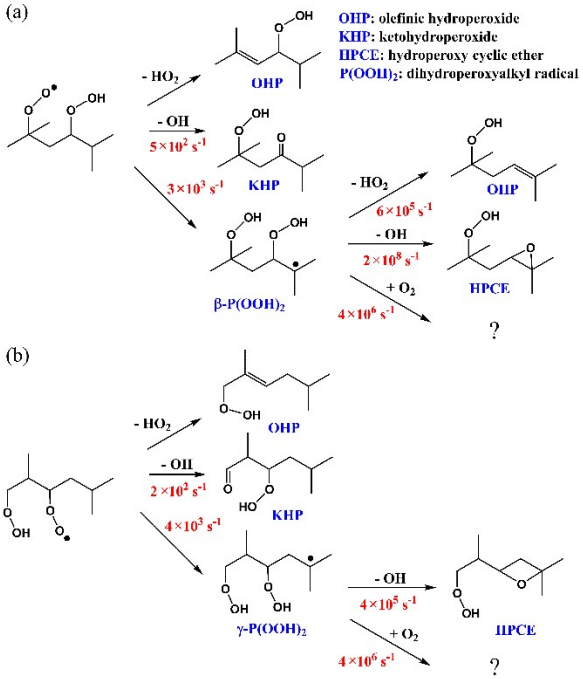

Figure 23: Reaction mechanism of ȮOQOOH radicals in low-temperature oxidation of 2,5-dimethylhexane. Rate constants of ȮOQOOH decomposition to KHP and isomerization to Ṗ(OOH)$_2$ at 500 K, and high-pressure-limit are estimated from Sharma et al. [104]. Rate constant of Ṗ(OOH)$_2$ radicals unimolecular dissociation at 500 K and high-pressure-limit estimated from Villano et al. [106]. Rate constant of oxygen addition to the Ṗ(OOH)$_2$ radicals estimated using O_2 concentration of 21 kPa and literature value of 7×10^{12} cm^3 molecule^{-1} s^{-1} [109].

To explore the fate of the ȮOQOOH radical (i.e. whether or not its alternative isomerization and further O_2 addition to Ṗ(OOH)$_2$ radical occurs), the low-temperature JSR oxidation of 2,5-dimethylhexane was investigated by Wang et al. [258]. The mass spectrum measured at 510 K, employing soft synchrotron-generated photons of 9.5 eV, is presented in Fig. 24.

In addition to the mass peaks corresponding to alkene, cyclic ether, olefinic hydroperoxide, and ketohydroperoxide, two additional peaks were detected that correspond to molecular formulae of $C_8H_{16}O_5$ and $C_8H_{14}O_4$. The temperature profiles of these two intermediates were similar to that of the KHP, indicating that they contained the –OOH function group. Analysis of the fragment pattern also supported the conclusion that these two species are peroxides. The $C_8H_{16}O_5$ intermediate probably has one carbonyl/keto group and two –OOH groups (i.e., a ketodihydroperoxide (KDHP)). The mass interval of cyclic ether ($C_8H_{16}O$), ketohydroperoxide ($C_8H_{16}O_3$), and ketodihydroperoxide ($C_8H_{16}O_5$) is 32 Da. According to Fig. 1, a cyclic ether is produced from the cycle of O_2 addition to the Ṙ radical (i.e., first O_2 addition), while a

ketohydroperoxide is produced from the cycle of O_2 addition to the $\dot{Q}OOH$ radical (i.e., second O_2 addition). Thus, it was postulated that ketodihydroperoxide could be produced from the cycle of O_2 addition to the $\dot{P}(OOH)_2$ radical (i.e., third O_2 addition). The $C_8H_{14}O_4$ species may have two carbonyl/keto groups and one –OOH group (i.e., a di-ketohydroperoxide (DKHP)) compound. Such DKHP isomers could be produced directly from the OH radical-assisted water elimination of theketodihydroperoxide ($C_8H_{16}O_5$) intermediates [265]. Modeling indicated that the mass peak of $C_8H_{16}O_3$ may contribute hydroperoxy cyclic ethers. However, the experiment could not separate them from the ketohydroperoxides, clearly revealing the limitations of the current experimental approaches.

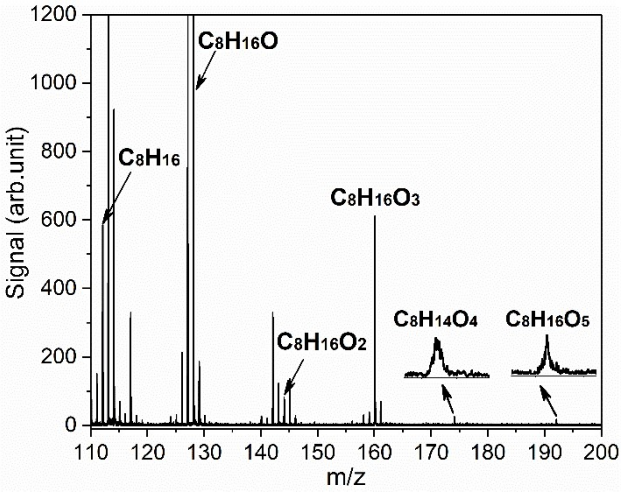

Figure 24: Mass spectrum obtained during low-temperature oxidation of 2,5-dimethylhexane at 510 K and 9.5 eV. Mass peaks corresponding to alkene (C_8H_{16}) and cyclic ether ($C_8H_{16}O$) from first O_2 addition, olefinic hydroperoxide ($C_8H_{16}O_2$) and ketohydroperoxide ($C_8H_{16}O_3$) from secondary O_2 addition, and di-ketohydroperoxide ($C_8H_{14}O_4$) and ketodihydroperoxide ($C_8H_{16}O_5$) from third O_2 addition are labeled – adapted from results of Ref. [258].

Further studies by Wang et al. [172, 252] revealed that the highly oxygenated intermediates with four and five oxygen atoms added to the fuel molecule were produced during the low-temperature oxidation of normal alkanes (e.g., *n*-heptane, *n*-decane, and *n*-dodecane), branched alkanes (e.g., 2-methylhexane, 2-methylnonane, 4-methylheptane, and 2,7-dimethyloctane), cycloalkanes (cyclohexane, cycloheptane, methylcyclohexane, *n*-butylcyclohexane), aldehyde (e.g., decanal), ketone (e.g., 2-decanone), alcohol (e.g., 1-decanol), ether (e.g., dipentyl ether), and ester (e.g., methyl decanoate). In the JSR experiments analyzed by the SVUV-PIMS, the elemental composition of these intermediates was clarified during examination of the low-temperature oxidation reactions with O_2 and $^{18}O_2$ as the oxidizer, respectively. In addition, the atmospheric pressure chemical ionization orbitrap mass spectrometer, with mass resolution of ~100000, was used to study the low-temperature oxidation process [146]. The highly oxygenated intermediates detected by the SVUV-PIMS were confirmed by this additional experiment. The number of the -OOH groups in the highly oxygenated intermediates was clarified by adding D_2O into the low temperature oxidation reaction system. The H/D exchange reaction occurred when the –OOH group in the highly oxygenated intermediates reacted with D_2O [61]. Figure 25 shows the mass spectra and PIE curves of the $C_{10}H_{20}O_3$, $C_{10}H_{18}O_4$, and $C_{10}H_{20}O_5$ intermediates with and without the addition of D_2O into the reaction process of 2,7-dimethyloctane low-temperature oxidation.

The mass peak of $C_{10}H_{20}O_3$ in Fig. 25(a) is shifted by 1 Da, which supports the theory that the KHP has one –OOH. In the $C_{10}H_{18}O_4$ intermediate in Fig. 25(b), its mass peak is dominantly shifted by one, indicating that this species also has one –OOH. In the case of $C_{10}H_{20}O_5$ in Fig. 25(c), the mass peak is shifted by 1 Da and 2 Da, respectively. Thus, the $C_{10}H_{20}O_5$ intermediate has two –OOH groups. The PIE curves of the parent molecule and the corresponding deuterated molecule in Fig. 25(d-e-f) were identical, further supporting the conclusion that they are the same compounds.

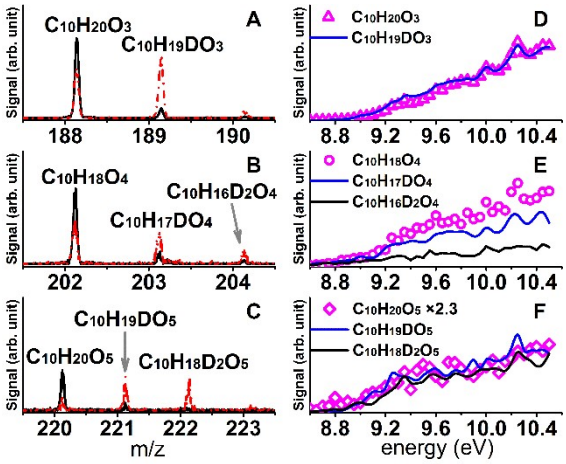

Figure 25: Photoionization mass spectra and photoionization efficiency curves of $C_{10}H_{20}O_3$, $C_{10}H_{18}O_4$, and $C_{10}H_{20}O_5$ with and without D_2O addition. A-C, mass spectra of $C_{10}H_{20}O_3$, $C_{10}H_{18}O_4$, and $C_{10}H_{20}O_5$ with (dashed red lines) and without D_2O addition (black lines) at 530 K and 9.5 eV. D-F. Photoionization efficiency spectra of $C_{10}H_{20}O_3$, $C_{10}H_{18}O_4$, and $C_{10}H_{20}O_5$ (open symbols) and corresponding deuterated species (lines) at 530 K. Signal of $C_{10}H_{20}O_5$ in F multiplied by 2.3. Reproduced from Ref. [172] with permission of PNAS.

Based on these findings, Wang et al. [172] proposed a generalized reaction scheme for the low temperature oxidation of hydrocarbon and oxygenated molecules, driven by the successive reactions of the fuel radical (i.e., O_2 additions and intramolecular H-atom migrations). The important radical intermediates were ROȮ, Q̇OOH, ȮOQOOH, Ṗ(OOH)$_2$, ȮOP(OOH)$_2$, and Ṫ(OOH)$_3$ in Fig. 26. Specifically, ROȮ radicals (peroxy radicals) produced by the O_2 addition to Ṙ radicals; Q̇OOH radicals (hydroperoxyalkyl radicals) generated from the isomerization of ROȮ radicals; ȮOQOOH radicals (hydroperoxyalkyl peroxy radicals) produced from the O_2 addition to Q̇OOH radicals; Ṗ(OOH)$_2$ radicals (dihydroperoxyalkyl radicals) generated from the isomerization of ȮOQOOH radicals; ȮOP(OOH)$_2$ radicals (dihydroperoxyalkyl peroxy radicals) produced from the O_2 addition to Ṗ(OOH)$_2$ radicals; and Ṫ(OOH)$_3$ radicals (trihydroperoxyalkyl radicals) formed from the isomerization of ȮOP(OOH)$_2$ radicals. The dissociation of these important radical intermediates led to products with zero to five oxygen atoms added to the fuel molecules. Possible structures of these products are olefins ($C_{10}H_{20}$), cyclic ethers ($C_{10}H_{20}O$), olefinic hydroperoxides ($C_{10}H_{20}O_2$), ketohydroperoxides and/or hydroperoxy cyclic ethers ($C_{10}H_{20}O_3$), olefinic dihydroperoxides ($C_{10}H_{20}O_4$), ketodihydroperoxides and/or dihydroperoxy cyclic ethers ($C_{10}H_{20}O_5$). The formula in the brackets in Fig. 26 are examples from the oxidation of 2,7-dimethyloctane.

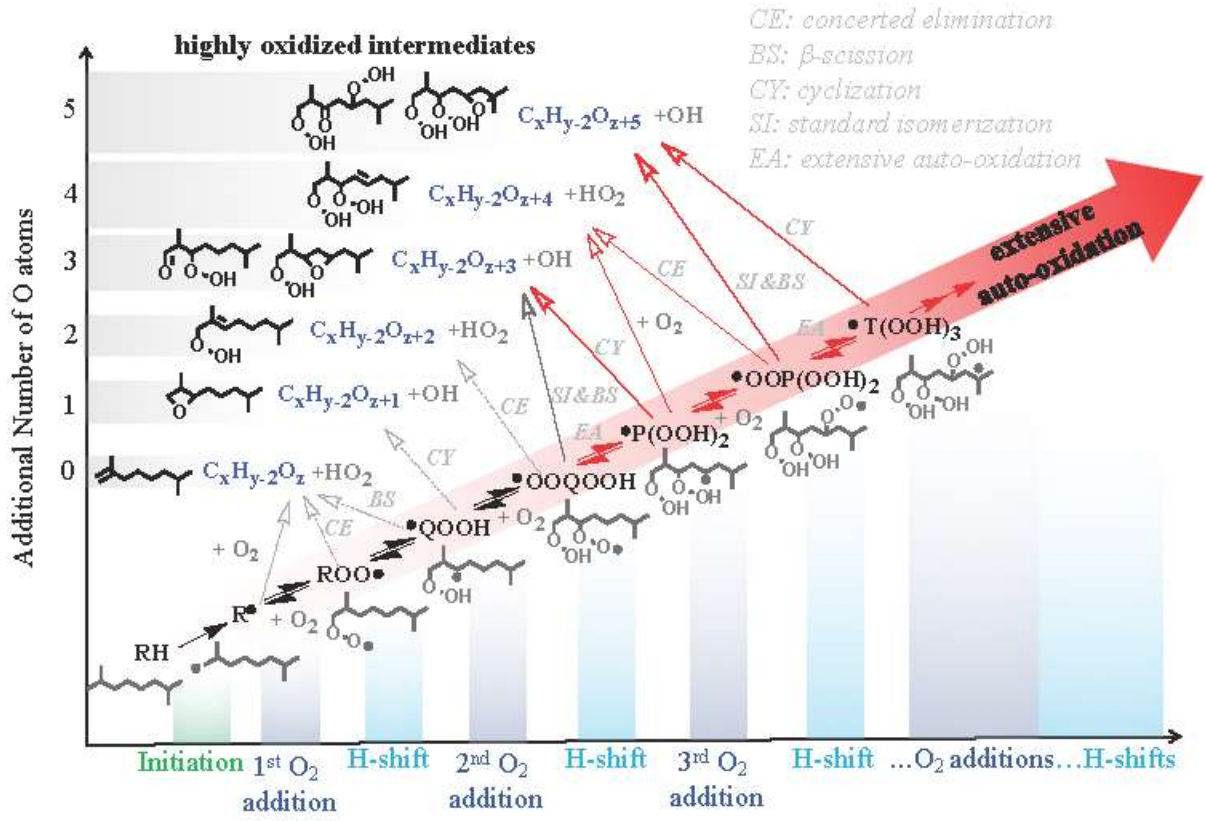

Figure 26: Generalized low-temperature oxidation mechanism of organic compounds (i.e., $C_xH_yO_z$), involving formation of intermediates with molecular formula of $C_xH_{y-2}O_{z+n}$ (n=0-5, labeled in blue). Structures of probable intermediates for low-temperature oxidation of R with a radical site at the primary carbon of 2,7-dimethyloctane are presented. Pathways to $C_xH_{y-2}O_5$ and $C_xH_{y-2}O_3$ highly oxygenated intermediates are highlighted with bold arrows – reproduced from Ref. [172] with permission of PNAS.

The formation of the highly oxygenated intermediates with five oxygen atoms added to the fuel radical is affected by its molecular structure. The relative ratios of the highly oxygenated products with five oxygen atoms, to ketohydroperoxide with three oxygen atoms, in the oxidation of *n*-heptane, 2-methylhexane, 2,5-dimethylhexane, cycloheptane, *n*-decane, 2-methylnonane, 2,7-dimethyloctane, *n*-butylcyclohexane, were estimated by assuming that these two types of species have the same total photoionization cross-sections. Under the experimental conditions of near one atmosphere, equivalence ratio of 1.0, and argon dilution of ~88%, the ratio varied between 1% (*n*-heptane) and 13% (*n*-butylcyclohexane), as shown in Fig. 27. The general trends were (1) for molecules with the same functional group, the longer carbon chain increased the O_5/KHP ratio; (2) for molecules with similar size, the ratio was smallest for normal alkanes, followed by branched alkanes, and highest for cycloalkanes. The experimental observation was supported by quantum chemistry calculation, which revealed that the number of tertiary C-H bonds and cyclic ring structures favored the alternative isomerization of ȮOQOOH radical to $\dot{P}(OOH)_2$ radical and further promoted the subsequent O_2 addition [172].

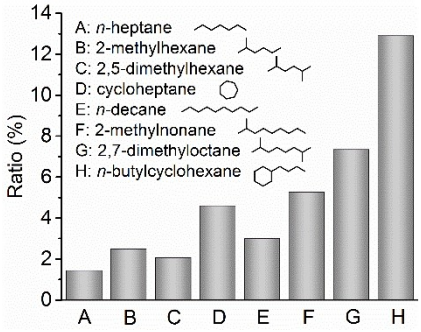

Figure 27: Relative ratios of $C_xH_{y-2}O_5$ to $C_xH_{y-2}O_3$ in eight hydrocarbon low-temperature oxidation reactions, indicating the likelihood of alternative isomerization of ȮOQOOH and third O_2 addition reaction affecting the propensity to produce heavier highly oxygenated intermediates (i.e., $C_xH_{y-2}O_5$) – reproduced from Ref. [172] with permission of PNAS.

The observation of highly oxygenated intermediates was made in an ideal reactor under much lower pressure than that of engine combustion. One question is whether these highly oxygenated intermediates from the generalized low-temperature oxidation mechanism are produced in engine relevant conditions. To answer this question, Wang et al. [146] investigated *n*-heptane low temperature oxidation in both a JSR and a CFR engine. Conditions for the JSR experiment included 1% of fuel, equivalence ratio of 1.0, and a pressure of 101.3 kPa. CFR engine specifications and test conditions are shown in Table 6. Under these conditions, *n*-heptane was partially oxidized, while ignition was avoided.

Table 6. CFR engine specifications and test conditions. Reproduced from Ref. [146] with permission of Elsevier.

Engine Type	**Single Cylinder**
Injection system	Port fuel injection
Bore	82.55 mm
Stroke	114.3 mm
Connecting rod length	254 mm
Compression ratio	8.3
Engine speed	600 RPM
Fuel/air Eq. ratio	0.3
Intake pressure	98 kPa
Inlet air temperature	27±1 °C

The products of *n*-heptane low-temperature oxidation in the JSR were sampled via a molecular beam and analyzed by SVUV-PIMS. With partial oxidation of *n*-heptane in the CFR engine, the products were sampled from the exhaust line and condensed in a trap. Methanol dissolved the products, which were then injected into the atmospheric pressure chemical ionization (APCI) source with a syringe and analyzed by the Orbitrap mass spectrometer (OTMS). Intermediates, with zero to five oxygen atoms added to the *n*-heptane molecule, were observed in both experiments and are shown in Fig. 28.

The $C_7H_{14}O_4$ intermediate was not detected by SVUV-PIMS, probably due to the low concentration, while C_7H_{14} was not measured by the APCI-OTMS because of the limitation of the ion source. Note that the mass peaks shown in Fig. 28 (b) are protonated molecular ion peaks $[M + H]^+$ from the parent molecule.

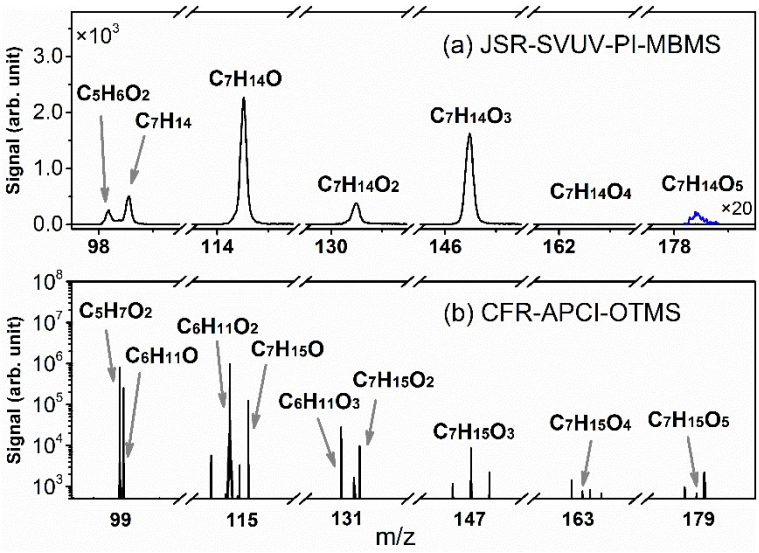

Figure 28: Mass spectra of intermediates with C7H14Ox (x = 0–5) molecular formula in *n*-heptane oxidation in (a) JSR and (b) CFR engine. For JSR experiment, mass spectrometer was obtained at photon energy of 9.6 eV and reactor temperature of 530 K. For CFR engine experiment, products were analyzed by APCI-OTMS; protonated molecular ion peak $[M + H]^+$ are presented - adapted from the results of Ref. [146].

In summary, the more complex hydroperoxides (highly oxygenated intermediates with four and five oxygen atoms added to the fuel molecule) were observed in the low-temperature oxidation of hydrocarbons and oxygenated compounds in ideal reactor (JSR). This type of intermediate was also observed during CFR engine low-temperature oxidation of *n*-heptane. The observation of intermediates with one to five oxygen atoms added to the fuel molecule confirmed the generalized low-temperature oxidation mechanism proposed in Fig. 26.

4 PROGRESS IN UNDERSTANDING HYDROPEROXIDE CHEMISTRY

In parallel to hydroperoxide analyses, studies were conducted to better understand the chemical kinetics of these reactive intermediates, especially for their decomposition pathways. The few kinetic studies related to hydroperoxide reactions are described in Section 4.1. Reaction kinetics of KHPs --especially reactions leading to unusual products, such as carboxylic acids and diones-- are described in Section 4.2. Finally, kinetic models which include the third O_2 addition reactions are discussed in Section 4.3, together with the implication of these reactions in real world systems.

4.1 Kinetic studies on hydroperoxides

This section briefly summarizes kinetic studies that address hydroperoxide reactions. Given its higher stability compared to other hydroperoxides, it is not surprising that hydrogen peroxide is the most studied peroxide molecule; kinetic investigations for organic hydroperoxides are scarce; and there are few kinetic studies for alkylhydroperoxides. However, there has been no experimental kinetic study on ketohydroperoxides and/or even more complex hydroperoxides.

4.1.1 Reactions of hydrogen peroxide

Because of its importance in explaining the H_2-O_2 reactivity [266] and hydrocarbon autoignition [227], the decomposition of hydrogen peroxide has been studied for several decades [267, 268]. However, only a few experimental studies have been performed in the temperature range beyond 900 K. In this temperature condition, this branching reaction is important in the promotion of fuel ignition. Experiments in the literature studies were all performed using shock tubes with sophisticated optical diagnostics [269-272]. In Hong et al. [271], the decomposition rate was followed via the formation of H_2O, which was measured by tunable laser absorption. H_2O_2 decomposition was also investigated theoretically in Ref. [273]. In 2011, analyzing the experimental and modelling studies in the literature, Troe [241] proposed the following rate expression for the reaction (500-1500 K):

H_2O_2 (+M) = ȮH + ȮH (+M):

- $k_\infty = 2.0\times10^{12}\ T^{0.9}\ \exp(-24534/T)\ s^{-1}$ (high-pressure limit),
- $k_0 = 3.94\times10^{24}\ T^{-2.3}\ \exp(-24534/T)\ cm^3\ mol^{-1}\ s^{-1}$ (low-pressure limit in argon)

This rate constant evaluated for H_2O_2 decomposition has been adopted in many up-to-date kinetic models of hydrocarbon oxidation (Ref. [88]).

Due to atmospheric implications, the other reactions of hydrogen peroxide which were investigated thoroughly were H-abstractions with ȮH radicals, O-atoms, and H-atoms. Most of these studies were carried out near room temperature. Readers are referred to the review by Atkinson et al. [39] in 2004. One of the most recent studies for the reaction of H_2O_2 with hydroxyl radicals was performed by Hong et al. [274], behind reflected shock waves. The experiments were carried out at between 1020 and 1460 K. Tunable diode laser absorption at 2550.96 nm was used to probe H^2O and ring dye laser absorption at 306 nm to follow ȮH radicals. The authors proposed the following rate expression in their studied temperature range:

$k = 4.6\times10^{13}\ \exp(-2630/T)\ cm^3\ mol^{-1}\ s^{-1}$.

At 1020 K, this rate expression leads to a rate constant value of 3.5×10^{12} $cm^3\ mol^{-1}\ s^{-1}$, slightly faster than the value of 2.3×10^{12} $cm^3\ mol^{-1}\ s^{-1}$ obtained from the expression recommended by Baulch et al. [275] between 240 and 1700 K:

$k = 1.6\times10^{18}\ \exp(-14800/T) + 1.9\times10^{12}\ \exp(-215K/T)\ cm^3\ mol^{-1}\ s^{-1}$.

In addition to these reactions, the reaction of hydrogen peroxide with H-atoms was also notably investigated. There are two channels for this reaction:

H_2O_2 + Ḣ ⇄ H_2O + ȮH (channel 1),
⇄ H_2 + HOȮ (channel 2).

The team of Walker [276] proposed the rate constants for the above two reactions at temperatures higher than room temperature. In their work, the decomposition of H_2O_2 was investigated in the presence of hydrogen in a flow reactor between 713 and 773 K.

In 2005, a review by Baulch et al. [275] recommended the following rate constants for these two channels:

$k = 1.02\times10^{13} \exp(-1800/T)$ cm^3 mol^{-1} s^{-1} (channel 1),
$k = 1.69\times10^{12} \exp(-1890/T)$ cm^3 mol^{-1} s^{-1} (channel 2).

4.1.2 Reactions of alkyl hydroperoxides

At the temperature of interest for this review, alkyl hydroperoxides decompose primarily by breaking the weak O-OH bond: ROOH = RȮ + ȮH. Pioneering work by Kirk and Knox [277] determined the rate constants of this reaction in the gas phase pyrolysis of ethyl, isopropyl and t butyl hydroperoxides, mixed with benzene in a flow tube. However, the kinetic parameters widely used in current models for the gas phase decomposition of alkyl hydroperoxides were proposed in
1982 by Sahetchian et al. [278]. The authors studied the decomposition of *n*-heptyl-1 and *n*-heptyl-2 hydroperoxides, added in a H_2-O_2 mixture flowing in a dynamic reactor. The hydroperoxides were synthesized via a reaction of heptylmethyl sulfonates with 30% hydrogen peroxide as proposed in Refs. [6, 7]. Rate constants were obtained by following the evolution of the HOȮ radicals. HOȮ radical analysis was performed using electronic paramagnetic resonance, a technique that Sahetchian began to use in Yerevan [279]. The following rate expressions were proposed:

$k = 1.1\times10^{16} \exp(-21892/T)$ s^{-1} (*n*-heptyl-1 hydroperoxide),
$k = 7\times10^{15} \exp(-20886K/T)$ s^{-1} (*n*-heptyl-2 hydroperoxide).

The accuracy of the rate constant for organic hydroperoxides decomposition determines the accuracy of the model prediction because the decomposition of the O-OH bond is the determining hydroperoxide consumption pathway. As shown in Fig. 29, the activation energy of this reaction has a significant effect on temperature dependence of the mole fractions of allyl hydroperoxide during JSR oxidation of hydrocarbon [119, 184].

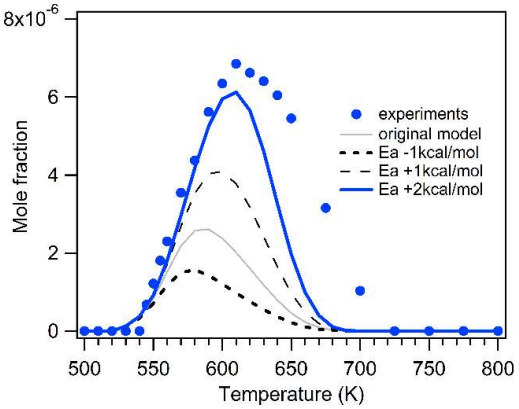

Figure 29: Influence of activation energy of O-OH bond decomposition on temperature dependence of allyl hydroperoxide mole fraction during *n*-heptane JSR oxidation – adapted from results in Ref. [184].

Current models usually use a single value for the rate constant of this O-OH bond decomposition and do not consider the exact structure of the hydroperoxide. As demonstrated by the good agreement between experimental and modeling results in the recent papers reviewed in Section 3.2.2, this assumption is appropriate for CH_3OOH. However, Sahetchian et al. [278] found a difference of 2 kcal/mol for the bond dissociation energy between *n*-heptyl-1 and *n*-heptyl-2-hydroperoxides. More studies on this decomposition would certainly be valuable to improve hydroperoxide predictions.

An accurate prediction of the hydroperoxide also relies on thermodynamic data. In the case of allyl hydroperoxide in Fig. 29, Rodriguez et al. [184] estimated the thermodynamic data using quantum chemistry calculation and the atomization method. The thermodynamic values ($\Delta_f H_0$(298K), -12.1 kcal/mol; S_0(298K), 78.6 cal/mol/K; and Cp (300K), 22.6 cal/mol/K) are close to the evaluation of Goldsmith et al. [280] (-11.9 ± 0.9 kcal/mol, 82.0 ± 2.1 cal/mol/K, 25.1 ± 0.7 cal/mol/K).

Several studies reported the thermodynamic properties of C_1-C_4 alkyl hydroperoxides, C_2-C_5 olefinic hydroperoxides, and C_3 KHPs [184, 280, 281]. For the larger hydroperoxides, however, thermodynamic data were usually estimated by the group additivity method [88, 282, 283], and may have larger uncertainties. Further investigations on the methods would be required to better evaluate the thermodynamic properties of the complex hydroperoxides. Due to the high interest in organic hydroperoxides in atmospheric chemistry, the H-abstraction rate constant by ȮH radicals from a few hydroperoxides were also investigated, and the ȮH radical was photolytically generated. For methyl hydroperoxide, studies were performed by Vaghjiani and Ravishankara [12], Niki et al. [284], and Wang and Chen [285]. The three studies used FTIR spectroscopy to analyze CH_3OOH with a FTIR spectrum provided in Ref. [284]. There are two channels for the reaction of CH_3OOH with ȮH radicals:

$CH_3OOH + \dot{O}H \rightleftarrows H_2O + \dot{C}H_2OOH$ (channel 1),
$\rightleftarrows H_2O + CH_3O\dot{O}$ (channel 2).

The experiments focused on the measurement near room temperature. However, the study by Vaghjiani and Ravishankara [12], with CH_3OOH prepared by methylation of hydrogen peroxide, was conducted in the temperature range of 203-423 K. In this work, the following rate expressions were proposed:

$k = 1.76\times10^{12} \exp(190/T)$ cm^3 mol^{-1} s^{-1} (channel 1),
$k = 1.07\times10^{12} \exp(220K/T)$ cm^3 mol^{-1} s^{-1} (channel 2).

These experimental data in the work of Vaghjiani and Ravishankara [12] are in good agreement with theoretical calculations by Luo et al. [286]. Using a similar experimental method as for methyl hydroperoxide, a measurement for the rate constant of the reaction of ethyl hydroperoxide with ȮH radical was also reported at room temperature (3.6×10^{12} cm^3 mol^{-1} s^{-1}) by Wang and Chen [287].

In addition, the H-abstraction rate constant by ȮH radicals was measured for tert-butyl hydroperoxide [288] between 206 and 375 K:

$k = 4.21\times10^{11} \exp(485/T)$ cm^3 mol^{-1} s^{-1}.

The kinetics of the H-abstraction by ȮH radicals were also investigated for hydroxymethyl hydroperoxide (HMHP) [289], one of the most abundant hydroperoxides in the atmosphere (see part 1.1), and for isoprene hydroxy hydroperoxides produced during the atmospheric oxidation of isoprene. Further oxidation of isoprene hydroxy hydroperoxides was indicated as a source of SOA [290].

4.2 Kinetics of ketohydroperoxides and implementation in mechanisms

This section describes how KHP decomposition is currently understood: first through the usual unimolecular loss of an ȮH radical (Section 4.2.1), then via unimolecular isomerization to organic acids (the so-called Korcek mechanism (Section 4.2.2)), and lastly by pathways involving dione formation (Section 4.2.3), postulated after the detection of dione intermediates in hydrocarbon oxidation [235].

4.2.1 Unimolecular OH loss of ketohydroperoxides and subsequent reactions

Based on the measurement by Sahetchian et al. [278] for the decomposition of heptyl hydroperoxides, a rate constant of $k = 1.0\times10^{16} \exp(-21640/T)$ s^{-1} for reaction type 24: Ketohydroperoxide decomposition, was adopted by Curran et al. [98] in their *n*-heptane oxidation model. Since then, many hydrocarbon oxidation models proposed in the literature have included this reaction, with a rate constant close to this value [84] (activation energies are normally in the ± 1 kcal/mol range and A-factors are in the range of a factor of ~2). Although KHP dissociation with the release of the ȮH is the crucial step for fuel ignition, experimental and theoretical studies for the rate constants of this reaction are scarce. Goldsmith et al. [291] used quantum chemistry calculations to investigate the decomposition of the γ-KHP obtained during propane oxidation.

Here, γ-KHP is the KHP, in which the carbonyl (-C=O) and hydroperoxy (-OOH) groups are separated by one $-CH_2$ in the carbon chain. A rate constant of $k = 1.8\times10^{16} \exp(-21640/T)$ s^{-1} was reported. This rate expression is close to the study of Sahetchian et al. [278]. Later, Goldsmith et al. [292] revisited the calculation of this reaction by considering the effect of non-thermal energy distributions of the γ-KHP intermediate. The result showed a possibly significant decomposition of KHPs before thermalization, at higher internal energies and lower pressures. However, more kinetic studies from both experimental and theoretical calculation on this type of reaction would certainly be of interest, and beneficial to the improvement of hydrocarbon oxidation modelling.

Moreover, the reliable measurements of KHP concentrations could help to establish a rate constant when models are tuned to predict the experimental data.

As shown in Fig. 30, in hydrocarbon oxidation, the decomposition of KHP via the loss of an ȮH radical leads to ketoalkoxyl radicals. On one hand, the β-C-C scission of this radical through the

C-C bond close to the carbonyl group leads to aldehydes --important intermediates during low temperature oxidation (channel 1). On the other hand, the β-C-C scission of this radical through the C-C bond away from the carbonyl group produces diones (channel 2), as will be discussed in Section 4.2.3. Estimated rate constants indicate that these two channels are competitive. A recent study of *n*-heptane low-temperature oxidation [146] detected diones with two to six carbon numbers, confirming the feasibility of this second reaction channel.

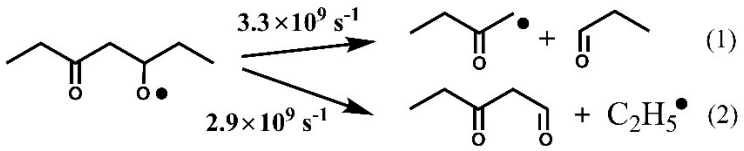

Figure 30: Possible pathways for decomposition of ketoalkoxyl radical. Radical obtained via loss of an ȮH radical from a KHP formed in *n*-heptane oxidation. Rate constants of two reactions at 600 K estimated from Refs. [255] and [293], respectively.

Furthermore, in ether oxidation, the decomposition of the KHP via the ȮH loss is a source of acids. Large amounts of acids have been observed during the oxidation of dimethyl (DME) and diethyl (DEE) ethers.

In 2000, Curran et al. [169] studied the oxidation of DME using the Princeton flow reactor; they reported formic acid as a major product. In these experiments, formic acid was detected and quantified by FTIR. These results were reproduced well by a model proposed by the authors. The formation of formic acid during DME oxidation was confirmed by further experimental studies in tubular reactors using FTIR [294], EI-MBMS [234, 295], and GC with thermal conductivity detector [296].

Similar to this previous work, Moshammer et al. [180] quantified formic acid during their JSR oxidation study of dimethyl ether. Performic and carbonic acids were also detected. The model prediction for formic acid was satisfactory using the model of Burke et al. [242] and Wang et al. [243]. In both models, formic acid was produced from the $\dot{O}CH_2OCHO$ radical, the dissociation product of HPMF (i.e., the KHP from DME oxidation), after breaking the O-OH bond. However, the specific reaction mechanism for formic acid from $\dot{O}CH_2OCHO$ radical was different in the two models.

In the model by Burke et al. [242], the reaction mechanism for formic acid was that proposed by Curran et al. [169] in 2000. The reaction starts from the intramolecular isomerization of $\dot{O}CH_2OCHO$ to give $HOCH_2O\dot{C}O$ via a five-member ring transition state. The decomposition of this intermediate led to formic acid (HOCHO), CO, and an H-atom. Later, a facile pathway to formic acid from the $\dot{O}CH_2OCHO$ radical (i.e., $\dot{O}CH_2OCHO \rightleftarrows HOCHO + H\dot{C}O$), was explored by Andersen and Carter [51, 297]. This pathway, highlighted in Fig. 31, was further confirmed by Wang et al. [243], with high level quantum chemistry calculation, and used in their DME oxidation model. Compared to this pathway, the calculation shows that the intramolecular isomerization of $\dot{O}CH_2OCHO$ to $HOCH_2O\dot{C}O$ is not important.

In addition to these channels, the Korcek reaction of HPMF could also produce formic acid [157, 180]. However, other theoretical calculation revealed that HMPF can easily dissociate into formic acid, and the smallest Criegee intermediate (CH_2OO) [51-54], instead of dissociation via the Korcek mechanism (Section 4.2.2). This pathway could be another source of formic acid in DME low-temperature oxidation.

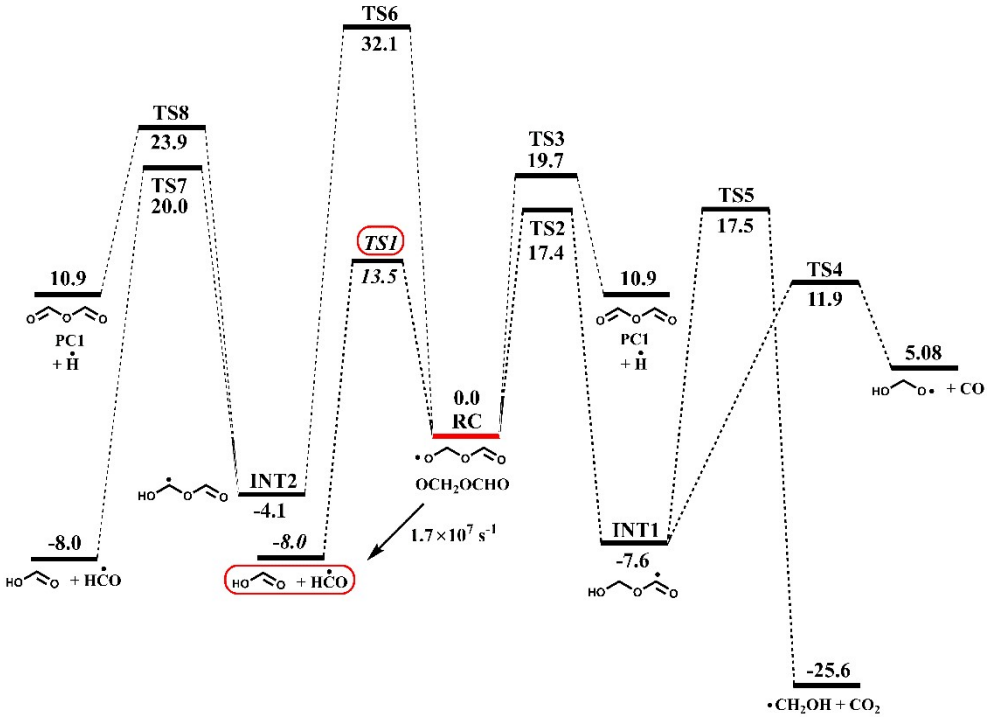

Figure 31: Reaction pathways of $\dot{O}CH_2OCHO$ radical at UQCISD(T)/CBS//B3LYP/6311++G(d,p) level of theory (unit: kcal/mol). Lowest barrier pathway from the $\dot{O}CH_2OCHO$ radical to formic acid and $H\dot{C}O$ highlighted and calculated high-pressure-limit rate constant at 600 K is presented - redrawn from results of Ref. [243] with permission of Elsevier.

In two recent JSR oxidation studies of diethyl ether (DEE) by Serinyel et al. [298] and by Tran et al. [299], acetic acid was also observed as an abundant product. The high concentration of this acid made it easily quantified by GC, even though the presence of two O-atoms in a C_2 molecule made the detection by flame ionization detection unfavorable. Consumption of the DEE and the formation of acetic acid from the work of Tran et al. [299] are shown in Fig. 32. Their kinetic model, based on the theoretical calculations from Sakai et al. [300], predicted the experimental observation well. The rate analysis revealed that over 90% of the consumption of DEE led to KHP, $CH_3CH(OOH)OC(O)CH_3$, which decomposed into $CH_3CH(\dot{O})OC(O)CH_3$ and $\dot{O}H$ radicals. In the model, the subsequent reactions of this intermediate followed the analogous reaction as $\dot{O}CH_2OCHO$ and led to acetic acid. The rate constant of this reaction is assumed to be identical to that of $\dot{O}CH_2OCHO$, calculated by Wang et al. [243]. However, the activation energy was reduced by 2 kcal/mol, considering the difference in bond dissociation energies between the primary- and secondary-carbon positions. The rapid formation of KHP, and its selective reaction to acetic acid, explains both the very high reactivity of DEE and the abundant formation of acetic acid at low temperatures (maximum mole fraction above 2.5×10^{-3}). When the temperature increased, β-scission reactions of the $\dot{Q}OOH$ radical were more favorable because of the O-atom in the fuel

molecule. The pathway could compete with the channels leading to the KHP, explaining the particular shape of the NTC zone displayed in Fig. 32.

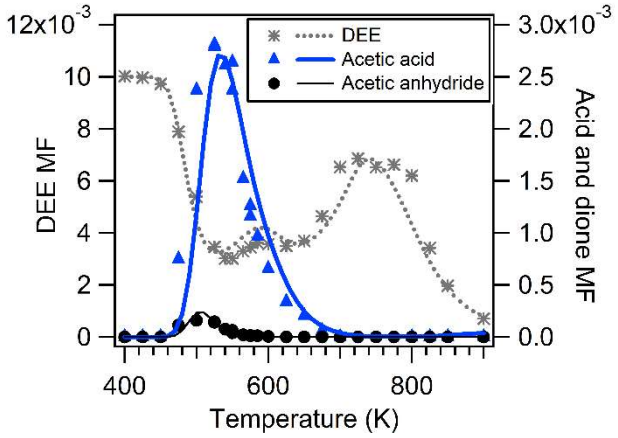

Figure 32: Experimental (symbols) and simulated mole fraction (MF) profiles of fuel, acetic acid and acetic anhydride during the JSR oxidation of DEE by Tran et al. – adapted from the results of Ref. [299].

The model underestimated the acetic acid formation by a factor of two to three in the work of Serinyel et al. [298]. The main reaction pathway for acetic acid is:

$CH_3\dot{C}O + O_2 \rightleftharpoons CH_3C(O)O\dot{O}$
$CH_3C(O)O\dot{O} + H\dot{O} \rightleftarrows CH_3COOH + O_2 + .O.$
$CH_3C(O)O\dot{O} + CH_3O\dot{O} \rightleftarrows CH_3COOH + O_2 + CH_2O.$

The last two reaction channels are overall reactions, details of which can be found in Refs. [29, 40]. The authors mentioned that underestimation may be partly due to uncertainties in the fate of the methylperoxy radicals ($CH_3O\dot{O}$), as well as missing pathways. Regarding this discussion, the pathway of KHP to acetic acid might be the missing pathway.

Formic acid was also observed as an important intermediate during the JSR oxidation of dibutylether by Thion et al. [301]. In their model, formic acid was mainly formed from the addition of $\dot{O}H$ radical to formaldehyde. The model over-predicted the mole fraction of formic acid; however the authors deduced that this may have been caused by the over-prediction of formaldehyde in the model.

4.2.2 Korcek decomposition and the formation of acids

To avoid negative impact on the environment [302], it is important to better understand the potential for direct emissions of monocarboxylic acids from the combustion process. To this end, Battin-Leclerc et al. [303] proposed tentative channels to predict acid formation in combustion systems, such as the addition of $\dot{O}H$ radicals to formaldehyde, leading to formic acid, reactions of ketene to form acetic acid, and/or the possible decomposition of ketohydroperoxides embedded in a cyclic ether, which are produced from the secondary reactions of cyclic ethers.

Even though the presence of short chain monocarboxylic acids (formic acid (HCOOH), acetic acid (CH_3COOH), propionic acid (C_2H_5COOH)) at the exhaust line of the internal combustion engines has been reported since 1999 [304], their formation in laboratory combustion systems was seldom reported before 2010. In contrast, carboxylic acids were first found to be significant products from the liquid phase oxidation of hydrocarbons by Korcek et al. [73, 82]; C_2 to C_7 alkanoic acids were quantified during their study of pentaerythrityl tetraheptanoate auto-oxidation [82]. The authors postulated that the carboxylic acids are produced from γ-KHPs [305].

Carboxylic acids were also observed during the gas phase oxidation of hydrocarbons. Using FTIR, formic acid was quantified in 1999 by Cernansky's team during the oxidation of *neo*-pentane in a flow reactor [306]. In their model, the authors considered an additional reaction of an ȮH radical to formaldehyde; under-prediction of this acid at a low temperature encouraged the authors to consider other pathways to formic acid.

In 2010, Herbinet et al. studied *n*-butane oxidation in a JSR by SVUV-PIMS [235]. The formation of a significant amount of acetic acid (m/z = 60) was reported, with a maximum mole fraction of around $1x10^{-3}$. A large peak of formic acid (m/z = 46) was also observed, but not quantified. Acetic acid was quantified by the same team [108] during the JSR oxidation of propane using both GC and SVUV-PIMS. For both hydrocarbons, satisfactory agreement was found between GC and SVUV-PIMS measurements (Fig. 33 (a) and (b)). A comparison between the experimental and simulated mole fractions of acetic acid during the JSR oxidation of linear C_3, C_4 and C_7 alkanes [108, 235, 255] is presented. Discrepancies observed between the modeled and experimental profiles in propane and *n*-butane oxidation are not currently understood.

The Nancy-Hefei team also reported the formation of acetic and propanoic acids during the JSR oxidation of isomers of hexane [254], *n*-pentane [111], and *n*-heptane [255] using GC or SVUV PIMS. Quantification of these organic acids in the SVUV-PIMS experiment was achieved by measuring the absolute photoionization cross-section of acetic acid and propanoic acid, as shown in Fig. 34. The ionization energy of the acid is normally higher than that of the olefinic hydroperoxide isomer. For example, the ionization energy of propanoic acid is 10.44 eV, while for allyl hydroperoxide it is 9.55 eV [171]. The signal measured for acids may contain the signal of the olefinic hydroperoxide isomers. The PIE curve for $C_3H_6O_2$ measured during *n*-heptane oxidation [146] is presented in Fig. 34. Apart from the ionization energy onset close to propanoic acid (~ 10.36 eV), the onset of the allyl hydroperoxide isomer is clearly observed at ~ 9.45 eV. In the work on *n*-heptane by Rodriguez et al. [184], the peak at m/z = 74 could correspond to both propanoic acid and allyl hydroperoxide at 11 eV. However, the maximum propanoic acid mole fraction is around $6x10^{-5}$ [255], notably larger than that of allyl hydroperoxide at around $7x10^{-6}$ (Fig. 29).

As discussed above, acetic acid measured by GC and SVUV-PIMS were in good agreement during the JSR oxidation of propane and *n*-butane. However, this was not the case for the C_{6+} hydrocarbons. For example, in the *n*-heptane JSR oxidation study, the mole fraction of acetic acid and propanoic acid measured by GC differed from those measured by SVUV-PIMS [255]. The shapes of the two profiles from GC and SVUV-PIMS were notably different, with a sharp peak around 550 K for the GC measurement, indicating possible decomposition of KHPs in the GC column, or during the transfer line between the reactor and the inlet of GC [153].

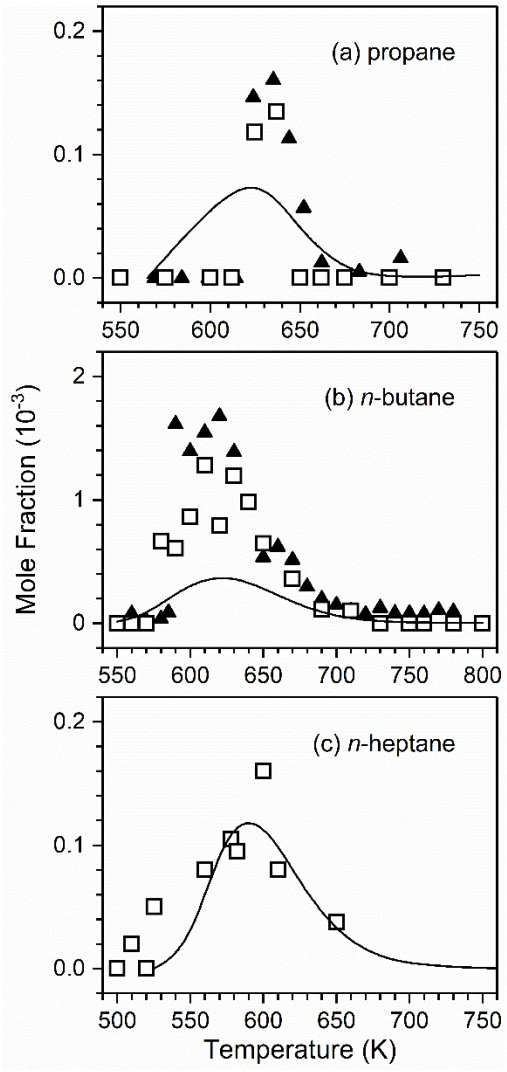

Figure 33: Experimental and predicted mole fraction profiles of acetic acid during propane, *n*-butane and *n*-heptane JSR oxidation. Experimental data (solid symbols by GC, open symbols by SVUV-PIMS) from Refs. [108, 235, 255], and predictions (lines) using the model of Refs. [283, 307], include pathway proposed by Jalan et al. [308].

The presence of formic, acetic, propanoic, and butanoic acids was also reported by Wang et al. [146] in their *n*-heptane JSR oxidation study. Evidence for propanoic acid is shown in Fig. 34(b). The formation of formic acid was also detected by Eskola et al. [260] using SVUV-PIMS during a study of the photo-initiated oxidation of *neo*-pentane in a flow tube.

Table 7 summarizes literature studies on gas phase oxidation of fuels, in which carboxylic acids were quantified. Based on these experiments, several attempts were made to model the formation of carboxylic acids. Herbinet et al. [255] proposed reactions starting from the aldehyde that led to carboxylic acid with the same carbon skeleton, e.g. from acetaldehyde to acetic acid [309]. The reaction starts with H-abstraction of the aldehydic H-atom, O_2 addition to the radical site, and disproportionation of the obtained peroxy radical with an HOȮ radical. As shown in Fig. 4, small aldehydes are common products of alkane oxidation. They can be easily produced from KHP decomposition. This model [255] satisfactorily predicted the acid formation in the case of *n*-heptane oxidation, but deviated by a factor of ten in the case of propane [108].

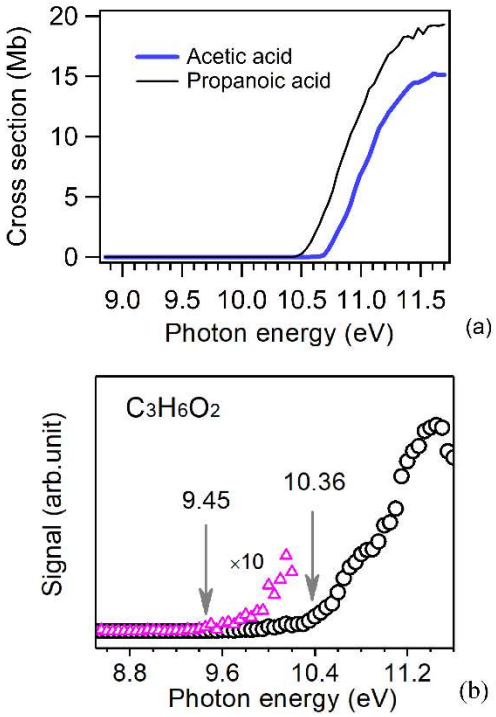

Figure 34: Photoionization of acetic and propanoic acid: (a) absolute cross-section as function of photon energy, (b) photoionization efficiency curve of $C_3H_6O_2$ measured during *n*-heptane oxidation – adapted from the results of Ref. [255] and Ref. [146] with permission from Elsevier.

Following the hypothesis of Korcek et al. [73, 82], that carboxylic acid can be formed from γ-KHPs during alkane oxidation, Jalan et al. [308] used high level computational methods to thoroughly investigate this pathway for the smallest γ-KHP from propane oxidation. They proposed a mechanism that led to formic and acetic acid via a cyclic peroxide isomer of the γ-KHP.

The work by Moshammer et al. [180] detected carbonic acid during the low-temperature oxidation of DME, potentially providing evidence for the Korcek decomposition mechanism. Taking into account the channels proposed by Jalan et al. [308], Goldsmith et al. subsequently [292] investigated the decomposition of the C_3 γ-KHP theoretically. The potential energy diagram that they calculated at a high level of theory is shown in Fig. 35(a), and the branching fractions between the four channels derived from master equation calculations are displayed in Fig. 35(b). This last figure shows that formic acid is the main acid product and acid formation is maximum in the early stages of alkane oxidation around 500 K. The proposed rate expressions at 101.3 kPa in helium for the formation of formic acid and acetaldehyde (k_1) and of acetic acid and formaldehyde (k_2), are respectively:

$k_1 = 2.80\times10^{43}\ T^{-10.22} \exp(-22990/T)\ s^{-1}$ ($k = 7.8\text{x}10^{-5}\ s^{-1}$ at 500 K), and
$k_2 = 3.26\times10^{43}\ T^{-10.36} \exp(-23409/T)\ s^{-1}$ ($k = 1.7\text{x}10^{-5}\ s^{-1}$ at 500 K) [292].

In 2018, Grambow et al. [314] reported the theoretical calculation of 75 possible unimolecular reaction pathways from C_3 γ-KHP. They found that whatever the method, the pathway related to the Korcek mechanism always had the lowest energy transition state. Recent kinetic modeling studies have included the Korcek pathways to carboxylic acid. In a reexamination of their models

for alkane oxidation, Ranzi et al. [283, 307] included a new reaction class from KHPs to acetic acid and used a rate constant for the C_3-KHPs. Their rate values were close to that of Goldsmith et al. [292]:

$k = 5.7\times10^{1}\ T^{2.130} \exp(-13839/T)\ s^{-1}$ ($k = 3\text{x}10^{-5}\ s^{-1}$ at 500 K) [307],

In C_4-KHPs, the rate constant at 500 K is four times larger than that of C_3-KHPs.

$k = 1.4\times10^{7}\ T^{0.94} \exp(-14444/T)\ s^{-1}$ ($k = 1.4\text{x}10^{-4}\ s^{-1}$ at 500 K) [307],

but the estimated value for the C_7-KHPs is even much larger:

$k = 6.8\times10^{5}\ T^{1.130} \exp(-13135/T)\ s^{-1}$ ($k = 3\text{x}10^{-3}\ s^{-1}$ at 500 K) [283].

Table 7: Carboxylic acids measured during fuel thermal oxidation in JSR and FT. Only studies reporting carboxylic acids mole fractions as a function of temperature are listed.

organic acid	fuel	T (K)	P (kPa)	□ (s)	fuel (%)	□	diagnostics	reference
formic acid	DME	550-850	1220-1820	2-4	2.13-3.38	0.7-4.2	FTIR	[169]
formic acid	DME	513-973	101.3	2-4	0.034	0.1	FTIR	[294]
formic acid	DME	400-1150	101.3	0.87-2	0.88	1.06	EI-MBMS	[234][b]
formic acid	DME	538	101.3		10, 22	1.6, 4.1	GC	[296]
formic acid	DME	460-950	93.4	4	2.5	0.5	SVUV-PIMS	[180]
formic acid	acetaldehyde	528-946	98.2	2.7	2.34	0.5	FTIR	[197]
formic acid	propanal	450-800	101.3	2	2	0.35, 4	SVUV-PIMS	[250]
formic acid	*neo*-pentane	620-810	81.1	0.2	0.2	0.3	FTIR	[306]
formic acid	BF	600-1200	1013	0.7	0.09	0.45, 0.9, 1.8	FTIR	[310]
formic acid	DBE	470-1250	101.3 1013	0.07 0.7	0.1	0.5, 1, 2	FTIR	[301]
acetic acid	DEE	400-1100	106.7	2	1	1	GC SVUV-PIMS	[299]
acetic acid	DEE	450-1250	101.3 1013	0.07 0.7	0.1	0.5, 1, 2	GC	[298]
acetic acid	propane	530-730	106.7	6	12	1	GC SVUV-PIMS	[108]
acetic acid	*n*-butane	550-800	106.7	6	4	1	FTIR	[235]
acetic acid butanoic acid	*n*-butanal	542-972	93.3	1.38	2	0.8	SVUV-PIMS	[237]
acetic acid	*n*-pentane	500-800	106.7	2	1	0.5, 1, 2	GC	[111]
acetic acid propanoic acid	hexanes	500-750	106.7	2	2 [a]	1	GC SVUV-PIMS	[254]
acetic acid	PA	700-1250	101.3 1013	0.07 0.7	0.1	0.5, 1, 2	FTIR	[311]
acetic acid propanoic acid	*n*-heptane	500-850	106.7	2	0.5	1	GC SVUV-PIMS	[255]
propanoic acid	EPP	750-1100	1013	0.7	0.1	0.3, 0.6, 1, 2	FTIR	[312]
pentanoic acid	EPT	560-1160	1013	0.7	0.1	0.6, 1, 2	FTIR GC	[313]
hexanoic acid	*n*-hexanal	475-1100	106.7	2	0.5	0.25, 1, 2	GC	[122]

Note:

Formic acid ($CH(O)OH$), IE=11.3 eV [238], acetic acid ($CH_3C(O)OH$), IE=10.65 eV [238], propanoic acid ($C_2H_5C(O)OH$), IE=10.44 eV [238], butanoic acid ($C_3H_7C(O)OH$), IE=10.17 eV [238], pentanoic acid ($C_4H_9C(O)OH$), IE=10.08 eV [171], hexanoic acid ($C_5H_{11}C(O)OH$), IE=10.21 eV [184].

DME: dimethyl ether, BF: butyl formate, PA: propyl acetate, DBE: dibutylether, DEE: diethyl ether, EPP: ethyl propanoate, EPT: ethyl pentanoate.

[a] fuel mole fraction is 4% for dimethylbutanes.

[b] measured in FT, others measured in JSR.

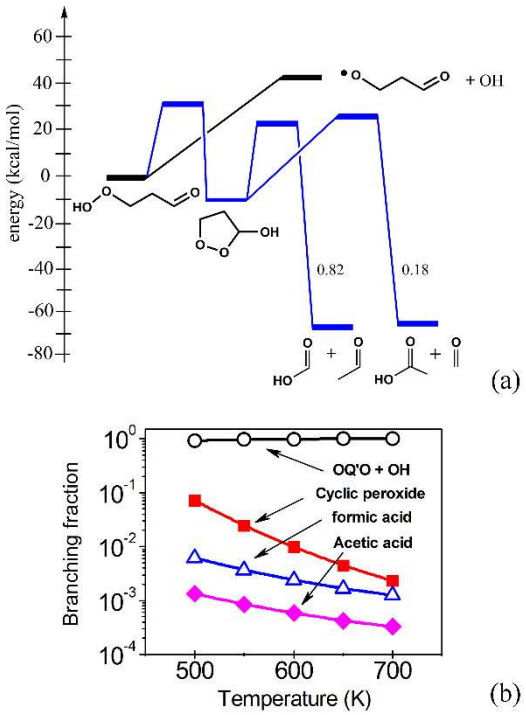

Figure 35: Kinetics of decomposition of C_3 γ-KHP according to the Korcek mechanism, calculated by Ref. [292]: (a) potential energy of KHP decomposition and branching ratio of k_1 and k_2 at 500 K, (b) branching ratios of KHP decomposition at atmospheric pressure and as a function of temperature – adapted from results of Ref. [292], and Ref. [146] with permission from Elsevier.

With these added reactions, the acid mole fraction reported for the JSR oxidation of linear C_3, C_4, and C_7 alkanes [108, 235, 255] was modeled by Ranzi's group [283, 307]. However, the acetic acid in C_3 and C_4 alkanes was still significantly underpredicted --especailly for C_4 alkane, as shown in Fig. 33. The good prediction of acetic acid in C_7 alkane may have been achieved by the much larger rate constant from estimation.

In the recent *n*-heptane kinetic model developed by Zhang et al. [88], these reactions were included with the same rate constants as Ranzi et al [283]. However, the mole fractions of acids measured during *n*-heptane JSR oxidation by Herbinet et al. [255] were significantly underpredicted. The authors stated that this discrepancy could have been caused by the too rapid decomposition rate constants of ketohydroperoxides via –OOH bond dissociation. While both rate expressions are based on that proposed by Sahetchian [278], the global rate constant at 600 K for the decomposition of all KHP isomers in the model of Zhang et al. [88] is about twice that used in the Milano *n*-heptane model [283]. Thus, for a better evaluation of the Korcek reactions, more kinetic work is needed to study the dissociation of KHPs. Furthermore, as discussed by Wang et al. [146], it is very likely that there are other channels for organic acid formation during the gas phase oxidation of alkanes.

Section 4.2.1 examined the importance of carboxylic acids as intermediates during ether oxidation.

Carboxylic acids --including non-alkanoic acids-- have frequently been quantified during the JSR oxidation of other oxygenated fuels; it is particularly important for esters with a C_{2+} alkylic chain, which can easily form an alkanoic acid and an alkene by an unimolecular elimination involving a six-member ring transition state [315]. This explains the large amounts of formic acid, propanoic acid and pentanoic acid observed during the JSR oxidation of butyl formate [310], propyl acetate [311], ethyl propanoate [312], and ethyl pentanoate [313], respectively. For example, in the case of ethyl pentanoate, the following molecular reaction is involved:

$C_2H_5OC(O)C_4H_9 = C_4H_9C(O)OH + C_2H_4$.

Furthermore, carboxylic acids were quantified during JSR oxidation studies of C_2-C_4 aldehydes by SVUV-PIMS [197, 237, 250] and of dibutylether by FTIR [301]. Using acetaldehyde as the fuel, Tao et al. [197] quantified formic and acetic acids, as shown in Fig. 36.

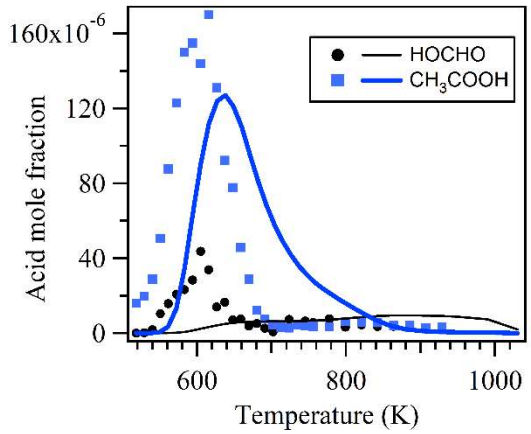

Figure 36: Experimental (symbols) and simulated (lines) mole fraction profiles of C_1-C_2 acids during JSR oxidation of acetaldehyde by Tao et al. - plotted from data in Supplementary Material of Ref. [197].

Simulations using the model of the authors [197] predicted the observed amounts of acetic acid well, but not the temperature where the maximum mole fraction occurred. The kinetic model showed some reactions that may also explain acid formation during alkane oxidation. For example, acetic acid was produced from ketene (CH_2CO), also a potential product of KHP decomposition during alkane oxidation. The ȮH radical addition to ketene formed $\dot{C}H_2COOH$ radical; and the subsequent reaction of this radical with HOȮ radical led to CH_3COOH. In formic acid (Fig. 36), its formation was not satisfactorily predicted. Analysis showed that formic acid was produced from the ȮH radical addition to formaldehyde, and then a C-H β-scission.

In propanal oxidation studied by Zhang et al. [250], the temperature dependence of formic acid was also measured, with a maximum mole fraction around 600 K. The experimental observation was reasonably predicted by the model developed in this work; but the authors did not analyze the major reaction pathways for formic acid. Similarly, the mole fraction of acetic and butanoic acids was measured by Liao et al. in *n*-butanal oxidation [237]. The formation of both acids peaked around 650 K; however, the reaction kinetics for these acids was not discussed in the paper.

4.2.3 Dione formation from ketohydroperoxides

As mentioned in Section 2.2, the Sahetchian group reported the formation of dodecadiones in their low-temperature oxidation study of *n*-dodecane in the gas phase [150]. Most isomers are γ-diones (the dione in which the two carbonyl functions are separated by a $-CH_2-$ group). γ-diones were also observed during the cool flames of hydrocarbons, such as butanal-3-one from *n*-butane and 2,4-pentanedione from *n*-pentane. These diones are important intermediates at temperatures below the cool flame zone [316]. A study by Barusch et al. [316] showed that as much as 10% of the initial *n*-pentane was converted into γ-diones. Before 2010 --and other than in these studies-- the formation of organic compounds including two carbonyl groups was not often reported during gas phase oxidation of fuels under combustion relevant conditions.

In recent work, diones with the same carbon skeleton as the fuel molecule have been widely detected in JSR oxidation of alkanes using SVUV-PIMS [171, 184, 254, 255] or using SPI-MS [171, 184]. One interesting observation is that species including a carbonyl and an alcohol function often formed along with the dione intermediates. The presence of γ-diones was also identified by GC-MS during the oxidation of C_6-C_7 alkanes [254, 255]; however, the temperature dependence of their mole fractions differed from the measurement by SVUV-PIMS [255]. Similar to the observations of carboxylic acids in the GC measurement (see Section 4.2.2), the authors proposed that the additional diones were produced from decomposition of KHP in the GC column and/or during the transfer line between the reactor and the inlet of GC. Table 8 summarizes the studies in the literature of fuel oxidation in the gas phase, in which diones were quantified, or their signals as a function of temperature were measured.

The observation of diones (i.e., C_7-diones) during *n*-heptane oxidation by the Nancy-Hefei team was further confirmed by Wang et al. [146] in their JSR oxidation study of *n*-heptane using SVUV PIMS and APCI-OPMS. These authors also reported intermediates with the molecular formula of $C_nH_{2n-2}O_2$ (n = 2–6), which may potentially be interpreted as C_2–C_6 diones.

Eskola et al. reported the formation of 2,2-dimethylpropanedial that was identified by SVUV PIMS during their study of the photo-initiated oxidation of *neo*-pentane in a flow tube [260].

Unfortunately, they were unable to provide quantitative information. The substantial formation of diones was reflected by its high signal intensity. For example, signal intensities of the diones with the same carbon skeleton as the fuel are the same order of magnitude as those of cyclic ethers, one of the major products during alkane JSR oxidation [146, 171, 184, 254, 255]. This can be seen in Fig. 4 in Ref. [146], where the signal intensities of cyclic ethers ($C_7H_{14}O$) and diones ($C_7H_{12}O_2$) at 600 K are very similar.

These similar concentrations were also observed during JSR oxidation of *n*-pentane [171]. The measured mole fractions of the C_5-diones are on the order of 1.5×10^{-4} at an equivalence ratio of 0.5 (Fig. 37(a)), close to that of cyclic ethers under the same conditions (Fig. 4). In the quantification of diones, their photoionization cross-sections were estimated from the group additivity method proposed by Bobeldijk et al. [199]. The uncertainty for the dione mole fraction is expected to be lower than for the hydroperoxides (Section 3.2), because the group's

contributions could all be estimated from the analysis of standard species. However, the model could not predict their temperature dependence of formation and mole fractions.

Table 8: Dione intermediates, the same size as the reactant, measured during fuel thermal oxidation in JSR. Only studies reporting diones mole fractions, or signals as a function of temperature, are listed.

diones	fuel	T (K)	P (kPa)	τ (s)	fuel (%)	φ	diagnostics	IE (eV)	reference
$C_4H_6O_3$	DEE	400-1100	106.7	2	1	1	GC	~ 10	[299]
$C_4H_6O_2$	*n*-butane	550-800	106.7	6	4	1	SVUV-PIMS	~ 9.3	[235]
$C_5H_8O_2$	*n*-pentane	500-800	106.7	2	1	0.5, 1, 2	SVUV-PIMS SPI-MS	~ 8.9, 9.3	[171]
$C_5H_8O_2$ [b]	hexanes	500-750	106.7	2	2 [a]	1	GC, SVUV-PIMS	~ 9.1-9.4	[254]
$C_4H_6O_4$ [b]	12DME	488-954	93.3	1	1	1	SVUV-PIMS	~ 9.8, 10.1	[261]
$C_7H_{12}O_2$	*n*-heptane	500-850	106.7	2	0.5	0.25, 1, 2, 4	SVUV-PIMS SPI-MS, GC	~ 9.4	[184,255]
$C_7H_{12}O_2$ [b]	*n*-heptane	500-600	104	2	1	1	SVUV-PIMS	--	[146]
$C_8H_{14}O_2$ [b]	25DMHX	470-550	93.3	2	1	1	SVUV-PIMS	~ 9.0	[258]
$C_{10}H_{18}O_2$	*n*-decane	500-850	106.7	2	0.25	1	GC, SVUV-PIMS	~ 9.0	[184]

Note:
DEE: diethyl ether, 1,2-DME: 1,2-dimethoxyethane, 25DMHX: 2,5-dimethylhexane
[a] the fuel mole fraction is 4% for dimethylbutanes.
[b] only signals were reported, not mole fractions.

The formation of diones also depends on the structure of the fuel. For example, the JSR oxidation study of the five isomers of hexane [254] showed that the branching level of the fuel molecule significantly impacted the formation of C6-diones, which have the same carbon skeleton as the fuel. The linear isomer produced almost an order of magnitude more diones than the dimethyl isomers, assuming that these diones have close photoionization cross-sections (Fig. 37(b)).

The formation of diones was also reported during the gas-phase oxidation of oxygenated fuels. The dione with the same carbon skeleton as the fuel molecule was identified by SVUV-PIMS during the oxidation study of DME [157], DEE [299], and 1,2-DME [261]. In the case of the C_4 ether, Tran et al. [299] also quantified acetic anhydride ($H_3C(O)OC(O)CH_3$) by GC. Model predictions for this compound were very good (Fig. 32). According to the model [299], acetic anhydride resulted from the KHP via the H-abstraction of the C-H adjacent to the –OOH group and a subsequent β-O-O scission.

The production of diones was also reported during the oxidation of a cyclic ether, tetrahydrofuran. The formation of butanedial was observed by Vanhove et al. [317] from rapid compression machine experiments using GC, and by Antonov et al. [259], from photo-initiated oxidation in a flow tube by SVUV-PIMS.

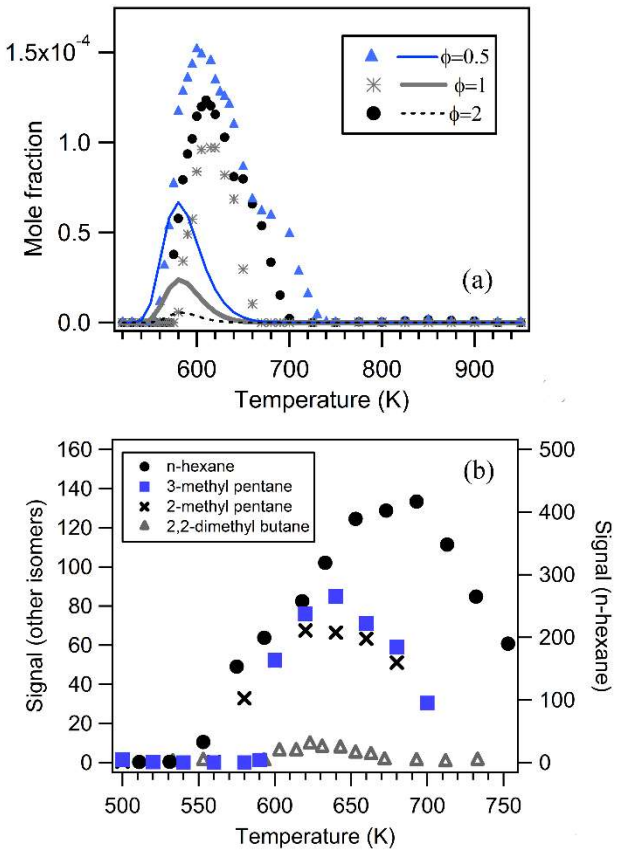

Figure 37: Examples of temperature dependences of mole fraction/signal of diones during JSR oxidation of alkane: (a) experimental (SPI-MS) and computed [111] mole fractions of C_5-diones during *n*-pentane oxidation under conditions of Fig. 4; (b) signal profile of m/z = 114 (i.e., C_6-diones) measured by SVUV-PIMS at energy of 10.5 eV during oxidation of five isomers of hexanes – adapted from results of Refs. [171, 254].

Since the experimental observation of diones in 2010 [235], efforts have been made in both kinetic modeling and theoretical calculations to explore their formation pathways. Fig. 38 summarizes the up-to-date channels proposed in the literature.

In a first-proposed pathway [154], the β-C-H scission of the ketoalkoxy radical leads to diones; the ketoalkoxy radical is derived from the KHP by breaking the O-OH bond. However, in modeling *n*-heptane oxidation [255], these authors found that this channel ($E_a \approx 81$ kJ/mol) cannot compete with the β-C-C scission (Ea ≈ 65 kJ/mol) of the ketoalkoxy radical. Afterward, another channel was postulated, i.e., the molecular decomposition of KHP to produce water and diones. However, even with this additional reaction, the experimental formation of diones was significantly underpredicted.

Later, Ranzi et al. [283, 307] included a new reaction class in their updated modeling of alkane oxidation, in which H-abstractions from KHP led directly to a dione, an ȮH radical, and H_2O. The dione mole fraction obtained during the JSR oxidation of propane, *n*-butane and *n*-heptane [108, 235, 255] was predicted; however, apart from the under-prediction of mole fraction, the temperature dependence of the dione mole fraction in propane oxidation was not reproduced well (Fig. 33). This deviation can also be seen in Fig. 37a, which displays dione profiles computed

during *n*-pentane JSR oxidation by the model of Bugler et al. [111]. In this model, the new reaction class proposed by Ranzi et al. [283, 307] was considered. The predicted temperature orresponding to the maximum formation of dione was about 40 K lower than the experimental measurement (Fig. 37a). This work showed that the most recent models in the literature still do not satisfactorily predict dione formation. Some ambiguous issues must be resolved for the existing models to correctly predict the dione formation. Xing et al. [265] performed high level theoretical calculations of these H-abstractions from KHP in *n*-pentane oxidation, but they did not involve a comprehensive study on the modeling. In addition to the reaction channels mentioned above, two other channels have yet to be tested in combustion chemistry modeling:

- the decomposition of KHP to produce water and dione through a roaming reaction, proposed by West and Goldsmith [318],
- a chemically activated $\dot{Q}OOH + O_2$ reaction in parallel with the formation of KHP, suggested by Eskola et al. [260].

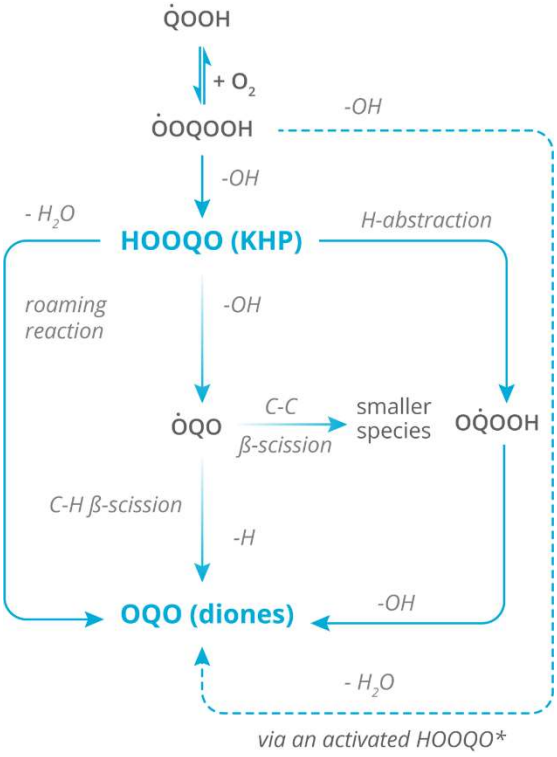

Figure 38: Summary of proposed reaction pathways for diones with carbon skeleton identical to fuel molecule. Dotted arrows correspond to pathways globalizing several elementary reactions.

In summary, the findings in Section 4.2 demonstrated that the degradation of KHPs does not occur only through cycle 2 of Fig. 1, via a rapid decomposition to yield ketoalkoxy and ȮH radicals. Even all the related channels are not yet fully understood; KHP decomposition can also be a source of C_1-C_2 carboxylic acids (Section 4.2.2). The Korcek mechanism described in Fig. 35 is a potential source for carboxylic acids. The competitive relationship between the KHP dissociation to ȮH radicals and the Korcek reaction of KHP must be thoroughly studied; however, there could be some additional channels that have not yet been identified.

Furthermore, diones with the same carbon skeleton as the fuel are important products of hydrocarbon oxidation (Fig. 37a). The pathways envisaged for dione formation are reviewed; and even though it is strongly suggested that diones come from the pathways following KHP consumption, the mechanism involved is still not well demonstrated and must be more thoroughly explored.

4.3 Kinetic modelling of third O_2 addition reactions

Another interesting topic is reaction kinetics for the third O_2 addition reactions. Because these pathways have only recently been proposed, reaction kinetics studies in the literature are very scarce. In this section, the few studies related to the third O_2 addition reactions are discussed, such as the alternative isomerization of the ȮOQOOH radical, model development for the third O_2 reactions and their effect on IDT and combustion phasing.

4.3.1 Alternative isomerization of the ȮOQOOH radical

As shown in Section 3.2.5, the third O_2 addition in fuel low-temperature oxidation leads to highly oxygenated intermediates with four and five oxygen atoms added to the fuel molecule. The prerequisite of this reaction mechanism is alternative isomerization of ȮOQOOH radicals. The reaction kinetics of this type of reaction has been investigated in recent years. Sharma et al. [104] studied the thermochemistry and rate constants of several selected ȮOQOOH radicals; special attention was paid to the hindered rotors of molecules with multiple internal rotors. Rate constants for the standard isomerization of ȮOQOOH to KHP were obtained and used in up-to-date Galway models [88, 109, 282]. For alternative isomerization pathways, the rate constants were not computed. Instead, they calculated the rate constants of ROȮ isomerizations, which could be used to estimate alternative isomerization rate constants. They mentioned that for some ȮOQOOH radicals, alternative isomerization is more important than standard isomerization. Two examples of the ȮOQOOH radicals, whose alternative isomerization is more important than the standard isomerization, are shown in Fig. 23.

Miyoshi et al. [105] carried out a comprehensive kinetic analysis of various kinds of ȮOQOOH radicals and suggested that the alternative isomerization rate constants of ȮOQOOH could be referred to analogous ROȮ radicals. The importance of the alternative isomerization was also highlighted by Goldsmith et al. [291] for ȮOQOOH radical in propane oxidation and by Sun et al. [319] for ȮOQOOH radical in *neo*-pentane oxidation. Recently, Yao et al. [320] studied site specific rate constants of some ȮOQOOH radicals; their study suggested that referring to the analogous ROȮ radicals may underestimate the alternative isomerization rate constants of ȮOQOOH radicals. Mohamed et al. [321, 322] systemically studied standard isomerizations and alternative isomerization of ȮOQOQH radicals in *n*-butane and *iso*-butane oxidation. The competitive relationship of these two reactions and the feasibility of referring ROȮ radicals to obtain the rate constants of ȮOQOOH alternative isomerization were discussed. Their results showed that the rate constant of ȮOQOOH alternative isomerization reactions are generally in good agreement with analogous ROȮ isomerization rates. The analogy is feasible for a few cases of ȮOQOOH alternative isomerization reactions; however, discrepancies were observed in some other cases. Similarly, Xing et al. [323, 324] investigated the competitive relationship of a class of

representative ȮOQOOH radicals which undergo the standard isomerization and alternative isomerization via the most favorable isomerization pathways by the six-member ring transition state. They concluded that torsional anharmonicity plays a significant role in the competition between the two isomerization pathways; and the size of the effect depends on the structure of the alkyl group, e.g. for ȮOQOOH radical like 3-peroxy-1-hexyl hydroperoxide and 3-peroxy-5-methyl-1-hexyl hydroperoxide, standard isomerization are the minor reactions over the investigated temperature range of 298−1500 K, and alternative isomerization reactions always dominate.

Supported by theoretical calculation, the alternative isomerization pathways of ȮOQOOH to $\dot{P}(OOH)_2$ radicals were included in the kinetic models of *n*-pentane [109, 111], *n*-hexane [282], *n*-heptane [88], and cyclohexane [325]. Rate constants for the alternative isomerization pathways in the three *n*-alkanes oxidation models were estimated by referring to analogous RO$\dot{O}$ isomerization rates [104]. In these models, the subsequent reactions of the $\dot{P}(OOH)_2$ radical included cyclization to form hydroperoxy cyclic ether, release of an ȮH radical, β-C-O scission to form olefinic hydroperoxide, release of an HO$\dot{O}$ radical (Fig. 23) and dissociation into smaller intermediates.

The change of ignition delay time (IDT) was observed after including these alternative isomerization pathways of ȮOQOOH and the subsequent reactions of $\dot{P}(OOH)_2$ radicals. The effect depended on the models, the fuel types and the temperature range [109, 112, 282].

One missing pathway from the $\dot{P}(OOH)_2$ radicals in these models is the O_2 addition to the radical site (e.g., a third O_2 addition). This additional reaction network needs to be developed and its effect on the combustion process needs to be explored.

4.3.2 Reaction rates and ideal reactor simulations

To complete the reaction mechanism and explore the effect of the third O_2 addition process on the ignition properties, a reaction mechanism of the third O_2 addition process (Fig. 26), was proposed by Wang et al. [112, 252]. The reaction pathways and the rate parameter sources for the third O_2 addition reaction in 2-methylhexane oxidation are shown in Table 9. The rate constants for those new added reactions were estimated from analogous reactions such as those of Q̇OOH, ȮOQOOH, and KHP. To maintain the consistency of the thermodynamic data, the group additivity method with the same sources of group values was used to estimate the thermodynamic properties of these species [281].

The kinetic model was used to simulate the JSR oxidation of 2-methylhexane [252], during which the signal profiles of the species generated from the third O_2 addition process (e.g., $C_7H_{12}O_4$ and $C_7H_{14}O_5$) were measured. Given the challenges outlined in Section 3.1.2 regarding the quantification of the mass spectral signal of elusive intermediates, a quantification of the signal is not currently feasible and only the profile shapes can be compared. The model captures well the signal profiles of the $C_7H_{12}O_4$ and $C_7H_{14}O_5$ species in Fig. 39, further confirming the existence of these highly oxygenated intermediates in combustion.

Table 9: Rate rules utilized for third O_2 addition reaction mechanism in 2-methylhexane oxidation [252].

Reactions	Reaction type	Analogous Reaction
O_2+ $\dot{P}(OOH)_2 \rightleftarrows \dot{O}OP(OOH)_2$	O_2 addition	O_2+ $\dot{Q}OOH \rightleftarrows \dot{O}OQOOH$
$\dot{O}OP(OOH)_2 \rightleftarrows ODHP+H\dot{O}$	Concerted elimination	$\dot{O}OQOOH \rightleftarrows OHP+H\dot{O}$
$\dot{O}OP(OOH)_2 \rightleftarrows KDHP+\dot{O}H$	H-migration, β-scission	$\dot{O}OQOOH \rightleftarrows KHP+\dot{O}H$
$\dot{O}OP(OOH)_2 \rightleftarrows \dot{T}(OOH)_3$	H-migration	$\dot{O}OQOOH \rightleftarrows \dot{P}(OOH)_2$
$\dot{T}(OOH)_3 \rightleftarrows DHPCE+OH$	Cyclization	$\dot{P}(OOH)_2 \rightleftarrows HPCE+\dot{O}H$
$\dot{T}(OOH)_3 \rightleftarrows ODHP+H\dot{O}$	C-O β-scission	$\dot{P}(OOH)_2 \rightleftarrows OHP+H\dot{O}$
$KDHP+\dot{O}H \rightleftarrows H_2O+\dot{O}H+$ DKHP	H-abstraction, β-scission	KHP + $\dot{O}H \rightleftarrows H_2O+\dot{O}H+$DKET
$DHPCE+\dot{O}H \rightleftarrows H_2O+\dot{O}H+KHPCE$	H-abstraction, β-scission	KHP + $\dot{O}H \rightleftarrows H_2O+\dot{O}H+$DKET
ODHP, KDHP, DHPCE, DKHP, and KHPCE decomposition	-OOH dissociation	KHP ⇄ products

Note: DHPCE: dihydroperoxy cyclic ether; KHPCE: ketohydroperoxy cyclic ether.

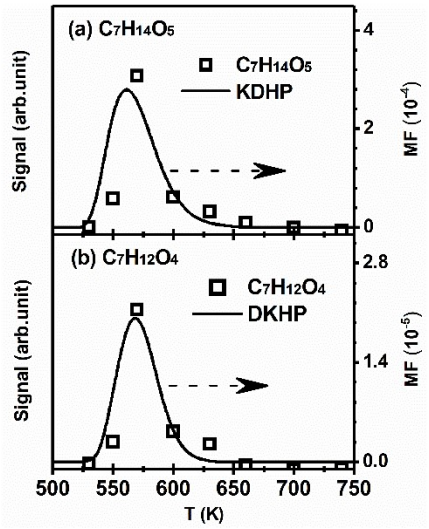

Figure 39: Temperature-dependent profiles of $C_7H_{14}O_5$ and $C_7H_{12}O_4$ intermediates in 2-methylhexane low-temperature oxidation. Symbols are experimental measurements; lines are simulated mole fractions of KDHP ($C_7H_{14}O_5$) and DKHP ($C_7H_{12}O_4$). Mole fractions refer to all isomers. Experimental signal and model prediction are scaled to match - adapted from Ref. [252].

A similar methodology was used to complete the reaction kinetic model of *n*-hexane low temperature oxidation, recently updated by Wang et al. [326]. In the update, 70 species and 151 reactions were added after including the third O_2 reactions in the *n*-hexane kinetic model, which originally had 1118 reactions and 4808 reactions; these numbers are expected to increase greatly when the represented fuel molecules in jet and diesel fuels are considered.

The effect of the third O_2 addition reactions on the IDTs of *n*-hexane and combustion phasing in HCCI *n*-hexane combustion was also investigated [326]. Figure 40(a) presents the IDTs of *n*-hexane in a shock tube and a rapid compression machine (RCM). Pressure is 1.52 MPa, equivalence ratio is 1.0, symbols are experimental measurements, dashed lines are model simulation by Zhang et al. [282]. The model captured the IDT of *n*-hexane under shock tube conditions (temperature 746 to 1370 K) well. However, the predicted first stage IDTs were higher than the experimental measurements at lower temperatures (e.g., 627-672 K) in RCM conditions. This discrepancy was reduced when the third O_2 addition reaction pathways were included in the model (represented by the black line in Fig. 40(a)). Results also revealed that promotion of IDT

by the third O_2 addition reactions depends on temperature, which determines the equilibrium of the third O_2 addition pathway. High temperature (the temperature under the aforementioned shock tube conditions) inhibited the third O_2 addition and resulted in a negligible effect on the IDT.

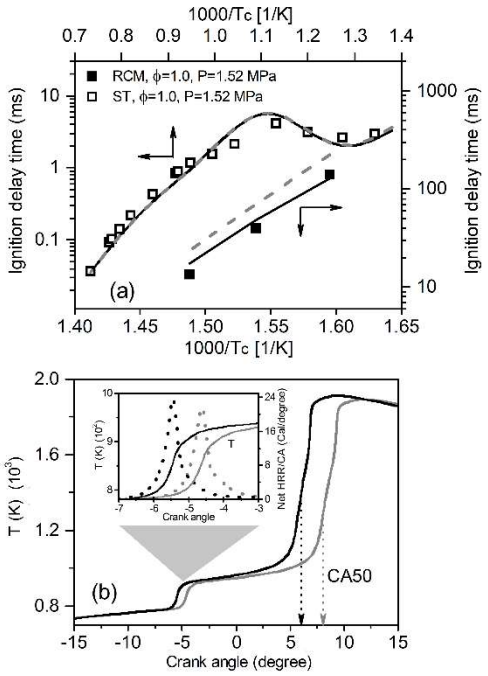

Figure 40: Effect of third O_2 addition reactions on IDTs and combustion phasing of *n*-hexane: (a) Shock tube (top-left axes), rapid compression machine (bottom-right axes) IDTs of *n*-hexane/air mixtures. Symbols are experimental data by Zhang et al. [282]. Black solid lines and grey dashed lines are simulation with [326] and without [282] third O_2 addition reactions. (b) Temperature dependence with crank angle during *n*-hexane/air mixtures in an HCCI engine ignition. Black and grey lines are simulation by model with and without third O_2 addition reactions, respectively. Net heat release rate (HRR) per crank angle and zoomed temperature profiles shown in inset – reproduced from Ref. [326] with permission from Elsevier.

A further study by Wang et al. [326] explored the effect of the third O_2 addition reactions on the combustion phasing in *n*-hexane HCCI combustion. The input parameters for the simulations were intake pressure 101.3 kPa, temperature 336 K, and equivalence ratio 0.4. The temperature profile as a function of crank angle in the cylinder (one crank angle degree corresponds to a time delay of 0.1 ms) is presented in Fig. 40(b). The grey line is the simulation by the original model of Zhang et al. [282]; the black line is simulated results after adding the third O_2 addition reaction scheme. Although both temperature profiles show two-stage ignition of *n*-hexane, the simulated CA 50 (the crank angle corresponding to 50% of total heat release) by the model with third O_2 addition reactions is ~2 degree earlier than the simulation using the original model. This slight advancement is also indicated by the earlier production of OH radicals (inset in Fig. 40(b)) by the model including the third O_2 addition pathways.

4.3.3 Implication for the modelling of real world systems

The simulation displayed in Fig. 40 shows that the third O_2 addition reactions promoted the ignition process in both constant volume and compression ignition of HCCI. Therefore, the question is how the third O_2 addition reaction promoted the ignition process. The brute force sensitivity analysis by Wang et al. [326] shows that the O_2 addition to $\dot{P}(OOH)_2$ radicals and the decomposition of the O_5 intermediates (e.g., KDHP) have a significant effect on the ignition of *n*-hexane. Later, Tingas et al. [327] used the computational singular perturbation (CSP) approach to explore the reaction dynamics of *n*-hexane ignition. In their work, two models of *n*-hexane, with and without the third O_2 addition reaction mechanism [282, 326], were adopted to simulate the ignition behavior of *n*-hexane under constant volume (closed batch reactor model) and variable volume (adiabatic single-zone HCCI engine model).

In the constant volume, the IDT of *n*-hexane at initial pressure of 6.08 MPa, initial temperature of 600 K, and equivalence ratio of 1.0 was simulated. Only the first stage ignition was observed in this simulation. Figure 41a presents the evolution of the fast explosive time scale τ_i in the two *n*-hexane models. In the context of CSP, the time scale of a mode sets the time frame of the action in this particular mode. As such, the characteristic mode has a time scale which will be among the fastest of the slow time scales. In autoignition systems, the fast explosive time scale τ_i is typically the characteristic time scale, characterizing the dynamics of the entire system [328]. Therefore, the fast explosive time scale is directly related to the ignition delay time (IDT) and the reactions composing the fast explosive time scale have a significant effect on the temporal evolution of the system. The time dependence of the important species controlling the ignition process --such as $\dot{O}H$, $H\dot{O}O$, and H_2O_2-- is also shown in Fig. 41b. The results show that during the explosive stage, the *n*-hexane model with third O_2 reactions had smaller τ_i, leading to a shorter IDT t in Fig. 41a. The promotion of ignition by the third O_2 reactions was also indicated by the buildup of the mass fractions of $\dot{O}H$, $H\dot{O}O$, and H_2O_2 species (yi in Fig. 41b).

To thoroughly explore the role of each elementary reaction in the explosive stage, the three points of the ignition process, P1, P2 and P3 in Fig. 41, were selected. The first point, P1, is at t = 0 s, corresponding to radical species production at the initial stage. P2 and P3 are at t = t/3 and t = 2t/3, respectively; they are the times when the growth of the radical pool is in its exponential phase. The quantification contribution of the reaction groups (first O_2 addition, isomerization of $\dot{Q}OOH$, O_2 addition to $\dot{P}(OOH)_2$, …) to the τ_i was analyzed. The results revealed that the following three types of reactions (only included in the *n*-hexane model with the third O_2 addition pathways), contribute to radical chain branching and promote the explosive nature of *n*-hexane ignition.

R1 KDHP ⇄ products + $\dot{O}H$
R2 $\dot{O}OP(OOH)_2$ ⇄ KDHP + $\dot{O}H$
R3 O2 + $\dot{P}(OOH)_2$ ⇄ $\dot{O}OP(OOH)_2$

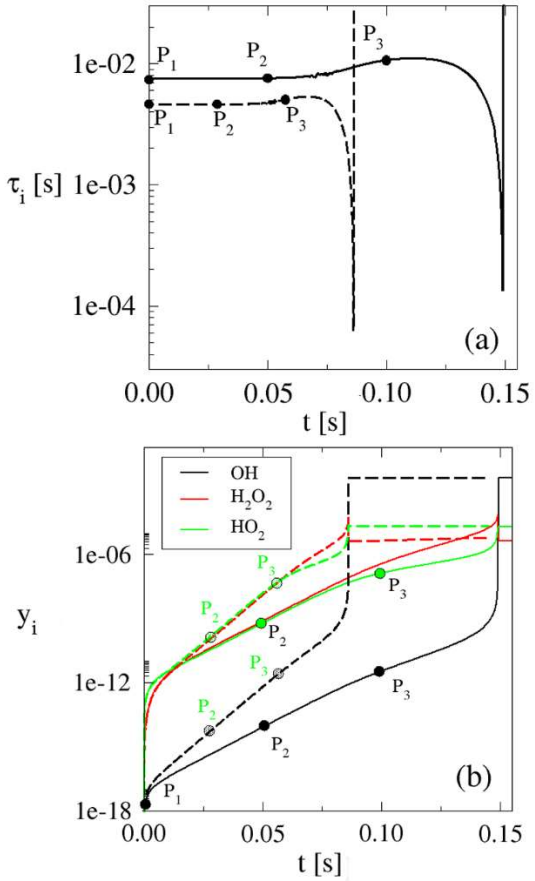

Figure 41: Evolution of explosive time scales (a), and mass fraction of OH, HO_2, and H_2O_2 (b) as a function of IDT during ignition of two *n*-hexane models. Conditions for simulation are p(0) = 6.08 MPa, ϕ = 1 and T(0) = 600 K. Dashed and solid lines are simulation results of *n*-hexane model with and without third O_2 addition reactions. P1 to P3 indicate the points at which CSP diagnostics were computed - adapted from the results of Ref. [327]. x-axis is physical time of ignition process (t). y-axis in (a) represents time scale τ_i [s] of 2 CSP fast explosive time scales. Y-axis in (b) represents mass fractions

Among them, the decomposition of KDHP is the dominant reaction in decreasing the IDT. A similar conclusion was obtained during the ignition process under HCCI conditions, which resulted in two-stage ignition of *n*-hexane. However, the role of the third O_2 addition reaction in this process decayed with time and the promotion of IDT became negligible at the end of the first stage ignition.

The kinetic modeling and CSP analysis showed that R1-R3, the third O_2 addition reaction pathway, generated additional radical chain-branching intermediates of KDHP. The bond dissociation of the OOH groups of KDHP produced extra ȮH radicals that may have extended ignition limits in certain combustion environments. This newly explored third O_2 addition reaction may advance the ignition process at high pressures and offer better prediction of the IDT of long chain alkanes [329].

To summarize Section 4.3, it is now well-accepted that ȮOQOOH radicals not only lead to KHP but can also isomerize to a wide range of $\dot{P}(OOH)_2$ radicals. Such alternative isomerization can be important, especially when yielding tertiary radicals (Fig. 23). These $\dot{P}(OOH)_2$ radicals are

candidates for a third O_2 addition reaction and are a source of compounds with four or five oxygen atoms added to the same skeleton as the fuel molecule (Fig. 26). This section shows that these pathways, postulated to follow the third O_2 addition in an oxidation model, changed the prediction of IDTs in RCM or in an HCCI engine. However, kinetic data for these reactions is still very scarce. More thorough studies for reaction kinetics of the typical structure of intermediates are needed. More investigations are needed to better understand the conditions in which this refinement may be fully necessary, consideration of these new pathways will involve significant enlargement of the models.

Mapping the initial conditions that revealed the effect of third O_2 addition reactions on the IDT was performed by Wang et al. [172] using the modeling of *n*-heptane as a prototype. Results from Fig. 42 reveal that (i) the effect of third O_2 addition pathways on the IDT was more evident at lower temperatures; (ii) the effect of third O_2 addition pathways on the IDT was more apparent at higher pressures; and correspondingly, the ratio of KDHP to KHP species was higher at higher pressures. For example, a reduction of about 20% in the ignition delay time was noted at 100 kPa, and 60% at 5 MPa, at a temperature of 600 K [172]. Additional simulations showed that the third O_2 addition reaction had a greater effect on the IDT under fuel-lean conditions than under fuel rich conditions. Similar conclusions were also obtained by Tingas et al. [327].

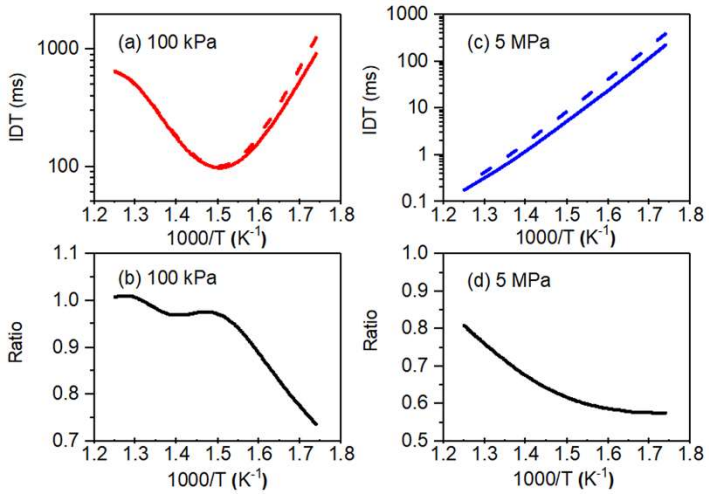

Figure 42: IDTs for *n*-heptane/O_2/N_2 mixtures at ϕ = 0.5. (a) Red dashed and red solid lines indicate IDTs obtained by simulation without third O_2 addition reactions and simulation with third O_2 addition reactions at 100 kPa, respectively; (b) ratio of IDT with third O_2 addition reactions to IDT without third O_2 addition reactions at 100 kPa. (c) Blue dashed and blue solid lines indicate IDTs obtained by simulation without third O_2 addition reactions and simulation with third O_2 addition reactions at 5 MPa, respectively; (d) ratio of IDT with third O_2 addition reactions to IDT without third O_2 addition reactions at 5 MPa – reproduced from Ref. [172] with permission of PNAS.

Moreover, the desired kinetic studies are hampered by the difficulty in detecting these elusive intermediates. So far, only molecular-beam mass spectrometry experiments with soft-ionization through synchrotron-generated vacuum-ultraviolet photons have allowed for the detection of these highly oxygenated species. Furthermore, strategies for quantitative measurements are lacking, significantly hampering progress. On the theoretical side, progress toward a complete

understanding of the intermediates involved in this newly detected reaction scheme is precluded because the size of the molecular structures, containing a large number of heavy atoms (C and O), increase computing time while simultaneously lowering the accuracy of the calculations [330].

5 CONCLUSION AND PERSPECTIVES

In this section, major conclusions from the recent development of experimental methods and progress in understanding hydroperoxide chemistry are summarized. Perspectives concerning hydroperoxide studies in combustion and atmospheric environment are also discussed.

(1) Development of transformative experimental methods

The results presented in this paper have developed mainly from studies of the low-temperature fuel oxidation in a JSR, which was coupled to two types of analytical diagnostics, i.e., continuous wave cavity ring-down spectroscopy (cw-CRDS) and photoionization mass-spectroscopy (PI-MS). The advantages and disadvantages of these two diagnostics for the analysis of hydroperoxides and other intermediates are presented in Table 10.

As can be seen from this summary and the discussion in this review, CRDS has been established as a sensitive technique to detect H_2O_2 and other labile species such as HOȮ radicals in combustion studies. In this method, the spectroscopic data of the target intermediate must be known in advance and interferences from other intermediates considered, limiting this technique to small molecules and radicals. Furthermore, due to condensation problems in the low pressure spectroscopic cell at ambient temperature, currently the method is also limited to analysis of the intermediates in the JSR oxidation of heavy fuels, up to *n*-heptane and hexanal (Section 3.2.1). However, the range of species probed by CRDS can certainly be enlarged. For example, the absolute cross-section of HONO, a potentially important intermediate in fuel oxidation in the presence of NO_x [331], was measured by CRDS in the near-infrared region [212].

Mass spectrometry techniques allow detection of intermediates without prior knowledge of their identity, permitting detection of large and/or complex species. Condensation is normally not a problem, especially using molecular-beam sampling. Using this method, JSR oxidation studies for fuels up to methyl decanoate have been reported. The SVUV-PIMS method has already been used to probe the product from the thermal degradation of notably heavier fuels, such as biomass pyrolysis [332-334]. JSR sampling molecular-beam mass spectrometry has also been used to investigate the ozonolysis process of biogenic emissions [48] that produces complex species within the pool of oxygenated intermediates [62]. cw-CRDS and mass spectrometry benefit from probe sampling (e.g., molecular beam and sonic probe), enabling sufficient cooling of the reactants and intermediates. Unfortunately, both techniques currently exhibit limitations when exploring the structures of more complex intermediates.

Table 10: Comparison of two main analytical techniques used to detect hydroperoxides. Details in Section 3.1.

Parameters	**Analytical techniques**	
	CRDS	**SVUV-PIMS**
Detected species	Quantified species must absorb in the used laser wavelength range.	All species can be detected simultaneously without prior knowledge of the chemical structure.
Labile species detection	Depends on coupling method: sonic probe and/or sampling cone enables H_2O_2 detection	Labile species can be detected in molecular beam experiments.
Sampling method	Sonic probe or sampling cone beam required to maintain cell at low pressure, usually < 6.7 kPa.	Sampling through small orifice and expansion into a molecular beam have been implemented.
Detection limit	Depends on species, spectra density, and absorption cross-section for combustion experiments. Limit is typically 50 ppm.	Detection limits depends on the species ionization cross-sections and other parameters. Typically, the limit is ~ 1ppm.
Uncertainty	~30%. Depends on uncertainty of cross-sections and peak environment: some spectra are very loaded. Several peaks can be used for quantification of the same species (and to confirm identification)	For species with known photoionization cross-sections, uncertainties of ~25% are typical and can be larger when ionization cross-sections are calculated or estimated.
Calibration	May not be required if absorption cross-sections measured elsewhere. Correction needed to account for pressure effect on peak height, if peak height is used instead of peak area for quantification.	Extensive calibration of the mass spectrometer is necessary (MDFs, etc.). Furthermore, photoionization cross-sections need to be known.
Analysis time	Depends on wavelength range and mirror alignment (typical time: 30-60 min. to scan over 5 cm^{-1})	A simple mass spectrum can be accumulated in about two minutes with sufficient signal to noise (S/N) ratio. Several mass spectra at different photon energies are necessary at any given temperature for a complete analysis.
Limitations/Difficulties	Due to condensation/adsorption problems, CRDS are not fully adapted to analyze intermediates for large fuel (e.g., *n*-decane) oxidation. Mirror cleaning frequently required, especially for combustion experiments.	Species identification and quantification nearly impossible for large molecules. Interpretation of mass spectra becomes complex.

Operating conditions using these two diagnostic techniques could be expanded. At present, all the JSR oxidation studies using CRDS or photoionization mass-spectrometry have been carried out at around 100 kPa; these methods must be adapted to study the reaction process at pressures more relevant to engine combustion [330] (up to 6 MPa for diesel engines [86], up to 12 MPa for HCCI engines [85]). A JSR with a sampling probe has already been used at pressures up to 4 MPa [166], together with the conventional analytical methods of GC and FTIR. One perspective could be the coupling of high pressure JSRs (for example up to 1 MPa), using cw-CRDS cell, or with PIMS. A high pressure flow reactor, working at pressures up to 200 kPa, has already been coupled to a molecular-beam mass spectrometer [158]. Sampling was achieved with an orifice positioned at the center of the end wall of the reactor. A solution by which to sample the reactor at atmospheric

pressure could be the use of a sampling cone, proven to work for atmospheric pressure sampling, and challenging at high pressure for two main reasons. 1) The cone, usually made of fused silica to avoid wall reactions, should resist the large difference in pressure ($\Delta P \approx 1.1$ MPa for a 1 MPa inside the reactor). The use of a cone made of metal (and preferably coated with non-reactive materials), could overcome this problem, but wall reactions may still occur. The use of a thick fused silica cone would be preferable, if possible. 2) The difference in pressure between the reactor and the analytical device should be preserved. One solution would be to control the size of the hole at the tip of the sampling cone; this may not be a universal solution since sampling cone holes are usually hand made. Laser or ultrasonic drilling can help solve this issue. For the PIMS, another solution would be faster pumping between the sampling cone and the skimmer, an additional stage between the sampling cone and the skimmer. For cw-CRDS, the use of a fused silica capillary tube is an option. However, this solution does not work for the sampling of reactive species like radicals.

While current techniques to detect and identify hydroperoxide species in complex environments have been proven to be very successful, some limitations remain:

- Small Franck-Condon overlaps may preclude the sensitive detection of these important intermediates;
- Species, and specifically isomeric identification based on the PIE curve, appear to be unreliable and/or achievable without theoretical support, which can be difficult when the size of the fuel molecule increases;
- Dissociative ionization might preclude a complete qualitative/quantitative interpretation of the sampled mass spectra;
- Access to synchrotron radiation facilities is highly competitive and therefore limited.

To overcome some of these challenges, new diagnostic techniques that address at least one of the above issues, must be developed. For example, photoelectron-photoion-coincidence (PEPICO) mass spectrometry might become a useful tool for the advanced diagnostics of hydroperoxides in low-temperature oxidation environments [335, 336]. In this technique, which also relies on the soft ionization, not only the photoion is detected (as in regular mass spectrometry), but the ejected photoelectron is also detected in coincidence. The energy of the ejected electron and the related photoelectron spectra can be used for isomer-resolved detection. While it is possible to perform PEPICO experiments in the laboratory using lasers, two VUV beamlines at SOLEIL, France and PSI, Switzerland mastered this technique and offer a great advantage in photon flux and duty cycle compared to laboratory experiments [189, 190, 337]. Flame-sampling experiments have proved that PEPICO can be used as an isomer-resolving diagnostic technique for complex environments [189-193, 338, 339]. An example is shown in Fig. 43, in which Pieper et al. [193] used PEPICO to identify the isomers at m/z = 68 from a fuel-rich *iso*-pentane flame. It shows how the two-dimensional image of the electrons that correlate to m/z = 68 ions (Fig. 43a) is converted into the photoelectron spectra (Fig.43b) and how this is fitted to reference spectra of the four m/z = 68 isomers 1,3-pentadiene, isoprene, cyclopentene, and 1,4-pentadiene.

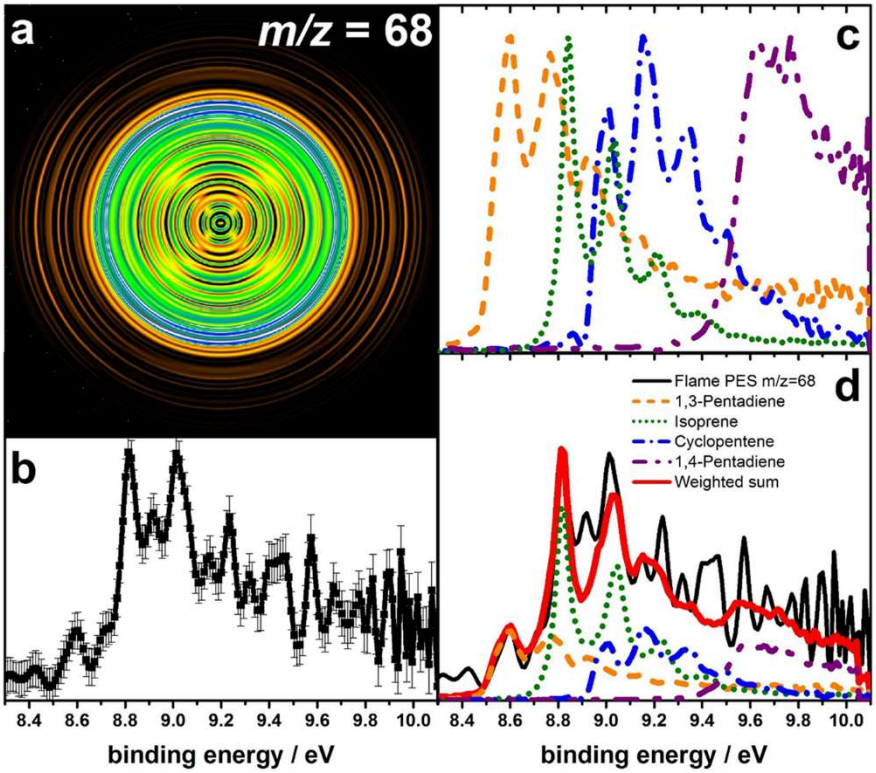

Figure 43: Results obtained using PEPICO mass spectrometry in a fuel-rich *iso*-pentane flame at 3.2 mm above burner surface and a fixed photon energy of 10.1 eV. (a) Inverted twodimensional electron image corresponding to ions of m/z = 68. (b) Photoelectron spectrum of m/z = 68. (c) Normalized reference spectra of m/z = 68. (d) Comparison of measured photoelectron spectrum with weighted sum of all reference spectra (binding energy = photon energy - kinetic energy) – Reproduced from Ref. [193] with permission of De Gruyter.

The photoelectron spectra are likely to be unknown for the hydroperoxides examined in this review. For identification purposes with PEPICO, and as with SVUV-PIMS, results must be combined with theoretical calculations of the ionization and binding energies. Non-synchrotron-based mass-spectrometric diagnostic techniques already implemented in the laboratories include laser-based techniques with four-wave mixing and atmospheric-pressure chemical ionization (APCI) mass spectrometer using nitrate (NO_3^-), sulfate (SO_4^{2-}), lactate ($CH_3CH(OH)COO-$), pyruvate ($CH_3C(O)COO-$) and acetate (CH_3COO-) clustering to form negative ions, or proton transfer techniques, to produce positive ions [340]. The clustering technique is highly sensitive to molecules containing -OH and -OOH groups, and it could be used to identify functional groups [25]. These advanced diagnostic techniques typically come with a high resolution mass spectrometer that allows exact determination of the molecular formula. However, issues remain concerning the quantification of the signal, i.e., the conversion of the mass spectra into mole fraction profiles. A more advanced diagnostic technique, called tandem or two-dimensional mass spectrometry, deserves to be tested for the study of the peroxide chemistry. This technique should chiefly offer the possibility of clarifying the chemical structure of sampled molecules [341, 342]. In this technique, currently being developed for flame-sampling experiments [194], ions are created using a soft ionization technique and mass is selected using a quadrupole mass filter. These mass selected ions are fragmented in a process called collision-induced fragmentation [343, 344]. The created fragment ions are then mass selected with a second mass spectrometer; the observed

fragmentation pattern is expected to provide structural information, possibly overcoming the challenges in identifying molecular structures using current experimental techniques [341, 342]. Although the fragmentation pattern of the hydroperoxide species might be useful when identifying molecular structures, in a totally different approach, rotational spectroscopy might be developed into a tool that enables unique identification capabilities. Rotational spectroscopy, also known as microwave spectroscopy, measures the frequency of the transitions between rotational states of freely rotating, polar molecules in the gas phase [345]. Microwave spectroscopy is known to provide the most accurate molecular structures; it is not only sensitive to isomeric, but also to conformeric structures [345, 346]; and it is based on the fact that the quantized rotational states of individual molecules depend on the moment of inertia, and therefore, the molecular structure. The invention of chirped-pulse microwave spectroscopy, in particular, has overcome some inherent problems, such as narrow band resonator style experiments that precluded easy detection of overview spectra and quantification [347].

Worldwide efforts are being undertaken to establish chirped-pulse microwave spectroscopy as an analytical tool in physical chemistry problems [346, 348, 349]. Microwave spectroscopy is typically conducted in pulsed molecular-beam experiments that result in rotational temperatures in the molecular beam of less than 5 K. Such rotationally cold molecules are needed to increase the sensitivity of this technique, which is dependent on the population differences between the different rotational states. This might hamper the technique for applicability in the study of peroxide chemistry in complex environments, but Hansen et al. [350] recently showed that low rotational temperatures can be achieved after sampling from hot flame environments, allowing the detection of oxygenated species in laboratory flames. Their experimental set-up, and a typical rotational spectrum after flame-sampling, are shown in Fig. 44.

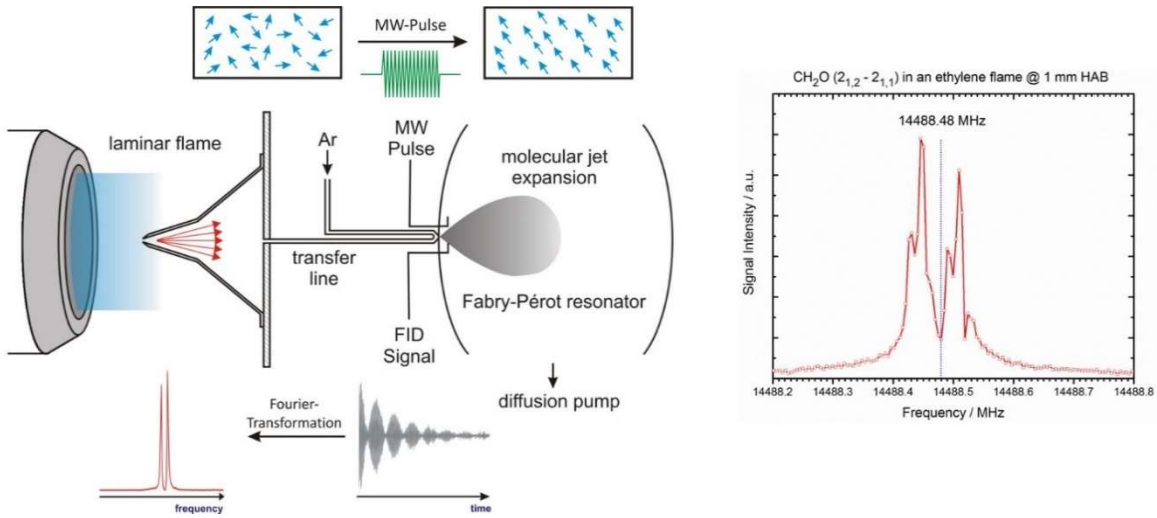

Figure 44: Experimental set-up by Hansen et al. [350] to achieve rotational temperatures of ~10 K after sampling from hot combustion environments. Model includes two-stage sampling through a quartz probe and molecular beam expansion into the high vacuum of a Fabry-Pérot type resonator. After excitation of rotating molecules with a short microwave pulse, free induction decay is detected and Fourier transformation results in the rotational spectrum. This extreme cooling allows sensitive detection of rotational transition of the 21,2-21,1 rotational transition of combustion intermediate formaldehyde.

The challenges arising with the interpretation of the microwave spectra from complex gas mixtures are complementary to those discussed above, which govern interpretation of the mass spectra. While mass spectrometry typically allows only for identification of mass-to-charge ratios, without providing detailed structural information, microwave spectroscopy has the potential to provide highly detailed structural information. Challenges may arise from assigning spectroscopic features to unknown chemical structures, from the complexity of the rotational spectra due to additional interactions of the rotational momentum with nuclear and electronic spins, and from different conformeric states of large flexible molecules. Furthermore, frequency ranges of the microwave components are limited, resulting in restrictions to accessible rotational transitions for targeted species in the given frequency range.

(2) Progress in understanding hydroperoxide chemistry

The work reviewed in this paper has shown abundant results in the detection/quantification of a wide range of reactive intermediates and their deriving species (acids and diones) obtained since 2010. Figure 45 summarizes the hydroperoxides, acid and diones that have been quantified during the oxidation of *n*-pentane using the two main experimental methods described here. The evolution of their mole fraction with temperature is displayed.

As is shown in Fig. 45a, acetic acid, pentadiones, and C_1-C_2 alkyl hydroperoxides were the major new products observed. Fig. 45b indicates that C_{3+} hydroperoxides are formed in much lower amounts than C_1 hydroperoxide. However, this figure does not reflect the reality for yields of KHPs, for which the mole fraction estimated using the group additivity method has been shown to be underestimated by a large factor, due to the disregard of significant fragmentation of this species. For these hydroperoxides in the temperature range of 500-700 K, the C_5 KHP and the C_5 alkyl hydroperoxide peak at the lowest temperature (next to peak are alkenyl and small alkyl hydroperoxides), while the hydrogen peroxide peaks at the highest temperature. The maximum mole fraction of acetic acid was observed at temperatures about 15 K lower than that of pentadiones.

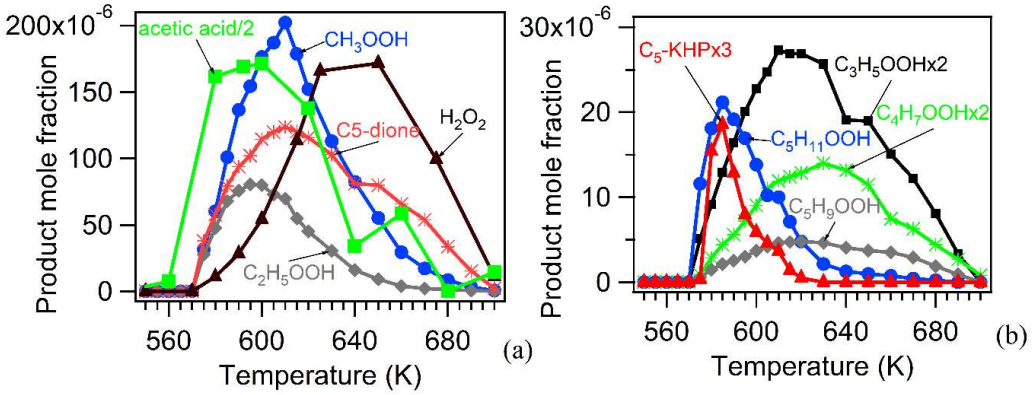

Figure 45: Mole fraction of hydroperoxides, acid and diones quantified using CRDS or photoionization mass spectrometry (with photoionization cross-section estimated by group additivity method) during *n*-pentane JSR oxidation under conditions in Figs. 4, 14, and 37a – adapted from results in Ref. [111, 171].

In comparison to Fig. 1, Fig. 46 shows the significant improvement in understanding reaction pathways during alkane low-temperature oxidation since 2010. This low-temperature oxidation mechanism is also important in microgravity cool flame formation of fuel droplets [229, 351] and in the oxidative stability of lubricants and other industrial fluids [80].

The improvements include several aspects. First, in addition to the formation of the many normal oxidation products (cyclic ethers, aldehydes, and ketones), two new types of intermediates must be considered: carboxylic acids (e.g., C1-C2) and diones with two carbonyl groups. As shown in Fig. 45, these products are formed in impressive amounts.

Second, alkyl and ketohydroperoxides are not the only organic hydroperoxides that must be considered. As previously demonstrated, pathways leading to olefinic hydroperoxides (OHP in Fig. 46) should also be taken into account.

Last, is a third propagating cycle (cycle 3 in Fig. 46) that includes a branching channel derived from a third O_2 addition pathway which has been proven feasible. This pathway is a source of hydroperoxides, with five O-atoms added to the fuel molecule, such as ketodihydroperoxides (KDHP). A slight promotion of IDTs by this new cycle has been reported at low temperatures. The third O_2 addition pathway is also a potential source of hydroperoxides with four O-atoms added to the fuel molecule, such as olefinic dihydroperoxides (ODHP), or di-ketohydroperoxides (DKHP, not shown in Fig. 46). For these newly proposed reaction pathways, more kinetic investigations are necessary to fully identify the involved channels and their rate parameters --necessary for the evaluation of their roles in the ignition process.

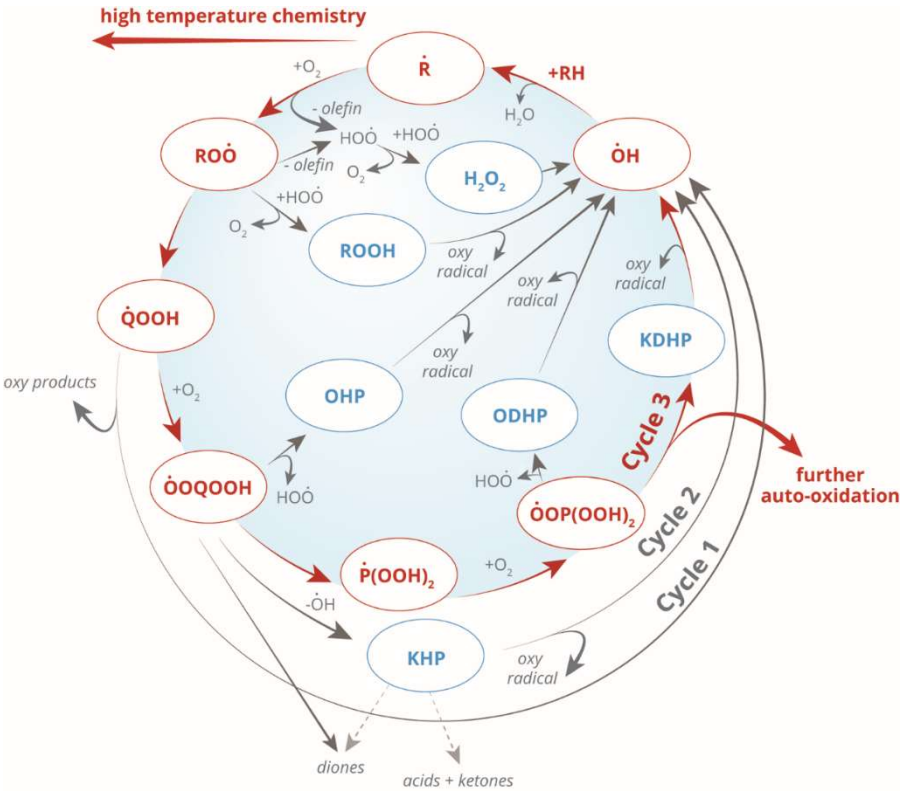

Figure 46: Updated reaction scheme for alkane low-temperature oxidation.

The key reaction that determines the first stage ignition in the reaction scheme is the decomposition of KHPs. The reaction kinetics related to these intermediates are the basis for complete exploration of the Korcek reaction to organic acids, the dione formation from KHPs, and the importance of the third O_2 addition pathways on the ignition process. Currently, studies on the reaction kinetics of hydroperoxide --especially of KHPs-- are scarce, both experimentally and theoretically. From the experimental side, collaboration with organic chemists to synthetize the hydroperoxides (ketohydroperoxides and other hydroperoxides) would aid in the study of reaction kinetics and the measurement of physical properties, like photoelectron and photoionization efficiency spectra. This type of experimentation is challenging because these hydroperoxides can violently dissociate. For the theoretical investigation, the only study in the literature is on the γ-KHP reaction in propane oxidation [291, 292]. Considering the complexity of the fuel structures (linear, branched, cyclic, and oxygenated), the large number of possible KHP isomers, and the competition of unimolecular and bimolecular reactions, the systemic and comprehensive investigation of reaction kinetics of KHPs is certainly necessary. A recent study by Grambow et al. [314], showed that the unimolecular reaction pathways of the simplest γ-KHP, 3-hydroperoxypropanal, are much more complex than expected. The authors discovered 68 reactions that were previously unknown and completely unexpected for this KHP. The importance of these newly discovered reactions must still be proven.

The proposition of the third O_2 addition pathways creates new research avenues for autoignition and hydroperoxide chemistry. The questions are whether further O_2 addition (fourth and fifth O_2 additions [172]) could occur; what is the appropriate environment for the further O_2 addition, how can we observe them, and how would they affect our understanding of autoignition and atmospheric chemistry? The highly oxygenated intermediates, with eleven O-atoms added to the reactant, were observed during the atmospheric auto-oxidation of aromatics [352], indicating a fifth O_2 addition reaction process. From the analysis of Wang et al. [172], the prerequisites for further O_2 addition, e.g., a fourth O_2 addition, are "(i) sufficient length of the carbon backbone, which allows multiple H-shift of the peroxy radical; (ii) functional groups such as tertiary C-H, naphthenic C-H, and oxygenated functions (e.g., carbonyl, keto, -OOH, -OH) which facilitate alternative isomerization; (iii) an adequate concentration of O_2 (e.g., pressure, fuel/O_2 ratio), which affects the rate of O_2 addition reaction (bimolecular reactions) and subsequent competition with bond-breaking via concerted H-transfer/beta-scission, which are favored at higher pressures and lower fuel/O_2 ratios; and (iv) an appropriate temperature for the oxidation reaction, which affects the equilibrium of the O_2 addition reaction (lower temperature favors O_2 addition reactions). "

It is expected that the concentration of hydroperoxide intermediates from the fourth and fifth O_2 addition is lower than those from the third O_2 addition. To capture these reactive intermediates, it is necessary to increase the detection limit of the SVUV-PIMS method. Furthermore, the atmospheric pressure chemical ionization (APCI) mass spectrometer, using nitrate (NO_3^-), sulfate (SO_4^{2-}), lactate ($CH_3CH(OH)COO-$), pyruvate ($CH_3C(O)COO-$) and acetate (CH_3COO-) clustering, is highly sensitive to molecules containing -OOH groups and could require a technique to explore autoignition and hydroperoxide chemistry.

Third O_2 addition pathways are also important for atmospheric auto-oxidation chemistry. The unburnt hydrocarbons (alkanes, cycloalkanes, and aromatics) and oxygenated compounds (aldehyde, keto compounds, and organic acids) from the internal combustion engines are important sources of pollutants in the urban area [353]. Their oxidation reaction by ȮH radical leads to radical intermediates; and the O_2 addition to the radical site forms peroxy radicals. Similar to low temperature oxidation in combustion environments (e.g., T > 500 K, at which organic compounds start to react by oxidation without photochemical initiation), peroxy radicals are also the center for the atmospheric auto-oxidation of organic compounds [13]. In the ozonolysis, or OH-radical initiated oxidation of unsaturated hydrocarbons, peroxy radicals undergo internal transfer of the weakly bound H atoms connected to the oxygenated functional groups (-OH and -C=O) and allylic sites, etc. However, for the peroxy radicals from saturated hydrocarbon auto-oxidation, the bimolecular reactions are usually more important [354, 355]. A recent study by Praske et al. revealed that the auto-oxidation of peroxy radicals from saturated hydrocarbons becomes increasingly important in urban and suburban North America [356]. In remote areas, as well as urban areas with decreasing NO_x emission due to the strict regulation from power generation and transportation, peroxy radicals might undergo auto-oxidation pathways that involve internal hydrogen migration and O_2 addition and produce hydroperoxide intermediates with multiple functional groups. This process should be more favorable for organic compounds with weak C-H bond (tertiary C-H, allylic C-H) and/or oxygenated functions. The higher temperature of summer afternoons and tropical areas should also favor the auto-oxidation process [356].

Furthermore, as highlighted in Fig. 47, it is necessary to establish an intelligent system of varieties and relative importance of the products generated by auto-oxidation processes. They might be emitted at the outlet of engines and interact with species from biogenic sources to form secondary organic aerosol (SOA), with significant implications for global climates [357]. This is particularly important for low-volatility organic compounds, like those containing several oxygen atoms, which can result from hydroperoxide or polyhydroperoxide decomposition and can be the starting nucleus for SOA. Moreover, the extremely low-volatility organic compounds (ELVOC), with a few functional groups added to the VOC reactants, can be generated from multigeneration oxidation of oxidation products and/or auto-oxidation of the organic peroxy radical from the initial VOC reactant [357]. Their extremely low vapor pressure could cause them to condense onto the growing particles in an irreversible process. Another important combustion source for organic aerosols is the burning of biomass. An important fraction of organic compounds from biomass burning is semi-volatility and intermediate-volatility organic compounds. Understanding of their emissions and their role in SOA production is still poor [358, 359], and the SOA from biomass burning is not well constrained in global climate models [360-362].

To this end, collaborations from combustion and atmosphere scientists could bridge the gap. For example, both the SVUV-PIMS method commonly used in combustion studies and the APCI mass spectrometer with clustering technique commonly adopted in the atmospheric research, could be used to investigate atmospheric auto-oxidation of hydrocarbons under well-defined laboratory reactors (FT and JSR). The combination of these two methods is expected to clarify the species pool with a wide range of volatility, and improve the identification of their probable structures.

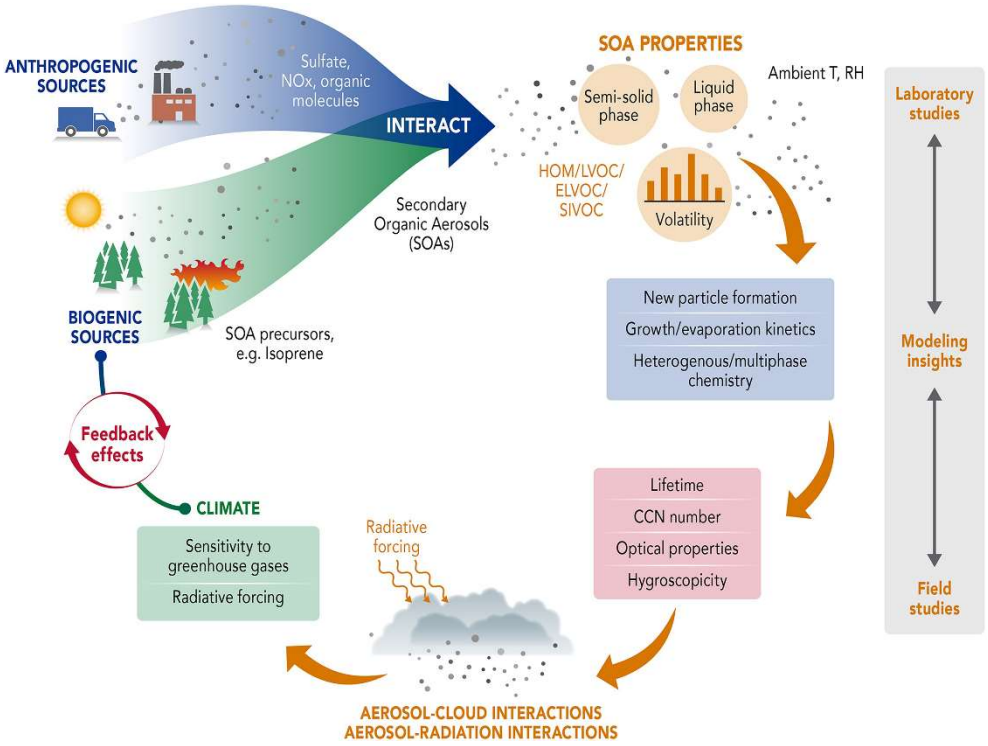

Figure 47: Formation of secondary organic aerosols and their importance in climate forcing: HOM: highly oxygenated molecules; LVOC: low-volatility organic compounds; ELVOC: extremely low-volatility organic compounds; SIVOC: semi-volatility and intermediate-volatility organic compounds; T: temperature; RH: relative humidity (only in this figure); CCN: cloud condensation nuclei – reproduced from Ref. [357] with permission of AGU.

The experience of scientists in combustion and atmospheric chemistry could be joined to improve detailed kinetic models and predict the atmospheric auto-oxidation process [363-365]. The ultimate goal is to develop combustion models that predict fuel ignition, flame propagation, and pollutant emissions, in cooperation with climate models that predict the chemical and dynamic evolution of SOA and global climate forcing.

ACKNOWLEDGEMENTS

ZW acknowledges “Hundred Talents Program” of the Chinese Academy of Sciences, and the Combustion and Flame endstation at National Synchrotron Radiation Laboratory. NH acknowledges support from the U.S. DOE, Office of Science, Office of Basic Energy Sciences. Sandia National Laboratories is a multi-mission laboratory managed and operated by National Technology and Engineering Solutions of Sandia, LLC., a wholly owned subsidiary of Honeywell International, Inc., for the U.S. DOE National Nuclear Security Administration under contract DE NA0003525. The authors thank Sandia artists Loren Stacks and Brent Hagelund for their help preparing some of the illustrations. We also wish to thank Michel Rossi, Charles Westbrook, Eliseo Ranzi, Christa Fittschen, Arkke Eskola, Stathis Tingas, Tao Tao, Luc Sy Tran, Gustavo Garcia Macias for their valuable assistance during the writing of this review.

PREFERENCES

[1] Luo YR. Comprehensive handbook of chemical bond energies: CRC Press. Taylor and Francis Group. Boca Raton; 2007.

[2] Jones CW. Applications of Hydrogen Peroxide and Derivatives: Royal Society of Chemistry; 2007.

[3] Pasini A, Torre L, Romeo L, Cervone A, D'Agostino L. Testing and Characterization of a Hydrogen Peroxide Monopropellant Thruster. J Propuls Pow. 2008;24:507-15.

[4] Rajakumar B, McCabe DC, Talukdar RK, Ravishankara AR. Rate coefficients for the reactions of OH with n-propanol and iso-propanol between 237 and 376 K. Int J Chem Kinet. 2010;42:1024.

[5] Sivaramakrishnan R, Srinivasan NK, Su MC, Michael JV. High temperature rate constants for OH + alkanes. Proc Combust Inst. 2009;32:107-14.

[6] Williams HR, Mosher HS. Peroxides. I. n-Alkyl Hydroperoxides. J Am Chem Soc. 1954;76:2984-7.

[7] Williams HR, Mosher HS. Organic Peroxides. II. Secondary Alkyl Hydroperoxides. J Am Chem Soc. 1954;76:2987-90.

[8] Lee M, Heikes BG, O'Sullivan DW. Hydrogen peroxide and organic hydroperoxide in the troposphere: a review. Atmos Environ. 2000;34:3475-94. [9] Zhou X, Lee YN. Aqueous solubility and reaction kinetics of hydroxymethyl hydroperoxide. J Phys Chem. 1992;96:265-72.

[10] Kok GL, McLaren SE, Stafflbach TA. HPLC Determination of Atmospheric Organic Hydroperoxides. J Atmos Ocean Tech. 1995;12:282-9.

[11] Kyasa S, Puffer BW, Dussault PH. Synthesis of Alkyl Hydroperoxides via Alkylation of gemDihydroperoxides. J Org Chem. 2013;78:3452-6.

[12] Vaghjiani GL, Ravishankara AR. Kinetics and mechanism of hydroxyl radical reaction with methyl hydroperoxide. J Phys Chem. 1989;93:1948-59.

[13] Crounse JD, Nielsen LB, Jørgensen S, Kjaergaard HG, Wennberg PO. Autoxidation of Organic Compounds in the Atmosphere. J Phys Chem Lett. 2013;4:3513-20.

[14] Hui S-P, Taguchi Y, Takeda S, Ohkawa F, Sakurai T, Yamaki S, et al. Quantitative determination of phosphatidylcholine hydroperoxides during copper oxidation of LDL and HDL by liquid chromatography/mass spectrometry. Anal Bioanal Chem. 2012;403:1831-40.

[15] Zhou S, Rivera-Rios JC, Keutsch FN, Abbatt JPD. Identification of organic hydroperoxides and peroxy acids using atmospheric pressure chemical ionization–tandem mass spectrometry (APCI-MS/MS): application to secondary organic aerosol. Atmos Meas Tech. 2018;11:3081-9.

[16] Hui S-P, Sakurai T, Ohkawa F, Furumaki H, Jin S, Fuda H, et al. Detection and characterization of cholesteryl ester hydroperoxides in oxidized LDL and oxidized HDL by use of an Orbitrap mass spectrometer. Anal Bioanal Chem. 2012;404:101-12.

[17] Lee JH, Leahy DF, Tang IN, Newman L. Measurement and speciation of gas phase peroxides in the atmosphere. J Geophys Res. 1993;98:2911-5.

[18] De Serves C. Gas phase formaldehyde and peroxide measurements in the Arctic atmosphere. J Geophys Res. 1994;99:25391-8.

[19] Sauer F, Beck J, Schuster G, Moortgat GK. Hydrogen peroxide, organic peroxides and organic acids in a forested area during FIELDVOC'94. Chemosphere - Global Change Sci. 2001;3:309-26.

[20] Guo J, Tilgner A, Yeung C, Wang Z, Louie PKK, Luk CWY, et al. Atmospheric Peroxides in a Polluted Subtropical Environment: Seasonal Variation, Sources and Sinks, and Importance of Heterogeneous Processes. Environ Sci Technol. 2014;48:1443-50.

[21] Wennberg PO, Hanisco TF, Jaeglé L, Jacob DJ, Hintsa EJ, Lanzendorf EJ, et al. Hydrogen Radicals, Nitrogen Radicals, and the Production of O3 in the Upper Troposphere. Science. 1998;279:49-53.
[22] Singh HB, Kanakidou M, Crutzen PJ, Jacob DJ. High concentrations and photochemical fate of oxygenated hydrocarbons in the global troposphere. Nature. 1995;378:50.
[23] Jackson AV, Hewitt CN. Atmosphere Hydrogen Peroxide and Organic Hydroperoxides: A Review. Crit Rev Environ Sci Technol. 1999;29:175-228.
[24] Tobias HJ, Ziemann PJ. Thermal Desorption Mass Spectrometric Analysis of Organic Aerosol Formed from Reactions of 1-Tetradecene and O3 in the Presence of Alcohols and Carboxylic Acids. Environ Sci Technol. 2000;34:2105-15.
[25] Ehn M, Thornton JA, Kleist E, Sipilä M, Junninen H, Pullinen I, et al. A large source of lowvolatility secondary organic aerosol. Nature. 2014;506:476.
[26] Krapf M, El Haddad I, Bruns Emily A, Molteni U, Daellenbach Kaspar R, Prévôt André SH, et al. Labile Peroxides in Secondary Organic Aerosol. Chem. 2016;1:603-16.
[27] Docherty KS, Wu W, Lim YB, Ziemann PJ. Contributions of Organic Peroxides to Secondary Aerosol Formed from Reactions of Monoterpenes with O3. Environ Sci Technol. 2005;39:404959.
[28] Li H, Chen Z, Huang L, Huang D. Organic peroxides' gas-particle partitioning and rapid heterogeneous decomposition on secondary organic aerosol. Atmos Chem Phys. 2016;16:1837-48.
[29] Atkinson R, Baulch DL, Cox RA, Hampson Jr. RF, Kerr JA, Troe J. Evaluated Kinetic and Photochemical Data for Atmospheric Chemistry: Supplement IV. IUPAC Subcommittee on Gas Kinetic Data Evaluation for Atmospheric Chemistry. J Phys Chem Ref Data. 1992;21:1125-568.
[30] Logan JA, Prather MJ, Wofsy SC, McElroy MB. Tropospheric chemistry: A global perspective. J Geophys Res. 1981;86:7210-54.
[31] Kleinman LI. Photochemical formation of peroxides in the boundary layer. J Geophys Res. 1986;91:10889-904.
[32] Kleinman LI. Seasonal dependence of boundary layer peroxide concentration: The low and high NOx regimes. J Geophys Res. 1991;96:20721-33.
[33] Olszyna KJ, Meagher JF, Bailey EM. Gas-phase, cloud and rain-water measurements of hydrogen peroxide at a high-elevation site. Atmos Environ. 1988;22:1699-706.
[34] Sakugawa H, Kaplan IR. H2O2 and O3 in the atmosphere of Los Angeles and its vicinity: Factors controlling their formation and their role as oxidants of SO2. J Geophys Res. 1989;94:12957-73.
[35] Das M, Aneja VP. Measurements and analysis of concentrations of gaseous hydrogen peroxide and related species in the rural Central Piedmont region of North Carolina. Atmos Environ. 1994;28:2473-83.
[36] Watkins BA, Parrish DD, Trainer M, Norton RB, Yee JE, Fehsenfeld FC, et al. Factors influencing the concentration of gas phase hydrogen peroxide during the summer at Niwot Ridge, Colorado. J Geophys Res. 1995;100:22831-40.
[37] Watkins BA, Parrish DD, Buhr S, Norton RB, Trainer M, Yee JE, et al. Factors influencing the concentration of gas phase hydrogen peroxide during the summer at Kinterbish, Alabama. J Geophys Res. 1995;100:22841-51.
[38] Gnauk T, Rolle W, Spindler G. Diurnal Variations of Atmospheric Hydrogen Peroxide Concentrations in Saxony (Germany). J Atmos Chem. 1997;27:79-103.

[39] Atkinson R, Baulch DL, Cox RA, Crowley JN, Hampson RF, Hynes RG, et al. Evaluated kinetic and photochemical data for atmospheric chemistry: Volume I - gas phase reactions of Ox, HOx, NOx and SOx species. Atmos Chem Phys. 2004;4:1461-738.
[40] Atkinson R, Baulch DL, Cox RA, Crowley JN, Hampson RF, Hynes RG, et al. Evaluated kinetic and photochemical data for atmospheric chemistry: Volume II - gas phase reactions of organic species. Atmos Chem Phys. 2006;6:3625-4055.
[41] Becker KH, Brockmann KJ, Bechara J. Production of hydrogen peroxide in forest air by reaction of ozone with terpenes. Nature. 1990;346:256-8.
[42] Becker KH, Bechara J, Brockmann KJ. Studies on the formation of H2O2 in the ozonolysis of alkenes. Atmos Environ. 1993;27:57-61.
[43] Gäb S, Hellpointner E, Turner WV, Korte F. Hydroxymethyl hydroperoxide and bis(hydroxymethyl) peroxide from gas-phase ozonolysis of naturally occurring alkenes. Nature. 1985;316:535-6.
[44] Hatakeyama S, Lai H, Gao S, Murano K. Production of Hydrogen Peroxide and Organic Hydroperoxides in the Reactions of Ozone with Natural Hydrocarbons in Air. Chem Lett. 1993;8:1287-90.
[45] Hewitt CN, Kok GL. Formation and occurrence of organic hydroperoxides in the troposphere: Laboratory and field observations. J Atmos Chem. 1991;12:181-94.
[46] Horie O, Neeb P, Limbach S, Moortgat GK. Formation of formic acid and organic peroxides in the ozonolysis of ethene with added water vapour. Geophys Res Lett. 1994;21:1523-6.
[47] Simonaitis R, Olszyna KJ, Meagher JF. Production of hydrogen peroxide and organic peroxides in the gas phase reactions of ozone with natural alkenes. Geophys Res Lett. 1991;18:912.
[48] Rousso AC, Hansen N, Jasper AW, Ju Y. Low-temperature oxidation of ethylene by ozone in a jet-stirred reactor. J Phys Chem A. 2018;122:8674–85.
[49] Martinez RI, Herron JT, Huie RE. The mechanism of ozone-alkene reactions in the gas phase. A mass spectrometric study of the reactions of eight linear and branched-chain alkenes. J Am Chem Soc. 1981;103:3807-20.
[50] Long B, Bao JL, Truhlar DG. Atmospheric Chemistry of Criegee Intermediates: Unimolecular Reactions and Reactions with Water. J Am Chem Soc. 2016;138:14409-22.
[51] Andersen A, Carter EA. Hybrid Density Functional Theory Predictions of Low-Temperature Dimethyl Ether Combustion Pathways. II. Chain-Branching Energetics and Possible Role of the Criegee Intermediate. J Phys Chem A. 2003;107:9463-78.
[52] Osborn DL, Taatjes CA. The physical chemistry of Criegee intermediates in the gas phase. Int Rev Phys Chem. 2015;34:309-60.
[53] Xing L, Zhang X, Wang Z, Li S, Zhang L. New Insight into Competition between Decomposition Pathways of Hydroperoxymethyl Formate in Low Temperature DME Oxidation. Chin J Chem Phys. 2015;28:563-72.
[54] Vereecken L. The reaction of Criegee intermediates with acids and enols. Phys Chem Chem Phys. 2017;19:28630-40.
[55] Sakamoto Y, Inomata S, Hirokawa J. Oligomerization Reaction of the Criegee Intermediate Leads to Secondary Organic Aerosol Formation in Ethylene Ozonolysis. J Phys Chem A. 2013;117:12912-21.
[56] Neeb P, Horie O, Moortgat GK. The Ethene−Ozone Reaction in the Gas Phase. J Phys Chem A. 1998;102:6778-85.

[57] Welz O, Eskola AJ, Sheps L, Rotavera B, Savee JD, Scheer AM, et al. Rate Coefficients of C1 and C2 Criegee Intermediate Reactions with Formic and Acetic Acid Near the Collision Limit: Direct Kinetics Measurements and Atmospheric Implications. Angew Chem Int Ed. 2014;53:4547-50.
[58] Chhantyal-Pun R, Rotavera B, McGillen MR, Khan MAH, Eskola AJ, Caravan RL, et al. Criegee Intermediate Reactions with Carboxylic Acids: A Potential Source of Secondary Organic Aerosol in the Atmosphere. ACS Earth Space Chem. 2018;2:833-42.
[59] Vereecken L, Francisco JS. Theoretical studies of atmospheric reaction mechanisms in the troposphere. Chem Soc Rev. 2012;41:6259-93.
[60] Liu F, Fang Y, Kumar M, Thompson WH, Lester MI. Direct observation of vinyl hydroperoxide. Phys Chem Chem Phys. 2015;17:20490-4.
[61] Rissanen MP, Kurtén T, Sipilä M, Thornton JA, Kangasluoma J, Sarnela N, et al. The Formation of Highly Oxidized Multifunctional Products in the Ozonolysis of Cyclohexene. J Am Chem Soc. 2014;136:15596-606.
[62] Jokinen T, Berndt T, Makkonen R, Kerminen V-M, Junninen H, Paasonen P, et al. Production of extremely low volatile organic compounds from biogenic emissions: Measured yields and atmospheric implications. Proc Nat Acad Sci. 2015;112:7123-8.
[63] Rissanen MP, Kurtén T, Sipilä M, Thornton JA, Kausiala O, Garmash O, et al. Effects of Chemical Complexity on the Autoxidation Mechanisms of Endocyclic Alkene Ozonolysis Products: From Methylcyclohexenes toward Understanding α-Pinene. J Phys Chem A. 2015;119:4633-50.
[64] Ziemann PJ. Aerosol products, mechanisms, and kinetics of heterogeneous reactions of ozone with oleic acid in pure and mixed particles. Faraday Discuss. 2005;130:469-90.
[65] Surratt JD, Murphy SM, Kroll JH, Ng NL, Hildebrandt L, Sorooshian A, et al. Chemical Composition of Secondary Organic Aerosol Formed from the Photooxidation of Isoprene. J Phys Chem A. 2006;110:9665-90.
[66] Nguyen TB, Bateman AP, Bones DL, Nizkorodov SA, Laskin J, Laskin A. High-resolution mass spectrometry analysis of secondary organic aerosol generated by ozonolysis of isoprene. Atmos Environ. 2010;44:1032-42.
[67] Bateman AP, Nizkorodov SA, Laskin J, Laskin A. Photolytic processing of secondary organic aerosols dissolved in cloud droplets. Phys Chem Chem Phys. 2011;13:12199-212.
[68] Mertes P, Pfaffenberger L, Dommen J, Kalberer M, Baltensperger U. Development of a sensitive long path absorption photometer to quantify peroxides in aerosol particles (PeroxideLOPAP). Atmos Meas Tech. 2012;5:2339-48.
[69] Epstein SA, Blair SL, Nizkorodov SA. Direct Photolysis of α-Pinene Ozonolysis Secondary Organic Aerosol: Effect on Particle Mass and Peroxide Content. Environ Sci Technol. 2014;48:11251-8.
[70] Paulot F, Crounse JD, Kjaergaard HG, Kürten A, St. Clair JM, Seinfeld JH, et al. Unexpected Epoxide Formation in the Gas-Phase Photooxidation of Isoprene. Science. 2009;325:730-3.
[71] Taraborrelli D, Lawrence MG, Crowley JN, Dillon TJ, Gromov S, Groß CBM, et al. Hydroxyl radical buffered by isoprene oxidation over tropical forests. Nat Geosci. 2012;5:190-3.
[72] Boss B, Hazlett R. n-Dodecane Oxidation-Elucidation by Internal Reference Techniques. Ind Eng Chem Prod Res Dev. 1975;14:135-8.
[73] Jensen RK, Korcek S, Mahoney LR, Zinbo M. Liquid-phase autoxidation of organic compounds at elevated temperatures. 1. The stirred flow reactor technique and analysis of primary products from n-hexadecane autoxidation at 120-180.degree.C. J Am Chem Soc. 1979;101:757484.

[74] Blaine S, Savage PE. Reaction pathways in lubricant degradation. 3. Reaction model for nhexadecane autoxidation. Ind Eng Chem Res. 1992;31:69-75.
[75] Pfaendtner J, Broadbelt LJ. Mechanistic Modeling of Lubricant Degradation. 1. Structure−Reactivity Relationships for Free-Radical Oxidation. Ind Eng Chem Res. 2008;47:2886-96.
[76] Bacha K, Ben-Amara A, Vannier A, Alves-Fortunato M, Nardin M. Oxidation Stability of Diesel/Biodiesel Fuels Measured by a PetroOxy Device and Characterization of Oxidation Products. Energy Fuels. 2015;29:4345-55.
[77] Jensen RK, Korcek S, Zinbo M, Johnson MD. Initiation in hydrocarbon autoxidation at elevated temperatures. Int J Chem Kinet. 1990;22:1095-107.
[78] Watkins JM, Mushrush GW, Hazlett RN, Beal EJ. Hydroperoxide formation and reactivity in jet fuels. Energy Fuels. 1989;3:231-6.
[79] Blaine S, Savage PE. Reaction pathways in lubricant degradation. 1. Analytical characterization of n-hexadecane autoxidation products. Ind Eng Chem Res. 1991;30:792-8.
[80] Chatelain K, Nicolle A, Ben Amara A, Catoire L, Starck L. Wide Range Experimental and Kinetic Modeling Study of Chain Length Impact on n-Alkanes Autoxidation. Energy Fuels. 2016;30:1294-303.
[81] Knothe G, Razon LF. Biodiesel fuels. Prog Energy Combust Sci. 2017;58:36-59.
[82] Hamilton EJ, Korcek S, Mahoney LR, Zinbo M. Kinetics and mechanism of the autoxidation of pentaerythrityl tetraheptanoate at 180–220°C. Int J Chem Kinet. 1980;12:577-603.
[83] Jensen RK, Korcek S, Zinbo M. Liquid-phase autoxidation of organic compounds at elevated temperatures. Absolute rate constant for intermolecular hydrogen abstraction in hexadecane autoxidation at 120–190°C. Int J Chem Kinet. 1994;26:673-80.
[84] Battin-Leclerc F. Low-Temperature Combustion Mechanisms. Reference Module in Chemistry, Molecular Sciences and Chemical Engineering: Elsevier; 2015.
[85] Saxena S, Bedoya ID. Fundamental phenomena affecting low temperature combustion and HCCI engines, high load limits and strategies for extending these limits. Prog Energy Combust Sci. 2013;39:457-88.
[86] Musculus MPB, Miles PC, Pickett LM. Conceptual models for partially premixed lowtemperature diesel combustion. Prog Energy Combust Sci. 2013;39:246-83.
[87] Kalghatgi GT. Developments in internal combustion engines and implications for combustion science and future transport fuels. Proc Combust Inst. 2015;35:101-15.
[88] Zhang K, Banyon C, Bugler J, Curran HJ, Rodriguez A, Herbinet O, et al. An updated experimental and kinetic modeling study of n-heptane oxidation. Combust Flame. 2016;172:11635.
[89] Lignola PG, Reverchon E. Cool flames. Prog Energy Combust Sci. 1987;13:75-96.
[90] Griffiths JF, Scott SK. Thermokinetic interactions: Fundamentals of spontaneous ignition and cool flames. Prog Energy Combust Sci. 1987;13:161-97.
[91] Walker RW, Morley C. Basic chemistry of combustion, In: Pilling MJ Ed., Comprehensive Chemical Kinetics: low-temperature combustion and autoignition: Elsevier, Amsterdam; 1997, p. 1-124.
[92] Battin-Leclerc F. Detailed chemical kinetic models for the low-temperature combustion of hydrocarbons with application to gasoline and diesel fuel surrogates. Prog Energy Combust Sci. 2008;34:440-98.

[93] Zádor J, Taatjes CA, Fernandes RX. Kinetics of elementary reactions in low-temperature autoignition chemistry. Prog Energy Combust Sci. 2011;37:371-421.
[94] Westbrook CK, Mehl M, Pitz WJ, Kukkadapu G, Wagnon S, Zhang K. Multi-fuel surrogate chemical kinetic mechanisms for real world applications. Phys Chem Chem Phys. 2018;20:10588606.
[95] Pollard RT. Hydrocarbons. In: Bamford CH, Tipper CFH Eds, Comprehensive chemical kinetics: gas-phase combustion: Elsevier, Amsterdam; 1977, p. 249-367.
[96] Herbinet O, Bax S, Glaude P-A, Carré V, Battin-Leclerc F. Mass spectra of cyclic ethers formed in the low-temperature oxidation of a series of n-alkanes. Fuel. 2011;90:528-35.
[97] Pease RN. Characteristics of the non-explosive oxidation of propane and the butanes. J Am Chem Soc. 1929;51:1839-56.
[98] Curran HJ, Gaffuri P, Pitz WJ, Westbrook CK. A Comprehensive Modeling Study of nHeptane Oxidation. Combust Flame. 1998;114:149-77.
[99] Ranzi E, Faravelli T, Gaffuri P, Sogaro A. Low-temperature combustion: Automatic generation of primary oxidation reactions and lumping procedures. Combust Flame. 1995;102:179-92.
[100] Warth V, Stef N, Glaude PA, Battin-Leclerc F, Scacchi G, Côme GM. Computer-Aided Derivation of Gas-Phase Oxidation Mechanisms: Application to the Modeling of the Oxidation of n-Butane. Combust Flame. 1998;114:81-102.
[101] Sarathy SM, Westbrook CK, Mehl M, Pitz WJ, Togbe C, Dagaut P, et al. Comprehensive chemical kinetic modeling of the oxidation of 2-methylalkanes from C7 to C20. Combust Flame. 2011;158:2338-57.
[102] Curran HJ. Developing detailed chemical kinetic mechanisms for fuel combustion. Proc Combust Inst. 2018;in press, doi: https://doi.org/10.1016/j.proci.2018.06.054.
[103] Klippenstein SJ. From theoretical reaction dynamics to chemical modeling of combustion. Proc Combust Inst. 2017;36:77-111.
[104] Sharma S, Raman S, Green WH. Intramolecular Hydrogen Migration in Alkylperoxy and Hydroperoxyalkylperoxy Radicals: Accurate Treatment of Hindered Rotors. J Phys Chem A. 2010;114:5689-701.
[105] Miyoshi A. Systematic Computational Study on the Unimolecular Reactions of Alkylperoxy (RO2), Hydroperoxyalkyl (QOOH), and Hydroperoxyalkylperoxy (O2QOOH) Radicals. J Phys Chem A. 2011;115:3301-25.
[106] Villano SM, Huynh LK, Carstensen H-H, Dean AM. High-Pressure Rate Rules for Alkyl + O2 Reactions. 2. The Isomerization, Cyclic Ether Formation, and β-Scission Reactions of Hydroperoxy Alkyl Radicals. J Phys Chem A. 2012;116:5068-89.
[107] Cord M, Sirjean B, Fournet R, Tomlin A, Ruiz-Lopez M, Battin-Leclerc F. Improvement of the Modeling of the Low-Temperature Oxidation of n-Butane: Study of the Primary Reactions. J Phys Chem A. 2012;116:6142-58.
[108] Cord M, Husson B, Lizardo Huerta JC, Herbinet O, Glaude P-A, Fournet R, et al. Study of the Low Temperature Oxidation of Propane. J Phys Chem A. 2012;116:12214-28.
[109] Bugler J, Somers KP, Silke EJ, Curran HJ. Revisiting the Kinetics and Thermodynamics of the Low-Temperature Oxidation Pathways of Alkanes: A Case Study of the Three Pentane Isomers. J Phys Chem A. 2015;119:7510-27.
[110] Bugler J, Marks B, Mathieu O, Archuleta R, Camou A, Grégoire C, et al. An ignition delay time and chemical kinetic modeling study of the pentane isomers. Combust Flame. 2016;163:13856.

[111] Bugler J, Rodriguez A, Herbinet O, Battin-Leclerc F, Togbé C, Dayma G, et al. An experimental and modelling study of n-pentane oxidation in two jet-stirred reactors: The importance of pressure-dependent kinetics and new reaction pathways. Proc Combust Inst. 2017;36:441-8.
[112] Mohamed SY, Cai L, Khaled F, Banyon C, Wang Z, Al Rashidi MJ, et al. Modeling Ignition of a Heptane Isomer: Improved Thermodynamics, Reaction Pathways, Kinetics, and Rate Rule Optimizations for 2-Methylhexane. J Phys Chem A. 2016;120:2201-17.
[113] Atef N, Kukkadapu G, Mohamed SY, Rashidi MA, Banyon C, Mehl M, et al. A comprehensive iso-octane combustion model with improved thermochemistry and chemical kinetics. Combust Flame. 2017;178:111-34.
[114] Bissoonauth T, Wang Z, Mohamed SY, Wang J-y, Chen B, Rodriguez A, et al. Methylcyclohexane pyrolysis and oxidation in a jet-stirred reactor. Proc Combust Inst. 2018;In press, doi: https://doi.org/10.1016/j.proci.2018.05.086.
[115] Blurock E, Battin-Leclerc F. Modeling Combustion with Detailed Kinetic Mechanisms. In: Battin-Leclerc F, Simmie J, Blurock E, Eds. Cleaner Combustion: Springer; 2013, p. 17-57.
[116] Cai L, Pitsch H, Mohamed SY, Raman V, Bugler J, Curran H, et al. Optimized reaction mechanism rate rules for ignition of normal alkanes. Combust Flame. 2016;173:468-82.
[117] Sarathy SM, Farooq A, Kalghatgi GT. Recent progress in gasoline surrogate fuels. Prog Energy Combust Sci. 2018;65:67-108.
[118] Zhou C-W, Li Y, O'Connor E, Somers KP, Thion S, Keesee C, et al. A comprehensive experimental and modeling study of isobutene oxidation. Combust Flame. 2016;167:353-79.
[119] Meng X, Rodriguez A, Herbinet O, Wang T, Battin-Leclerc F. Revisiting 1-hexene lowtemperature oxidation. Combust Flame. 2017;181:283-99.
[120] Rodriguez A, Frottier O, Herbinet O, Fournet R, Bounaceur R, Fittschen C, et al. Experimental and Modeling Investigation of the Low-Temperature Oxidation of Dimethyl Ether. J Phys Chem A. 2015;119:7905-23.
[121] Sarathy SM, Oßwald P, Hansen N, Kohse-Höinghaus K. Alcohol combustion chemistry. Prog Energy Combust Sci. 2014;44:40-102.
[122] Rodriguez A, Herbinet O, Battin-Leclerc F. A study of the low-temperature oxidation of a long chain aldehyde: n-hexanal. Proc Combust Inst. 2017;36:365-72.
[123] Battin-Leclerc F, Herbinet O, Glaude P-A, Fournet R, Zhou Z, Deng L, et al. Experimental Confirmation of the Low-Temperature Oxidation Scheme of Alkanes. Angew Chem Int Ed. 2010;49:3169-72.
[124] Semenov NN. Some general considerations in connection with the chain-reaction theory. Trans Faraday Soc. 1932;28:818-22.
[125] Semenov NN. Some Problems in Chemical Kinetics and Reactivity: vol. 2, Pergamon Press, London; 1959.
[126] Cartlidge J, Tipper CFH. Knock resistance and anti-knock with hydrocarbon fuels. Combust Flame. 1961;5:87-91.
[127] Burgess AR, Laughlin RGW. The role of hydroperoxides as chain-branching agents in the cool-flame oxidation of n-heptane. Chem Com. 1967;0:769-70.
[128] Knox JH. Low-temperature combustion phenomena. In: Ashmore PG, Sugden TM, Dainton FS Eds., Photochemistry and reaction kinetics: Cambridge University Press, Cambridge; 1967, p. 250-286.
[129] Fish A. Oxidation of organic compounds, vol 2. Advances in Chemistry Series, 1968, p. 6985.
[130] Fish A. The Cool Flames of Hydrocarbons. Angew Chem Int Edit. 1968;7:45-60.

[131] Benson SW. The kinetics and thermochemistry of chemical oxidation with application to combustion and flames. Prog Energy Combust Sci. 1981;7:125-34.
[132] Cox RA, Cole JA. Chemical aspects of the autoignition of hydrocarbon-air mixtures. Combust Flame. 1985;60:109-23.
[133] Halstead MP, Kirsch LJ, Prothero A, Quinn CP. A mathematical model for hydrocarbon autoignition at high pressures. Proc R Soc Lond A. 1975;346:515-38.
[134] Pitz WJ, Wilk RD, Westbrook CK, Cernansky NP. The oxidation of n-butane at low and intermediate temperatures: an experimental and modeling study. Paper n° WSSCI 88-51, Western States Sections / The Combustion Institute Spring Meeting. 1988.
[135] Chevalier C, Pitz WJ, Warnatz J, Westbrook CK, Melenk H. Hydrocarbon ignition: Automatic generation of reaction mechanisms and applications to modeling of engine knock. Proc Combust Inst. 1992;24:93-101.
[136] Cartlidge J, Tipper CFH. The role of peroxides in slow combustion of hydrocarbons. Proc Chem Soc. 1960:219.
[137] Cartlidge J, Tipper CFH. Analysis of peroxides separation and identification by paper chromatography. Anal Chim Acta. 1960;22:106-10.
[138] Sahetchian K, Rigny R, Blin N. Evaluation of Hydroperoxide Concentrations During the Delay of Autoignition in an Experimental Four Stroke Engine: Comparison with Cool Flame Studies in a Flow System. Combust Sci Technol. 1988;60:117-24.
[139] Sahetchian KA, Blin N, Rigny R, Seydi A, Murat M. The oxidation of n-butane and nheptane in a CFR engine. Isomerization reactions and delay of autoignition. Combust Flame. 1990;79:242-9.
[140] Brock C, Stanley D. The Cooperative Fuels Research engine: Applications for education and research. J Aviat Technol Eng. 2012;2:130–5.
[141] Curran HJ, Gaffuri P, Pitz WJ, Westbrook CK, Leppard WR. Autoignition chemistry in a motored engine: An experimental and kinetic modeling study. Proc Combust Inst. 1996;26:266977.
[142] Zhang Y, Boehman AL. Oxidation of 1-butanol and a mixture of n-heptane/1-butanol in a motored engine. Combust Flame. 2010;157:1816-24.
[143] Leppard WR. The Autoignition Chemistry of n-Butane: An Experimental Study. SAE Transactions. 1987;96:934-57.
[144] Leppard WR. The Chemical Origin of Fuel Octane Sensitivity. SAE International; 1990.
[145] Bhavani Shankar VS, Sajid M, Al-Qurashi K, Atef N, Alkhesho I, Ahmed A, et al. Primary Reference Fuels (PRFs) as Surrogates for Low Sensitivity Gasoline Fuels. SAE International; 2016.
[146] Wang Z, Chen B, Moshammer K, Popolan-Vaida DM, Sioud S, Shankar VSB, et al. nHeptane cool flame chemistry: Unraveling intermediate species measured in a stirred reactor and motored engine. Combust Flame. 2018;187:199-216.
[147] Sahetchian KA, Rigny R, Circan S. Identification of the hydroperoxide formed by isomerization reactions during the oxidation of n-heptane in a reactor and CFR engine. Combust Flame. 1991;85:511-4.
[148] Blin-Simiand N, Rigny R, Viossat V, Circan S, Sahetchian K. Autoignition of Hydrocarbon/Air Mixtures in a CFR Engine: Experimental and Modeling Study. Combust Sci Technol. 1993;88:329-48.

[149] Jorand F, Heiss A, Perrin O, Sahetchian K, Kerhoas L, Einhorn J. Isomeric hexylketohydroperoxides formed by reactions of hexoxy and hexylperoxy radicals in oxygen. Int J Chem Kinet. 2003;35:354-66.
[150] Blin-Simiand N, Jorand F, Sahetchian K, Brun M, Kerhoas L, Malosse C, et al. Hydroperoxides with zero, one, two or more carbonyl groups formed during the oxidation of ndodecane. Combust Flame. 2001;126:1524-32.
[151] Taatjes CA, Hansen N, McIlroy A, Miller JA, Senosiain JP, Klippenstein SJ, et al. Enols Are Common Intermediates in Hydrocarbon Oxidation. Science. 2005;308:1887-9.
[152] Qi F. Combustion chemistry probed by synchrotron VUV photoionization mass spectrometry. Proc Combust Inst. 2013;34:33-63.
[153] Herbinet O, Battin-Leclerc F. Progress in Understanding Low-Temperature Organic Compound Oxidation Using a Jet-Stirred Reactor. Int J Chem Kinet. 2014;46:619-39.
[154] Battin-Leclerc F, Herbinet O, Glaude P-A, Fournet R, Zhou Z, Deng L, et al. New experimental evidences about the formation and consumption of ketohydroperoxides. Proc Combust Inst. 2011;33:325-31.
[155] Montgomery Jr. JA, Frisch MJ, Ochterski JW, Petersson GA. A complete basis set model chemistry. VI. Use of density functional geometries and frequencies. J Chem Phys. 1999;110:2822-7.
[156] Frisch MJ, Trucks GW, Schlegel HB, Scuseria GE, Robb MA, Cheeseman JR, et al. Gaussian03, revision B05; Gaussian, Inc.: Wallingford, CT. 2004.
[157] Moshammer K, Jasper AW, Popolan-Vaida DM, Lucassen A, Diévart P, Selim H, et al. Detection and Identification of the Keto-Hydroperoxide (HOOCH2OCHO) and Other Intermediates during Low-Temperature Oxidation of Dimethyl Ether. J Phys Chem A. 2015;119:7361-74.
[158] Eskola AJ, Welz O, Zádor J, Antonov IO, Sheps L, Savee JD, et al. Probing the lowtemperature chain-branching mechanism of n-butane autoignition chemistry via time-resolved measurements of ketohydroperoxide formation in photolytically initiated n-C4H10 oxidation. Proc Combust Inst. 2015;35:291-8.
[159] Herbinet O, Dayma G. Jet-Stirred Reactors. In: Battin-Leclerc F, Simmie JM, Blurock E, editors. Cleaner Combustion: Developing Detailed Chemical Kinetic Models. London: Springer London; 2013. p. 183-210.
[160] Monge F, Aranda V, Millera A, Bilbao R, Alzueta MU. Tubular Flow Reactors. In: BattinLeclerc F, Simmie JM, Blurock E, editors. Cleaner Combustion: Developing Detailed Chemical Kinetic Models. London: Springer London; 2013. p. 211-30.
[161] Brezinsky K. The high-temperature oxidation of aromatic hydrocarbons. Prog Energy Combust Sci. 1986;12:1-24.
[162] Song Y, Hashemi H, Christensen JM, Zou C, Haynes BS, Marshall P, et al. An Exploratory Flow Reactor Study of H2S Oxidation at 30–100 Bar. Int J Chem Kinet. 2017;49:37-52.
[163] Levenspiel O. Chemical Reaction Engineering, 3rd edn. Wiley, New York, 1999.
[164] Abian M, Alzueta MU, Glarborg P. Formation of NO from N2/O2 Mixtures in a Flow Reactor: Toward an Accurate Prediction of Thermal NO. Int J Chem Kinet. 2015;47:518-32.
[165] Herbinet O, Husson B, Le Gall H, Battin-Leclerc F. Comparison study of the gas-phase oxidation of alkylbenzenes and alkylcyclohexanes. Chem Eng Sci. 2015;131:49-62.
[166] Dagaut P, Reuillon M, Cathonnet M. Experimental study of the oxidation of n-heptane in a jet stirred reactor from low to high temperature and pressures up to 40 atm. Combust Flame. 1995;101:132-40.

[167] de Joannon M, Cavaliere A, Faravelli T, Ranzi E, Sabia P, Tregrossi A. Analysis of process parameters for steady operations in methane mild combustion technology. Proc Combust Inst. 2005;30:2605-12.
[168] Matras D, Villermaux J. Un réacteur continu parfaitement agité par jets gazeux pour l'étude cinétique de réactions chimiques rapides. Chem Eng Sci. 1973;28:129-37.
[169] Curran HJ, Fischer SL, Dryer FL. The reaction kinetics of dimethyl ether. II: Lowtemperature oxidation in flow reactors. Int J Chem Kinet. 2000;32:741-59.
[170] Chen B, Wang Z, Wang J-Y, Wang H, Togbé C, Alonso PEÁ, et al. Exploring gasoline oxidation chemistry in jet stirred reactors. Fuel. 2019;236:1282-92.
[171] Rodriguez A, Herbinet O, Wang Z, Qi F, Fittschen C, Westmoreland PR, et al. Measuring hydroperoxide chain-branching agents during n-pentane low-temperature oxidation. Proc Combust Inst. 2017;36:333-42.
[172] Wang Z, Popolan-Vaida DM, Chen B, Moshammer K, Mohamed SY, Wang H, et al. Unraveling the structure and chemical mechanisms of highly oxygenated intermediates in oxidation of organic compounds. Proc Nat Acad Sci. 2017;114:13102-7.
[173] Guo H, Sun W, Haas FM, Farouk T, Dryer FL, Ju Y. Measurements of H2O2 in low temperature dimethyl ether oxidation. Proc Combust Inst. 2013;34:573-81.
[174] Egolfopoulos FN, Hansen N, Ju Y, Kohse-Höinghaus K, Law CK, Qi F. Advances and challenges in laminar flame experiments and implications for combustion chemistry. Prog Energy Combust Sci. 2014;43:36-67.
[175] Taatjes CA, Hansen N, Osborn DL, Kohse-Höinghaus K, Cool TA, Westmoreland PR. "Imaging" combustion chemistry via multiplexed synchrotron-photoionization mass spectrometry. Phys Chem Chem Phys. 2008;10:20-34.
[176] Hansen N, Cool TA, Westmoreland PR, Kohse-Höinghaus K. Recent contributions of flamesampling molecular-beam mass spectrometry to a fundamental understanding of combustion chemistry. Prog Energy Combust Sci. 2009;35:168-91.
[177] Anderson JB. Molecular beams from nozzle sources. In: Wegener PP, Ed. Molecular beams and low density gasdynamics. New York: Marcel Dekker, Inc.; 1974. p. 1-91.
[178] Kantrowitz A, Grey J. A High Intensity Source for the Molecular Beam. Part I. Theoretical. Rev Sci Instrum. 1951;22:328-32.
[179] Smalley RE, Wharton L, Levy DH. Molecular optical spectroscopy with supersonic beams and jets. Acc Chem Res. 1977;10:139-45.
[180] Moshammer K, Jasper AW, Popolan-Vaida DM, Wang Z, Bhavani Shankar VS, Ruwe L, et al. Quantification of the Keto-Hydroperoxide (HOOCH2OCHO) and Other Elusive Intermediates during Low-Temperature Oxidation of Dimethyl Ether. J Phys Chem A. 2016;120:7890-901.
[181] Kamphus M, Liu NN, Atakan B, Qi F, McIlroy A. REMPI temperature measurement in molecular beam sampled low-pressure flames. Proc Combust Inst. 2002;29:2627-33.
[182] Zhao H, Wu L, Patrick C, Zhang Z, Rezgui Y, Yang X, et al. Studies of low temperature oxidation of n-pentane with nitric oxide addition in a jet stirred reactor. Combust Flame. 2018;197:78-87.
[183] Zhao H, Dana AG, Zhang Z, Green WH, Ju Y. Experimental and modeling study of the mutual oxidation of N-pentane and nitrogen dioxide at low and high temperatures in a jet stirred reactor. Energy. 2018;165:727-38.
[184] Rodriguez A, Herbinet O, Meng X, Fittschen C, Wang Z, Xing L, et al. Hydroperoxide Measurements During Low-Temperature Gas-Phase Oxidation of n-Heptane and n-Decane. J Phys Chem A. 2017;121:1861-76.

[185] Leone SR, Ahmed M, Wilson KR. Chemical dynamics, molecular energetics, and kinetics at the synchrotron. Phys Chem Chem Phys. 2010;12:6564-78.
[186] Zhou Z, Du X, Yang J, Wang Y, Li C, Wei S, et al. The vacuum ultraviolet beamline/endstations at NSRL dedicated to combustion research. J Synchrotron Radiat. 2016;23:1035-45.
[187] Li Y, Qi F. Recent Applications of Synchrotron VUV Photoionization Mass Spectrometry: Insight into Combustion Chemistry. Acc Chem Res. 2010;43:68-78.
[188] Qi F, Yang R, Yang B, Huang C, Wei L, Wang J, et al. Isomeric identification of polycyclic aromatic hydrocarbons formed in combustion with tunable vacuum ultraviolet photoionization. Rev Sci Instrum. 2006;77:084101.
[189] Oßwald P, Hemberger P, Bierkandt T, Akyildiz E, Köhler M, Bodi A, et al. In situ flame chemistry tracing by imaging photoelectron photoion coincidence spectroscopy. Rev Sci Instrum. 2014;85:025101.
[190] Krüger J, Garcia GA, Felsmann D, Moshammer K, Lackner A, Brockhinke A, et al. Photoelectron–photoion coincidence spectroscopy for multiplexed detection of intermediate species in a flame. Phys Chem Chem Phys. 2014;16:22791-804.
[191] Krüger D, Oßwald P, Köhler M, Hemberger P, Bierkandt T, Karakaya Y, et al. Hydrogen abstraction ratios: A systematic iPEPICO spectroscopic investigation in laminar flames. Combust Flame. 2018;191:343-52.
[192] Felsmann D, Moshammer K, Krüger J, Lackner A, Brockhinke A, Kasper T, et al. Electron ionization, photoionization and photoelectron/photoion coincidence spectroscopy in massspectrometric investigations of a low-pressure ethylene/oxygen flame. Proc Combust Inst. 2015;35:779-86.
[193] Pieper J, Schmitt S, Hemken C, Davies E, Wullenkord J, Brockhinke A, et al. Isomer Identification in Flames with Double-Imaging Photoelectron/Photoion Coincidence Spectroscopy (i2PEPICO) using Measured and Calculated Reference Photoelectron Spectra. Z Phys Chem. 2018;232:153.
[194] Adamson BA, Skeen SA, Ahmed M, Hansen N. Detection of Aliphatically Bridged MultiCore Polycyclic Aromatic Hydrocarbons in Sooting Flames with Atmospheric-Sampling HighResolution Tandem Mass Spectrometry. J Phys Chem A. 2018;122:9338–49.
[195] Cool TA, Nakajima K, Taatjes CA, McIlroy A, Westmoreland PR, Law ME, et al. Studies of a fuel-rich propane flame with photoionization mass spectrometry. Proc Combust Inst. 2005;30:1681-8.
[196] Osswald P, Struckmeier U, Kasper T, Kohse-Höinghaus K, Wang J, Cool TA, et al. IsomerSpecific Fuel Destruction Pathways in Rich Flames of Methyl Acetate and Ethyl Formate and Consequences for the Combustion Chemistry of Esters. J Phys Chem A. 2007;111:4093-101.
[197] Tao T, Sun W, Hansen N, Jasper AW, Moshammer K, Chen B, et al. Exploring the negative temperature coefficient behavior of acetaldehyde based on detailed intermediate measurements in a jet-stirred reactor. Combust Flame. 2018;192:120-9.
[198] Dodson LG, Shen L, Savee JD, Eddingsaas NC, Welz O, Taatjes CA, et al. VUV Photoionization Cross Sections of HO2, H2O2, and H2CO. J Phys Chem A. 2015;119:1279-91.
[199] Bobeldijk M, van der Zande WJ, Kistemaker PG. Simple models for the calculation of photoionization and electron impact ionization cross sections of polyatomic molecules. Chem Phys. 1994;179:125-30.
[200] Gianturco FA, Lucchese RR, Sanna N. Calculation of low-energy elastic cross sections for electron-CF4 scattering. J Chem Phys. 1994;100:6464-71.

[201] Gans B, Boyé-Péronne S, Broquier M, Delsaut M, Douin S, Fellows CE, et al. Photolysis of methane revisited at 121.6 nm and at 118.2 nm: quantum yields of the primary products, measured by mass spectrometry. Phys Chem Chem Phys. 2011;13:8140-52.
[202] Jacovella U, Holland DMP, Boyé-Péronne S, Gans B, de Oliveira N, Ito K, et al. A NearThreshold Shape Resonance in the Valence-Shell Photoabsorption of Linear Alkynes. J Phys Chem A. 2015;119:12339-48.
[203] Jacovella U, Holland DMP, Boyé-Péronne S, Gans B, de Oliveira N, Joyeux D, et al. Highresolution vacuum-ultraviolet photoabsorption spectra of 1-butyne and 2-butyne. J Chem Phys. 2015;143:034304.
[204] Natalense APP, Lucchese RR. Cross section and asymmetry parameter calculation for sulfur 1s photoionization of SF6. J Chem Phys. 1999;111:5344-8.
[205] Oana CM, Krylov AI. Dyson orbitals for ionization from the ground and electronically excited states within equation-of-motion coupled-cluster formalism: Theory, implementation, and examples. J Chem Phys. 2007;127:234106.
[206] Wilhelmy I, Ackermann L, Görling A, Rösch N. Molecular photoionization cross sections by the Lobatto technique. I. Valence photoionization. J Chem Phys. 1994;100:2808-20.
[207] Ruberti M, Yun R, Gokhberg K, Kopelke S, Cederbaum LS, Tarantelli F, et al. Total molecular photoionization cross-sections by algebraic diagrammatic construction-StieltjesLanczos method: Benchmark calculations. J Chem Phys. 2013;139:144107.
[208] Gokhberg K, Vysotskiy V, Cederbaum LS, Storchi L, Tarantelli F, Averbukh V. Molecular photoionization cross sections by Stieltjes–Chebyshev moment theory applied to Lanczos pseudospectra. J Chem Phys. 2009;130:064104.
[209] Lehmann KK, Berden G, Engeln R. An introduction to Cavity ring-down spectroscopy. In: Berden G, Engeln R, Eds. Cavity ring-down spectroscopy: Techniques and application, John Wiley & Sons, Ltd; . 2009, p. 1–26.
[210] Macko P, Romanini D, Mikhailenko SN, Naumenko OV, Kassi S, Jenouvrier A, et al. High sensitivity CW-cavity ring down spectroscopy of water in the region of the 1.5μm atmospheric window. J Mol Spectrosc. 2004;227:90-108.
[211] Campargue A, Barbe A, De Backer-Barilly MR, Tyuterev VG, Kassi S. The near infrared spectrum of ozone by CW-cavity ring down spectroscopy between 5850 and 7000 cm−1: new observations and exhaustive review. Phys Chem Chem Phys. 2008;10:2925-46.
[212] Jain C, Morajkar P, Schoemaecker C, Viskolcz B, Fittschen C. Measurement of Absolute Absorption Cross Sections for Nitrous Acid (HONO) in the Near-Infrared Region by the Continuous Wave Cavity Ring-Down Spectroscopy (cw-CRDS) Technique Coupled to Laser Photolysis. J Phys Chem A. 2011;115:10720-8.
[213] Assaf E, Fittschen C. Cross Section of OH Radical Overtone Transition near 7028 cm−1 and Measurement of the Rate Constant of the Reaction of OH with HO2 Radicals. J Phys Chem A. 2016;120:7051-9.
[214] Mercier X, Desgroux P. Cavity ring-down spectroscopy for combustion studies. In: Berden G, Engeln R, editors. Cavity ring-down spectroscopy: Techniques and application, John Wiley & Sons, Ltd; . 2009, p. 273–311.
[215] Cheskis S, Goldman A. Laser diagnostics of trace species in low-pressure flat flame. Prog Energy Combust Sci. 2009;35:365-82.
[216] Meijer G, Boogaarts MGH, Jongma RT, Parker DH, Wodtke AM. Coherent cavity ring down spectroscopy. Chem Phys Lett. 1994;217:112-6.

[217] Bouvier Y, Mihesan C, Ziskind M, Therssen E, Focsa C, Pauwels JF, et al. Molecular species adsorbed on soot particles issued from low sooting methane and acetylene laminar flames: A laserbased experiment. Proc Combust Inst. 2007;31:841-9.
[218] Romanini D, Kachanov AA, Sadeghi N, Stoeckel F. CW cavity ring down spectroscopy. Chem Phys Lett. 1997;264:316-22.
[219] Mercier X, Therssen E, Pauwels JF, Desgroux P. Quantitative features and sensitivity of cavity ring-down measurements of species concentrations in flames. Combust Flame. 2001;124:656-67.
[220] Bahrini C, Herbinet O, Glaude P-A, Schoemaecker C, Fittschen C, Battin-Leclerc F. Detection of some stable species during the oxidation of methane by coupling a jet-stirred reactor (JSR) to cw-CRDS. Chem Phys Lett. 2012;534:1-7.
[221] Djehiche M, Le Tan NL, Jain CD, Dayma G, Dagaut P, Chauveau C, et al. Quantitative Measurements of HO2 and Other Products of n-Butane Oxidation (H2O2, H2O, CH2O, and C2H4) at Elevated Temperatures by Direct Coupling of a Jet-Stirred Reactor with Sampling Nozzle and Cavity Ring-Down Spectroscopy (cw-CRDS). J Am Chem Soc. 2014;136:16689-94.
[222] Ruth Albert A, Heitmann U, Heinecke E, Fittschen C. The Rotationally-Resolved Absorption Spectrum of Formaldehyde from 6547 to 7051 cm−1. Z Phys Chem. 2015;229:1609.
[223] Parker AE, Jain C, Schoemaecker C, Szriftgiser P, Votava O, Fittschen C. Simultaneous, time-resolved measurements of OH and HO2 radicals by coupling of high repetition rate LIF and cw-CRDS techniques to a laser photolysis reactor and its application to the photolysis of H2O2. Appl Phys B. 2011;103:725-33.
[224] Bahrini C, Herbinet O, Glaude P-A, Schoemaecker C, Fittschen C, Battin-Leclerc F. Quantification of Hydrogen Peroxide during the Low-Temperature Oxidation of Alkanes. J Am Chem Soc. 2012;134:11944-7.
[225] Bahrini C, Morajkar P, Schoemaecker C, Frottier O, Herbinet O, Glaude P-A, et al. Experimental and modeling study of the oxidation of n-butane in a jet stirred reactor using cwCRDS measurements. Phys Chem Chem Phys. 2013;15:19686-98.
[226] Le Tan NL, Djehiche M, Jain CD, Dagaut P, Dayma G. Quantification of HO2 and other products of dimethyl ether oxidation (H2O2, H2O, and CH2O) in a jet-stirred reactor at elevated temperatures by low-pressure sampling and continuous-wave cavity ring-down spectroscopy. Fuel. 2015;158:248-52.
[227] Griffiths JF, Hughes KJ, Porter R. The role and rate of hydrogen peroxide decomposition during hydrocarbon two-stage autoignition. Proc Combust Inst. 2005;30:1083-91.
[228] Carlier M, Corre C, Minetti R, Pauwels JF, Ribaucour M, Sochet LR. Autoignition of butane: A burner and a rapid compression machine study. Proc Combust Inst. 1991;23:1753-8.
[229] Ju Y, Reuter CB, Yehia OR, Farouk TI, Won SH. Cool flames and their impact on engine fuel development. Prog Energy Combust Sci. 2018;submitted.
[230] Arcoumanis C, Bae C, Crookes R, Kinoshita E. The potential of di-methyl ether (DME) as an alternative fuel for compression-ignition engines: A review. Fuel. 2008;87:1014-30.
[231] Leitner W, Klankermayer J, Pischinger S, Pitsch H, Kohse-Höinghaus K. Advanced Biofuels and Beyond: Chemistry Solutions for Propulsion and Production. Angew Chem Int Ed. 2017;56:5412-52.
[232] Liu H, Wang Z, Wang J, He X. Improvement of emission characteristics and thermal efficiency in diesel engines by fueling gasoline/diesel/PODEn blends. Energy. 2016;97:105-12.
[233] Kohse-Höinghaus K, Oßwald P, Cool TA, Kasper T, Hansen N, Qi F, et al. Biofuel Combustion Chemistry: From Ethanol to Biodiesel. Angew Chem Int Ed. 2010;49:3572-97.

[234] Kurimoto N, Brumfield B, Yang X, Wada T, Diévart P, Wysocki G, et al. Quantitative measurements of HO2/H2O2 and intermediate species in low and intermediate temperature oxidation of dimethyl ether. Proc Combust Inst. 2015;35:457-64.
[235] Herbinet O, Battin-Leclerc F, Bax S, Gall HL, Glaude P-A, Fournet R, et al. Detailed product analysis during the low temperature oxidation of n-butane. Phys Chem Chem Phys. 2011;13:296308.
[236] Sun W, Tao T, Lailliau M, Hansen N, Yang B, Dagaut P. Exploration of the oxidation chemistry of dimethoxymethane: Jet-stirred reactor experiments and kinetic modeling. Combust Flame. 2018;193:491-501.
[237] Liao H, Tao T, Sun W, Hansen N, Law CK, Yang B. Investigation of the low-temperature oxidation of n-butanal in a jet-stirred reactor. Proc Combust Inst. 2018;in press, doi: https://doi.org/10.1016/j.proci.2018.06.217.
[238] Linstrom PJ, Mallard WG. NIST Chemistry Webbook, National Institute of Standard and Technology, Number 69, Gaithersburg, MD, http://webbook.nist.gov/. 2005.
[239] Koizumi H. Predominant decay channel for superexcited organic molecules. J Chem Phys. 1991;95:5846-52.
[240] Baulch DL, Cobos CJ, Cox RA, Frank P, Hayman G, Just T, et al. Evaluated Kinetic Data for Combustion Modeling. Supplement I. J Phys Chem Ref Data. 1994;23:847-8.
[241] Troe J. The thermal dissociation/recombination reaction of hydrogen peroxide H2O2(+M)⇔2OH(+M) III.: Analysis and representation of the temperature and pressure dependence over wide ranges. Combust Flame. 2011;158:594-601.
[242] Burke U, Somers KP, O'Toole P, Zinner CM, Marquet N, Bourque G, et al. An ignition delay and kinetic modeling study of methane, dimethyl ether, and their mixtures at high pressures. Combust Flame. 2015;162:315-30.
[243] Wang Z, Zhang X, Xing L, Zhang L, Herrmann F, Moshammer K, et al. Experimental and kinetic modeling study of the low- and intermediate-temperature oxidation of dimethyl ether. Combust Flame. 2015;162:1113-25.
[244] Vermeire FH, Carstensen H-H, Herbinet O, Battin-Leclerc F, Marin GB, Van Geem KM. Experimental and modeling study of the pyrolysis and combustion of dimethoxymethane. Combust Flame. 2018;190:270-83.
[245] Marrodán L, Royo E, Millera Á, Bilbao R, Alzueta MU. High Pressure Oxidation of Dimethoxymethane. Energy Fuels. 2015;29:3507-17.
[246] Varga T, Olm C, Nagy T, Zsély IG, Valkó É, Pálvölgyi R, et al. Development of a Joint Hydrogen and Syngas Combustion Mechanism Based on an Optimization Approach. Int J Chem Kinet. 2016;48:407-22.
[247] Blocquet M, Schoemaecker C, Amedro D, Herbinet O, Battin-Leclerc F, Fittschen C. Quantification of OH and HO2 radicals during the low-temperature oxidation of hydrocarbons by Fluorescence Assay by Gas Expansion technique. Proc Nat Acad Sci. 2013;110:20014-7.
[248] Brumfield B, Sun W, Ju Y, Wysocki G. Direct In Situ Quantification of HO2 from a Flow Reactor. J Phys Chem Lett. 2013;4:872-6.
[249] Zhang X, Ye L, Li Y, Zhang Y, Cao C, Yang J, et al. Acetaldehyde oxidation at low and intermediate temperatures: An experimental and kinetic modeling investigation. Combust Flame. 2018;191:431-41.

[250] Zhang X, Li Y, Cao C, Zou J, Zhang Y, Li W, et al. New insights into propanal oxidation at low temperatures: An experimental and kinetic modeling study. Proc Combust Inst. 2018;in press, doi: https://doi.org/10.1016/j.proci.2018.06.173.
[251] Battin-Leclerc F, Rodriguez A, Husson B, Herbinet O, Glaude P-A, Wang Z, et al. Products from the Oxidation of Linear Isomers of Hexene. J Phys Chem A. 2014;118:673-83.
[252] Wang Z, Mohamed SY, Zhang L, Moshammer K, Popolan-Vaida DM, Shankar VSB, et al. New insights into the low-temperature oxidation of 2-methylhexane. Proc Combust Inst. 2017;36:373-82.
[253] Biet J, Hakka MH, Warth V, Glaude P-A, Battin-Leclerc F. Experimental and Modeling Study of the Low-Temperature Oxidation of Large Alkanes. Energy Fuels. 2008;22:2258-69.
[254] Wang Z, Herbinet O, Cheng Z, Husson B, Fournet R, Qi F, et al. Experimental Investigation of the Low Temperature Oxidation of the Five Isomers of Hexane. J Phys Chem A. 2014;118:5573-94.
[255] Herbinet O, Husson B, Serinyel Z, Cord M, Warth V, Fournet R, et al. Experimental and modeling investigation of the low-temperature oxidation of n-heptane. Combust Flame. 2012;159:3455-71.
[256] Pelucchi M, Ranzi E, Frassoldati A, Faravelli T. Alkyl radicals rule the low temperature oxidation of long chain aldehydes. Proc Combust Inst. 2017;36:393-401.
[257] Pelucchi M, Somers KP, Yasunaga K, Burke U, Frassoldati A, Ranzi E, et al. An experimental and kinetic modeling study of the pyrolysis and oxidation of n-C3C5 aldehydes in shock tubes. Combust Flame. 2015;162:265-86.
[258] Wang Z, Zhang L, Moshammer K, Popolan-Vaida DM, Shankar VSB, Lucassen A, et al. Additional chain-branching pathways in the low-temperature oxidation of branched alkanes. Combust Flame. 2016;164:386-96.
[259] Antonov IO, Zádor J, Rotavera B, Papajak E, Osborn DL, Taatjes CA, et al. PressureDependent Competition among Reaction Pathways from First- and Second-O2 Additions in the Low-Temperature Oxidation of Tetrahydrofuran. J Phys Chem A. 2016;120:6582-95.
[260] Eskola AJ, Antonov IO, Sheps L, Savee JD, Osborn DL, Taatjes CA. Time-resolved measurements of product formation in the low-temperature (550–675 K) oxidation of neopentane: a probe to investigate chain-branching mechanism. Phys Chem Chem Phys. 2017;19:13731-45.
[261] Sun W, Lailliau M, Serinyel Z, Dayma G, Moshammer K, Hansen N, et al. Insights into the oxidation kinetics of a cetane improver – 1,2-dimethoxyethane (1,2-DME) with experimental and modeling methods. Proc Combust Inst. 2018;in press, doi: https://doi.org/10.1016/j.proci.2018.06.077.
[262] Koritzke AL, Davis JC, Caravan RL, Christianson MG, Osborn DL, Taatjes CA, et al. ˙QOOH-mediated reactions in cyclohexene oxidation. Proc Combust Inst. 2018;in press, doi: https://doi.org/10.1016/j.proci.2018.05.029.
[263] Wang J, Yang B, Cool TA, Hansen N, Kasper T. Near-threshold absolute photoionization cross-sections of some reaction intermediates in combustion. Int J Mass spectrom. 2008;269:21020.
[264] McLafferty FW, Turecek F. Interpretation of mass spectra, University science books, 1993, p. 1-371.
[265] Xing L, Bao JL, Wang Z, Zhang F, Truhlar DG. Degradation of Carbonyl Hydroperoxides in the Atmosphere and in Combustion. J Am Chem Soc. 2017;139:15821-35.

[266] Westbrook CK, Dryer FL. Chemical kinetic modeling of hydrocarbon combustion. Prog Energy Combust Sci. 1984;10:1-57.
[267] McLane CK. Hydrogen Peroxide in the Thermal Hydrogen Oxygen Reaction I. Thermal Decomposition of Hydrogen Peroxide. J Chem Phys. 1949;17:379-85.
[268] Baldwin RR, Brattan D. Homogeneous gas-phase decomposition of hydrogen peroxide. Proc Combust Inst. 1961;8:110-9.
[269] Meyer E, Olschewski HA, Troe J, Wagner HG. Investigation of N2H4 and H2O2 decomposition in low and high pressure shock waves. Proc Combust Inst. 1969;12:345-55.
[270] Kappel C, Luther K, Troe J. Shock wave study of the unimolecular dissociation of H2O2 in its falloff range and of its secondary reactions. Phys Chem Chem Phys. 2002;4:4392-8.
[271] Hong Z, Farooq A, Barbour EA, Davidson DF, Hanson RK. Hydrogen Peroxide Decomposition Rate: A Shock Tube Study Using Tunable Laser Absorption of H2O near 2.5 μm. J Phys Chem A. 2009;113:12919-25.
[272] Sajid MB, Es-sebbar E, Javed T, Fittschen C, Farooq A. Measurement of the Rate of Hydrogen Peroxide Thermal Decomposition in a Shock Tube Using Quantum Cascade Laser Absorption Near 7.7 μm. Int J Chem Kinet. 2014;46:275-84.
[273] Sellevåg SR, Georgievskii Y, Miller JA. Kinetics of the Gas-Phase Recombination Reaction of Hydroxyl Radicals to Form Hydrogen Peroxide. J Phys Chem A. 2009;113:4457-67.
[274] Hong Z, Cook RD, Davidson DF, Hanson RK. A Shock Tube Study of OH + H2O2 → H2O + HO2 and H2O2 + M → 2OH + M using Laser Absorption of H2O and OH. J Phys Chem A. 2010;114:5718-27.
[275] Baulch DL, Bowman CT, Cobos CJ, Cox RA, Just T, Kerr JA, et al. Evaluated Kinetic Data for Combustion Modeling: Supplement II. J Phys Chem Ref Data. 2005;34:757-1397.
[276] Baldwin RR, Brattan D, Tunnicliffe B, Walker RW, Webster SJ. The hydrogen-sensitized decomposition of hydrogen peroxide. Combust Flame. 1970;15:133-42.
[277] Kirk AD, Knox JH. The pyrolysis of alkyl hydroperoxides in the gas phase. Trans Faraday Soc. 1960;56:1296-303.
[278] Sahetchian KA, Heiss A, Rigny R, Ben-aïm RI. Determination of the gas-phase decomposition rate constants of heptyl-1 and heptyl-2 hydroperoxides (C7H15OOH). Int J Chem Kinet. 1982;14:1325-37.
[279] Vardanyan IA, Sachyan GA, Nalbandyan AB. Kinetics and mechanism of formaldehyde oxidation. Combust Flame. 1971;17:315-22.
[280] Goldsmith CF, Magoon GR, Green WH. Database of Small Molecule Thermochemistry for Combustion. J Phys Chem A. 2012;116:9033-57.
[281] Burke SM, Simmie JM, Curran HJ. Critical Evaluation of Thermochemical Properties of C1–C4 Species: Updated Group-Contributions to Estimate Thermochemical Properties. J Phys Chem Ref Data. 2015;44:013101.
[282] Zhang K, Banyon C, Togbé C, Dagaut P, Bugler J, Curran HJ. An experimental and kinetic modeling study of n-hexane oxidation. Combust Flame. 2015;162:4194-207.
[283] Pelucchi M, Bissoli M, Cavallotti C, Cuoci A, Faravelli T, Frassoldati A, et al. Improved Kinetic Model of the Low-Temperature Oxidation of n-Heptane. Energy Fuels. 2014;28:7178-93.
[284] Niki H, Maker PD, Savage CM, Breitenbach LP. A Fourier transform infrared study of the kinetics and mechanism for the reaction hydroxyl + methyl hydroperoxide. J Phys Chem. 1983;87:2190-3.

[285] Wang C, Chen Z. Effect of CH3OOH on the atmospheric concentration of OH radicals. Prog Natur Sci. 2006;16:1141-9.
[286] Luo J, Jia X, Gao Y, Song G, Yu Y, Wang R, et al. Theoretical study on the kinetics of OH radical reactions with CH3OOH and CH3CH2OOH. J Comput Chem. 2011;32:987-97.
[287] Wang C, Chen Z. An experimental study for rate constants of the gas phase reactions of CH3CH2OOH with OH radicals, O3, NO2 and NO. Atmos Environ. 2008;42:6614-9.
[288] Baasandorj M, Papanastasiou DK, Talukdar RK, Hasson AS, Burkholder JB. (CH3)3COOH (tert-butyl hydroperoxide): OH reaction rate coefficients between 206 and 375 K and the OH photolysis quantum yield at 248 nm. Phys Chem Chem Phys. 2010;12:12101-11.
[289] Allen HM, Crounse JD, Bates KH, Teng AP, Krawiec-Thayer MP, Rivera-Rios JC, et al. Kinetics and Product Yields of the OH Initiated Oxidation of Hydroxymethyl Hydroperoxide. J Phys Chem A. 2018;122:6292-302.
[290] St. Clair JM, Rivera-Rios JC, Crounse JD, Knap HC, Bates KH, Teng AP, et al. Kinetics and Products of the Reaction of the First-Generation Isoprene Hydroxy Hydroperoxide (ISOPOOH) with OH. J Phys Chem A. 2016;120:1441-51.
[291] Goldsmith CF, Green WH, Klippenstein SJ. Role of O2 + QOOH in Low-Temperature Ignition of Propane. 1. Temperature and Pressure Dependent Rate Coefficients. J Phys Chem A. 2012;116:3325-46.
[292] Goldsmith CF, Burke MP, Georgievskii Y, Klippenstein SJ. Effect of non-thermal product energy distributions on ketohydroperoxide decomposition kinetics. Proc Combust Inst. 2015;35:283-90.
[293] Rauk A, Boyd RJ, Boyd SL, Henry DJ, Radom L. Alkoxy radicals in the gaseous phase: βscission reactions and formation by radical addition to carbonyl compounds. Can J Chem. 2003;81:431-42.
[294] Liu I, Cant NW, Bromly JH, Barnes FJ, Nelson PF, Haynes BS. Formate species in the lowtemperature oxidation of dimethyl ether. Chemosphere. 2001;42:583-9.
[295] Herrmann F, Oßwald P, Kohse-Höinghaus K. Mass spectrometric investigation of the lowtemperature dimethyl ether oxidation in an atmospheric pressure laminar flow reactor. Proc Combust Inst. 2013;34:771-8.
[296] Gao J, Nakamura Y. Low-temperature ignition of dimethyl ether: transition from cool flame to hot flame promoted by decomposition of HPMF (HO2CH2OCHO). Combust Flame. 2016;165:68-82.
[297] Andersen A, Carter EA. First-principles-derived kinetics of the reactions involved in lowtemperature dimethyl ether oxidation. Mol Phys. 2008;106:367-96.
[298] Serinyel Z, Lailliau M, Thion S, Dayma G, Dagaut P. An experimental chemical kinetic study of the oxidation of diethyl ether in a jet-stirred reactor and comprehensive modeling. Combust Flame. 2018;193:453-62.
[299] Tran L-S, Herbinet O, Li Y, Wullenkord J, Zeng M, Bräuer E, et al. Low-temperature gasphase oxidation of diethyl ether: Fuel reactivity and fuel-specific products. Proc Combust Inst. 2018;in press, doi: https://doi.org/10.1016/j.proci.2018.05.135.
[300] Sakai Y, Herzler J, Werler M, Schulz C, Fikri M. A quantum chemical and kinetics modeling study on the autoignition mechanism of diethyl ether. Proc Combust Inst. 2017;36:195-202.
[301] Thion S, Togbé C, Serinyel Z, Dayma G, Dagaut P. A chemical kinetic study of the oxidation of dibutyl-ether in a jet-stirred reactor. Combust Flame. 2017;185:4-15.
[302] Chebbi A, Carlier P. Carboxylic acids in the troposphere, occurrence, sources, and sinks: A review. Atmos Environ. 1996;30:4233-49.

[303] Battin-Leclerc F, Konnov AA, Jaffrezo JL, Legrand M. To Better Understand the Formation of Short-Chain Acids in Combustion Systems. Combust Sci Technol. 2007;180:343-70.
[304] Zervas E, Montagne X, Lahaye J. Collection and analysis of organic acids in exhaust gas. Comparison of different methods. Atmos Environ. 1999;33:4953-62.
[305] Jensen RK, Korcek S, Mahoney LR, Zinbo M. Liquid-phase autoxidation of organic compounds at elevated temperatures. 2. Kinetics and mechanisms of the formation of cleavage products in n-hexadecane autoxidation. J Am Chem Soc. 1981;103:1742-9.
[306] Wang S, Miller DL, Cernansky NP, Curran HJ, Pitz WJ, Westbrook CK. A flow reactor study of neopentane oxidation at 8 atmospheres: experiments and modeling. Combust Flame. 1999;118:415-30.
[307] Ranzi E, Cavallotti C, Cuoci A, Frassoldati A, Pelucchi M, Faravelli T. New reaction classes in the kinetic modeling of low temperature oxidation of n-alkanes. Combust Flame. 2015;162:1679-91.
[308] Jalan A, Alecu IM, Meana-Pañeda R, Aguilera-Iparraguirre J, Yang KR, Merchant SS, et al. New Pathways for Formation of Acids and Carbonyl Products in Low-Temperature Oxidation: The Korcek Decomposition of γ-Ketohydroperoxides. J Am Chem Soc. 2013;135:11100-14.
[309] Le Crâne J-P, Rayez M-T, Rayez J-C, Villenave E. A reinvestigation of the kinetics and the mechanism of the CH3C(O)O2 + HO2 reaction using both experimental and theoretical approaches. Phys Chem Chem Phys. 2006;8:2163-71.
[310] Zaras AM, Szőri M, Thion S, Van Cauwenberghe P, Deguillaume F, Serinyel Z, et al. A Chemical Kinetic Investigation on Butyl Formate Oxidation: Ab Initio Calculations and Experiments in a Jet-Stirred Reactor. Energy Fuels. 2017;31:6194-205.
[311] Dayma G, Thion S, Lailliau M, Serinyel Z, Dagaut P, Sirjean B, et al. Kinetics of propyl acetate oxidation: Experiments in a jet-stirred reactor, ab initio calculations, and rate constant determination. Proc Combust Inst. 2018;in press, doi: https://doi.org/10.1016/j.proci.2018.05.178.
[312] Metcalfe WK, Togbé C, Dagaut P, Curran HJ, Simmie JM. A jet-stirred reactor and kinetic modeling study of ethyl propanoate oxidation. Combust Flame. 2009;156:250-60.
[313] Dayma G, Halter F, Foucher F, Togbé C, Mounaim-Rousselle C, Dagaut P. Experimental and Detailed Kinetic Modeling Study of Ethyl Pentanoate (Ethyl Valerate) Oxidation in a Jet Stirred Reactor and Laminar Burning Velocities in a Spherical Combustion Chamber. Energy Fuels. 2012;26:4735-48.
[314] Grambow CA, Jamal A, Li Y-P, Green WH, Zádor J, Suleimanov YV. Unimolecular Reaction Pathways of a γ-Ketohydroperoxide from Combined Application of Automated Reaction Discovery Methods. J Am Chem Soc. 2018;140:1035-48.
[315] Metcalfe WK, Dooley S, Curran HJ, Simmie JM, El-Nahas AM, Navarro MV. Experimental and Modeling Study of C5H10O2 Ethyl and Methyl Esters. J Phys Chem A. 2007;111:4001-14.
[316] Barusch MR, Crandall HW, Payne JQ, Thomas JR. Identification of β-Dicarbonyl Compounds. Ind Eng Chem. 1951;43:2764-6.
[317] Vanhove G, Yu Y, Boumehdi MA, Frottier O, Herbinet O, Glaude P-A, et al. Experimental Study of Tetrahydrofuran Oxidation and Ignition in Low-Temperature Conditions. Energy Fuels. 2015;29:6118-25.
[318] West RH, Goldsmith CF. The impact of roaming radicals on the combustion properties of transportation fuels. Combust Flame. 2018;194:387-95.

[319] Sun H, Bozzelli JW. Thermochemical and Kinetic Analysis on the Reactions of Neopentyl and Hydroperoxy-Neopentyl Radicals with Oxygen: Part I. OH and Initial Stable HC Product Formation. J Phys Chem A. 2004;108:1694-711.
[320] Yao Q, Sun X-H, Li Z-R, Chen F-F, Li X-Y. Pressure-Dependent Rate Rules for Intramolecular H-Migration Reactions of Hydroperoxyalkylperoxy Radicals in Low Temperature. J Phys Chem A. 2017;121:3001-18.
[321] Mohamed SY, Davis AC, Al Rashidi MJ, Sarathy SM. High-Pressure Limit Rate Rules for α-H Isomerization of Hydroperoxyalkylperoxy Radicals. J Phys Chem A. 2018;122:3626-39.
[322] Mohamed SY, Davis AC, Al Rashidi MJ, Sarathy SM. Computational Kinetics of Hydroperoxybutylperoxy Isomerizations and Decompositions: A Study of the Effect of Hydrogen Bonding. J Phys Chem A. 2018;122:6277-91.
[323] Xing L, Bao JL, Wang Z, Wang X, Truhlar DG. Hydrogen shift isomerizations in the kinetics of the second oxidation mechanism of alkane combustion. Reactions of the hydroperoxypentylperoxy OOQOOH radical. Combust Flame. 2018;197:88-101.
[324] Xing L, Bao JL, Wang Z, Wang X, Truhlar DG. Relative rates of hydrogen shift isomerizations depend strongly on multiple-structure anharmonicity. J Am Chem Soc. 2018;In press, doi: 10.1021/jacs.8b09381.
[325] Silke EJ, Pitz WJ, Westbrook CK, Ribaucour M. Detailed Chemical Kinetic Modeling of Cyclohexane Oxidation. J Phys Chem A. 2007;111:3761-75.
[326] Wang Z, Sarathy SM. Third O2 addition reactions promote the low-temperature auto-ignition of n-alkanes. Combust Flame. 2016;165:364-72.
[327] Tingas E-A, Wang Z, Mani Sarathy S, Im HG, Goussis DA. Chemical kinetic insights into the ignition dynamics of n-hexane. Combust Flame. 2018;188:28-40.
[328] Tingas EA, Kyritsis DC, Goussis DA. Ignition delay control of DME/air and EtOH/air homogeneous autoignition with the use of various additives. Fuel. 2016;169:15-24.
[329] Pei Y, Hawkes ER, Kook S, Goldin GM, Lu T. Modelling n-dodecane spray and combustion with the transported probability density function method. Combust Flame. 2015;162:2006-19.
[330] Yuan W, Li Y, Qi F. Challenges and perspectives of combustion chemistry research. Sci China Chem. 2017;60:1391-401.
[331] Chai J, Goldsmith CF. Rate coefficients for fuel+NO2: Predictive kinetics for HONO and HNO2 formation. Proc Combust Inst. 2017;36:617-26.
[332] Dufour A, Weng J, Jia L, Tang X, Sirjean B, Fournet R, et al. Revealing the chemistry of biomass pyrolysis by means of tunable synchrotron photoionisation-mass spectrometry. RSC Adv. 2013;3:4786-92.
[333] Jia L, Le Brech Y, Mauviel G, Qi F, Bente-von Frowein M, Ehlert S, et al. Online Analysis of Biomass Pyrolysis Tar by Photoionization Mass Spectrometry. Energy Fuels. 2016;30:1555-63.
[334] Jia L, Zhou Z, Li Y, Yang J, Qi F. Novel applications of synchrotron VUV photoionization mass spectrometry in combustion and energy research. Sci China Chem. 2013;43:1686-99.
[335] Baer T, Tuckett RP. Advances in threshold photoelectron spectroscopy (TPES) and threshold photoelectron photoion coincidence (TPEPICO). Phys Chem Chem Phys. 2017;19:9698-723.
[336] Garcia GA, Soldi-Lose H, Nahon L. A versatile electron-ion coincidence spectrometer for photoelectron momentum imaging and threshold spectroscopy on mass selected ions using synchrotron radiation. Rev Sci Instrum. 2009;80:023102.

[337] Tang X, Garcia GA, Gil J-F, Nahon L. Vacuum upgrade and enhanced performances of the double imaging electron/ion coincidence end-station at the vacuum ultraviolet beamline DESIRS. Rev Sci Instrum. 2015;86:123108.
[338] Sztáray B, Voronova K, Torma KG, Covert KJ, Bodi A, Hemberger P, et al. CRF-PEPICO: Double velocity map imaging photoelectron photoion coincidence spectroscopy for reaction kinetics studies. J Chem Phys. 2017;147:013944.
[339] Hemberger P, Custodis VBF, Bodi A, Gerber T, van Bokhoven JA. Understanding the mechanism of catalytic fast pyrolysis by unveiling reactive intermediates in heterogeneous catalysis. Nat commun. 2017;8:15946.
[340] Berndt T, Richters S, Jokinen T, Hyttinen N, Kurtén T, Otkjær RV, et al. Hydroxyl radicalinduced formation of highly oxidized organic compounds. Nat commun. 2016;7:13677.
[341] McLafferty F. Tandem mass spectrometry. Science. 1981;214:280-7.
[342] McLafferty FW. Tandem mass spectrometry (MS/MS): a promising new analytical technique for specific component determination in complex mixtures. Acc Chem Res. 1980;13:339.
[343] Levsen K, Schwarz H. Collisional Activation Mass Spectrometry—A New Probe for Determining the Structure of Ions in the Gas Phase. Angew Chem Int Edit. 1976;15:509-19.
[344] Levsen K, Schwarz H. Gas-phase chemistry of collisionally activated ions. Mass spectrom Rev. 1983;2:77-148.
[345] Puzzarini C. Rotational spectroscopy meets theory. Phys Chem Chem Phys. 2013;15:6595607.
[346] Park GB, Field RW. Perspective: The first ten years of broadband chirped pulse Fourier transform microwave spectroscopy. J Chem Phys. 2016;144:200901.
[347] Brown GG, Dian BC, Douglass KO, Geyer SM, Pate BH. The rotational spectrum of epifluorohydrin measured by chirped-pulse Fourier transform microwave spectroscopy. J Mol Spectrosc. 2006;238:200-12.
[348] Brown GG, Dian BC, Douglass KO, Geyer SM, Shipman ST, Pate BH. A broadband Fourier transform microwave spectrometer based on chirped pulse excitation. Rev Sci Instrum. 2008;79:053103.
[349] Xu Y, Wijngaarden JV, Jäger W. Microwave spectroscopy of ternary and quaternary van der Waals clusters. Int Rev Phys Chem. 2005;24:301-38.
[350] Hansen N, Wullenkord J, Obenchain DA, Graf I, Kohse-Höinghaus K, Grabow JU. Microwave spectroscopic detection of flame-sampled combustion intermediates. RSC Adv. 2017;7:37867-72.
[351] Cuoci A, Saufi AE, Frassoldati A, Dietrich DL, Williams FA, Faravelli T. Flame extinction and low-temperature combustion of isolated fuel droplets of n-alkanes. Proc Combust Inst. 2017;36:2531-9.
[352] Molteni U, Bianchi F, Klein F, El Haddad I, Frege C, Rossi MJ, et al. Formation of highly oxygenated organic molecules from aromatic compounds. Atmos Chem Phys. 2018;18:1909-21.
[353] Gentner DR, Jathar SH, Gordon TD, Bahreini R, Day DA, El Haddad I, et al. Review of Urban Secondary Organic Aerosol Formation from Gasoline and Diesel Motor Vehicle Emissions. Environ Sci Technol. 2017;51:1074-93.
[354] Davis AC, Francisco JS. Reactivity Trends within Alkoxy Radical Reactions Responsible for Chain Branching. J Am Chem Soc. 2011;133:18208-19.
[355] Jokinen T, Sipilä M, Richters S, Kerminen V-M, Paasonen P, Stratmann F, et al. Rapid Autoxidation Forms Highly Oxidized RO2 Radicals in the Atmosphere. Angew Chem Int Ed. 2014;53:14596-600.

[356] Praske E, Otkjær RV, Crounse JD, Hethcox JC, Stoltz BM, Kjaergaard HG, et al. Atmospheric autoxidation is increasingly important in urban and suburban North America. Proc Nat Acad Sci. 2018;115:64-9.
[357] Shrivastava M, Cappa CD, Fan J, Goldstein AH, Guenther AB, Jimenez JL, et al. Recent advances in understanding secondary organic aerosol: Implications for global climate forcing. Rev Geophys. 2017;55:509-59.
[358] Stockwell CE, Veres PR, Williams J, Yokelson RJ. Characterization of biomass burning emissions from cooking fires, peat, crop residue, and other fuels with high-resolution protontransfer-reaction time-of-flight mass spectrometry. Atmos Chem Phys. 2015;15:845-65.
[359] Yokelson RJ, Burling IR, Gilman JB, Warneke C, Stockwell CE, de Gouw J, et al. Coupling field and laboratory measurements to estimate the emission factors of identified and unidentified trace gases for prescribed fires. Atmos Chem Phys. 2013;13:89-116.
[360] Spracklen DV, Jimenez JL, Carslaw KS, Worsnop DR, Evans MJ, Mann GW, et al. Aerosol mass spectrometer constraint on the global secondary organic aerosol budget. Atmos Chem Phys. 2011;11:12109-36.
[361] Tsigaridis K, Daskalakis N, Kanakidou M, Adams PJ, Artaxo P, Bahadur R, et al. The AeroCom evaluation and intercomparison of organic aerosol in global models. Atmos Chem Phys. 2014;14:10845-95.
[362] Shrivastava M, Easter RC, Liu X, Zelenyuk A, Singh B, Zhang K, et al. Global transformation and fate of SOA: Implications of low-volatility SOA and gas-phase fragmentation reactions. J Geophys Res. 2015;120:4169-95.
[363] Master Chemical Mechanism, MCM v3.3.1, http://mcm.leeds.ac.uk/MCM.
[364] Saunders SM, Jenkin ME, Derwent RG, Pilling MJ. Protocol for the development of the Master Chemical Mechanism, MCM v3 (Part A): tropospheric degradation of non-aromatic volatile organic compounds. Atmos Chem Phys. 2003;3:161-80.
[365] Vereecken L, Aumont B, Barnes I, Bozzelli JW, Goldman MJ, Green WH, et al. Perspective on Mechanism Development and Structure-Activity Relationships for Gas-Phase Atmospheric Chemistry. Int J Chem Kinet. 2018;50:435-69.